# Interfacial electrokinetic transport phenomena and their impact on DNA electrophoresis in microfluidics

Vom Fachbereich Maschinenbau
an der Technischen Universität Darmstadt
zur
Erlangung des akademischen Grades eines Doktors der
Naturwissenschaften (Dr. rer. nat.)
genehmigte

**Dissertation**

vorgelegt von

**Dipl. Biol. Thomas Hahn**
geboren in Spremberg

Berichterstatter: Prof. Dr. Steffen Hardt (Technische Universität Darmstadt)
Mitberichterstatter: Prof. Dr. Nico van der Vegt (Technische Universität Darmstadt)
Tag der Einreichung: 23.11.2010
Tag der mündlichen Prüfung: 25.01.2011

Darmstadt 2011
D17

Ich, Thomas Hahn, erkläre, daß ich die vorliegende Arbeit selbständig angerfertigt habe.

Darmstadt, 15.02.2011 .....

Ort, Datum Unterschrift

## Summary

The dissertation examines two different options to separate DNA based on differences in size by utilising electric fields. Each of the techniques is based on a new approach and faces several fundamental problems concerning electrokinetics. A microfluidic environment is chosen to experimentally investigate DNA electrophoresis at a small scale.

A sophisticated setup is employed that on the one hand enables a multiphase flow, while at the same time it stabilises two immiscible polymer phases in a microfluidic compartment. An aqueous two-phase system consisting of poly(ethylene glycol) and dextran provides a stable liquid-liquid interface under quiescent conditions. Such a setup allows the application of an electric field perpendicular to the liquid-liquid interface. In doing so, DNA accumulates at the interface. The parameters influencing the electrophoretic adsorption process are examined in detail. A highlight of the experimental investigations is desorption of DNA from the interface that is triggered by increasing the electric field strength. The latter phenomenon affords a separation of different sized DNA fragments across the liquid-liquid interface. Smaller DNA fragments desorb at lower field amplitudes while larger ones desorb at larger field strengths. Although liquid-liquid interfacial phenomena in aqueous two-phase systems are complex, a preliminary understanding is achieved addressing basic theoretical issues.

In the following the reader is introduced into a second and alternative setup to yield a size separation of DNA. The approach is based on traditional capillary electrophoresis. The novelty is examined by combining several preconcentration techniques with a gel-based size separation of DNA in a preparative manner. The DNA migrates due to the application of an electric field. The preconcentration is accomplished by electrokinetic trapping at a charged membrane embedded into a poly(methyl methacrylate) microchip. It has been found that a fluidic counter flow supports DNA trapping at a membrane. A subsequent DNA size separation is exploited to separate free fetal DNA from maternal DNA in blood of pregnant women providing preliminary results to afford a basis for non-invasive prenatal diagnosis.

## Zusammenfassung

Die Dissertation untersucht zwei verschiedene Optionen, um DNS nach der Größe unter Verwendung elektrischer Felder zu trennen. Die entwickelten Verfahren basieren jeweils auf einen völlig neuen Ansatz während sie den Leser mit einigen grundlegenden Problemen der Elektrokinetik konfrontieren. Eine mikrofluidische Umgebung ist gewählt, um experimentell DNS-Elektrophorese in einem kleinen Maßstab zu betreiben. Eine anspruchsvolle Einrichtung wurde entwickelt, die auf der einen Seite ermöglicht auch unter ruhenden Bedingungen ein Mehrphasensystem zu stabilisieren. Das wässrige Zweiphasensystem, bestehend aus Polyethylenglykol und Dextran, bietet eine stabile flüssig-flüssig Phasengrenze. Die entwickelte Einrichtung ermöglicht es, ein elektrisches Feld senkrecht zur flüssig-flüssig Phasengrenze anzulegen. Dabei akkumuliert DNS an der Phasengrenze. Die Parameter, die die elektrophoretische Adsorption beeinflussen werden im Detail dargestellt. Ein Höhepunkt dieser experimentellen Untersuchungen ist die Desorption der DNS von der Phasengrenze ausgelöst durch die Erhöhung der elektrischen Feldstärke. Letzteres Phänomen ermöglicht eine Trennung von unterschiedlich großen DNS Fragmenten. Kleinere DNS Fragmente desorbieren bei niedrigeren Feldstärken während große DNS Fragmente bei größeren Feldstärken desorbieren. Obwohl die Grenzflächenphänomene in wässrigen Zweiphasensystemen komplex sind und man erst am Beginn des Verstehens ist, gibt eine Diskussion mit Reflektion auf den bisherigen Kenntnisstand einige theoretische Hinweise.

Im Folgenden wird der Leser in eine zweite Einrichtung eingeführt, die eine Größentrennung von DNS erlaubt. Der Ansatz basiert auf traditioneller Kapillarelektrophorese. Die Neuheit besteht in einer präparativen Trennung von DNS während die Anreicherung an einer negativ geladenen Membran eingebettet in einem PMMA Chip erfolgt. Es wurde festgestellt, dass ein fluidischer Gegenstrom die DNS Anreicherung an der Membran begünstigt. Eine nachträgliche DNA Größentrennung wird ausgenutzt, um fötale DNS aus dem mütterlichen Blut zu isolieren. Damit sind vorläufige Ergebnisse für eine nicht-invasive Pränataldiagnostik bereitgestellt.

# Interfacial electrokinetic transport phenomena and their impact on DNA electrophoresis in microfluidics

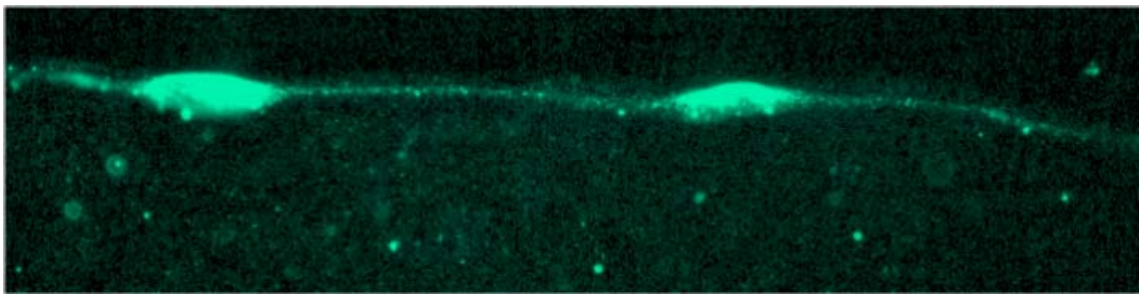

λ-DNA at a liquid-liquid interface forms islands

Thomas Hahn

# Content

# Chapter 1: Introduction

## 1.1 Microfluidics

Since the introduction of micro total analysis systems (μTAS) in 1990 [1] confluences from biology, chemistry, physics and engineering have contributed to the development of this emerging area. μTAS has brought together engineers and natural scientists of many fields. Engineers have scaled channels down to micrometres and even nanometres utilising new fabrication techniques [2]. Physicists have investigated forces that are insignificant in the macroworld, but gain considerable importance at small length scales. Such forces have been exploited, e.g. the rise of water in a capillary just by capillary action, to transport liquid that otherwise would be inopportune on a macroscale approach. Chemists have developed pathways to modify channel surfaces and have thereby created novel material properties for polymers. The modifications of material properties again enabled physicists to study and control the characteristics and behaviour of the fluid in the channels such as surface slip on superhydrophobic surfaces [3]. Chemical engineers have made their contribution to micro process technologies that enable safer handling of dangerous products [4, 5]. Scaling up the number of micro channels already results in a higher production output than classical approaches [6].

Alongside biologists found their interests in new applications concerning medical devices. Cells, proteins and deoxyribonucleic acids (DNA) can be manipulated in microchannels; they can be brought together to interact as well as amongst themselves chemicals in micro process technologies. Clinical biologists have used microfluidics to develop lab-on-a-chip devices for point-of-care diagnostics. The underlying objective of these developments has been to bring low cost disposable applications directly to the patient. New insulin pumps based on microfluidics have automated already the daily administration [7] and microchips have been exploited to control the drug release [8, 9]. The list of examples is endless, if one considers all applications that appeared from the μTAS concept. In general the area is still emerging and will bring new applications in our daily life.

Nevertheless fundamental research to understand the processes at a small scale is essential. Reliability and reproducibility of the aforementioned applications are key issues, if the μTAS concept is to address a wider public for point-of-care diagnostics and fulfils the IVD (in-vitro diagnostic device) regulations in a medical environment. Thus, a detailed understanding of the physical phenomena is essential.

## 1.2 Biological demand for DNA size separation on chip

It has been mentioned that there is a large interest to transfer the fundamental knowledge of microfluidics to the lab-on-a-chip concept, which will evolve into point-of-care diagnostic applications. For clinical investigations concerning the genetic background, e.g. for cancer diagnosis or any other, DNA size separation has been a tool for analytical purposes [10]. In gel electrophoresis an electric field transports the negatively charged DNA through a matrix. Smaller DNA fragments move faster through the matrix than larger ones. The sieving ability of the matrix separates DNA fragments according to their size and enables to distinguish alleles by polymerase chain amplification techniques such as multiplex ligation-dependent probe amplification [11]. The development of capillary electrophoresis systems have improved the speed of conventional electrophoresis systems [12-16]. Nevertheless, capillary electrophoresis has been limited to analytical solutions. So far no concept had been available to separate DNA fragments according to their size for preparative purposes in a microchannel from complex samples.

Eventually, the large number of available systems for DNA size separation does not decrease the demand for further investigations concerning new approaches tackling this issue. The reader will understand the need for automated preparative DNA separations looking at the research investigating non-invasive methods for prenatal diagnosis. It has been found that cell-free fetal DNA circulates in maternal blood of pregnant women [17]. This fetal DNA is biochemically indistinguishable from maternal DNA, however fetal DNA is smaller in size, mainly smaller than 300 bp and therefore, smaller than maternal DNA (> 500 bp) circulating cell-free in the blood of pregnant women [18, 19].

The possibility of accessing fetal DNA from a blood sample of pregnant women provides a risk-free analysis of the fetus' heredity background. In case of genetic disorders appropriate medication and treatment would prevent unfavourable developments.

## 1.3 Objective and organisation of this thesis

**Objective**

The purpose of this documentation is mainly devoted to the physical understanding of the electrophoretic DNA adsorption at interfaces. The investigations report about liquid-liquid interfaces - a field of emerging interest. Such interfaces between two liquid phases are usually expected to be a region of some nano metres wide. Herein experiments are described concerning DNA adsorption to a liquid-liquid interface of an aqueous two-phase system (ATPS) with an electric field acting perpendicular to the interface. Eventually the process of DNA desorption into the non-preferred polymer phase of the ATPS is experimentally investigated in greater detail to find the parameters for the accumulation of DNA at such an interface. It has been found that desorption of DNA is chain length dependent and carries the signature of a thermally activated process, while the molecules escape from a metastable state. The liquid-liquid interface has been exploited to achieve separation of several DNA fragments. The results indicate a great promise for this technique to be utilised for size separation of DNA in preference to conventional methods. For DNA separation concerning preparative isolations this new technique is certainly promising in speed and efficiency.

The investigations about liquid-liquid interfaces highlight some other interesting phenomena regarding the electrophoretic stretching of DNA adsorbed at the interface. Chromosomal DNA has been stretched at a liquid-liquid interface and visualised using the epifluorescence microscope to demonstrate this.

In subsequent chapters the electrophoretic transport of DNA towards a charged membrane interface and its accumulation is investigated. Negatively charged

membranes such as poly(ethylene terephtalate) (PET) are used to trap DNA based on charge exclusion. The phenomenon is known under electrokinetic trapping at nanopores. In this report a fluidic counterflow contributes to the trapping process at the charged membrane. It is theoretically shown how the fluidic counterflow can be incorporated into the general Nernst-Planck equations to describe the ion flux at the membrane pores.

The electrokinetic trapping process is intended to be integrated into a complex lab-on-a-chip system to preconcentrate and separate DNA fragments according to their size. In the presented system a general capillary electrophoresis approach has been chosen to achieve a preparative DNA separation. The novelty is achieved by the combination of the electrokinetic trapping approach with a transient isotachophoresis for further stacking and subsequent size separation exploiting the sieving ability of a matrix. Experiments with real samples from blood of pregnant women illustrate the applicability of the microchip to isolate cell-free fetal DNA. The presented microchip is the first device that enables a preparative sample preparation from a complex sample with an option to automate the entire process [20].

**Organisation**

An extensive literature review of the electrokinetic phenomena at interfaces introduces the theoretical background required for this thesis. The understanding of electrokinetics requires a comprehension of the electric double layer, the evolution of the Poisson-Boltzmann equation and the understanding of liquid-liquid interfaces. Subsequently the fundamental background concerning nucleic acids is summarised with emphasis on the behaviour of DNA in electric fields. All important methods to separate DNA in microfluidics are presented. The following chapter introduces ATPSs and prepares the reader for the investigations concerning liquid-liquid interfaces.

Chapter 5 describes the setup required to investigate a liquid-liquid interface followed by the characterisation of some properties of the polymer phases and electrophoretic migration of ions and biomolecules. Chapter 7 to 10 discuss results regarding the

adsorption and desorption of DNA from the liquid-liquid interface including the developed size separation of DNA as a novel technique.

Finally, Chapter 11 introduces into a disposable preconcentration and separation device for DNA. This PMMA microchip utilises a combination of preconcentration techniques such as electrokinetic trapping and isotachophoresis to stack DNA from a large volume sample into a small channel. Following chapters evolve the process and give detailed results showing the applicability of the microchip to isolate cell-free fetal DNA from maternal blood.

# Chapter 2: Interfacial electrokinetic phenomena

## 2.1 Summary

Forces due to an electrostatic or applied potential have a great applicability in microfluidics. This chapter can just give an overview about the basic principles required for the comprehension of the results examined in this book. The chapter focuses on Coulomb interactions and electrokinetic phenomena such as electrophoresis. An overview about the historical concepts of the electrostatics at interfaces accomplishes this examination. For further details the reader is referred to various books [21-23].

## 2.2 Interactions of small matter

**Electrostatic interactions**

Electrostatic interactions of two charged molecules or ions are derived from Coulomb's law. In some cases they are comparable in their strengths to covalent bonds. In microfluidics Coulomb forces have impact on several electrokinetic phenomena, such as providing the condition for the electroosmotic flow due to an adsorption of electrolyte counterions on a charged material and an applied electric field longitudinal to the surface. In nanofluidics their contribution is even more important, e.g. for the repulsion of coions on charged nanopores of a membrane. Such electrostatic contributions in nanochannels lead to an electroviscous effects or electrokinetic trapping phenomena where Coulomb forces retard ions at nanopores of permselective membranes.

The free energy for the Coulomb attraction between two charges ($q_1$ and $q_2$) with distance ($r$) is given by [22]

$$w(r) = \frac{q_1 q_2}{4\pi\varepsilon_0\varepsilon_r r} \qquad 2.2.1$$

where $\varepsilon_r$ is the relative permittivity and $\varepsilon_0$ is the dielectric constant.

Such electrostatic interactions determine the activity coefficient of an ion species – an important parameter in electrokinetics [24, 25]. How these interactions are described by the Debye-Hückel parameter is issued in Chapter 2.3.

**Ion-ion pair interactions**

Ion-ion pair interactions, sometimes denoted as ion associations, appear mainly in solvents of low dielectric constant. Usually in water at room temperature these kinds of interactions are not present. However, in presence of large electric fields the dielectric constant decreases in any solvent and ion-ion interactions cannot be neglected even in water [26]. An example is the interaction of sodium ions with DNA due to a lower dielectric constant in the minor and major groove of the DNA helix [27]. The dielectric decrement is typical for such surfaces with a large zeta potential. The phosphates in the DNA backbone with a high charge density are perfect to form ion-ion pair interactions as the attractive Coulomb force is naturally strong.

Further, ion-ion pair interactions are considered to contribute to the structure of liquid-liquid interfaces [28, 29]. Due to the presence of high electric fields at such interfaces a decreased dielectric constant is suggested to support such interactions.

**Van der Waals interactions**

Van der Waals forces are dipole-dipole interactions, which either result from two dipoles or one dipole inducing another dipole in a non-polarized molecule. Moreover, London-forces, which result from a spontaneous dipole formation due to the interaction of two non-polarized molecules, are understood as Van der Waals forces [23]. The classification of Van der Waals forces is reviewed in Tab. 1.

Commonly, Van der Waals forces are long range interactions up to 10 nm. At short distances the molecules experience a strong repulsion, but are attracted at larger distances. The Van der Waals energy incorporates into the Lennard-Jones potential,

which is consulted to describe the potential energy at a certain distance ($r$). For large distances with $\sigma \leq r$ the Lennard-Jones potential is negative and the dipoles attract each other (Fig. 1)

$$V^{LJ} = 4\varepsilon\left[\left(\frac{\sigma}{r}\right)^{12} - \left(\frac{\sigma}{r}\right)^{6}\right] = \varepsilon\left[\left(\frac{r_m}{r}\right)^{12} - 2\left(\frac{r_m}{r}\right)^{6}\right] \qquad 2.2.2$$

where $\varepsilon$ is the depth of the potential well, $\sigma$ is exclusively here the distance where the Lennard-Jones potential is zero and $r_m$ is the distance from the energy minimum $r_m = 2^{1/6}\sigma$. A table with typical parameters to calculate the Lennard-Jones potential can be found in Ref. [30].

*Tab. 1: Classification of the Van der Waals interactions.*

| Van der Waals type | Synonym | Interaction |
|---|---|---|
| Dispersion | London forces | inducible dipole – inducible dipole |
| Orientation | Keesom | dipole-dipole |
| Induction | Debye | dipole-inducible dipole |

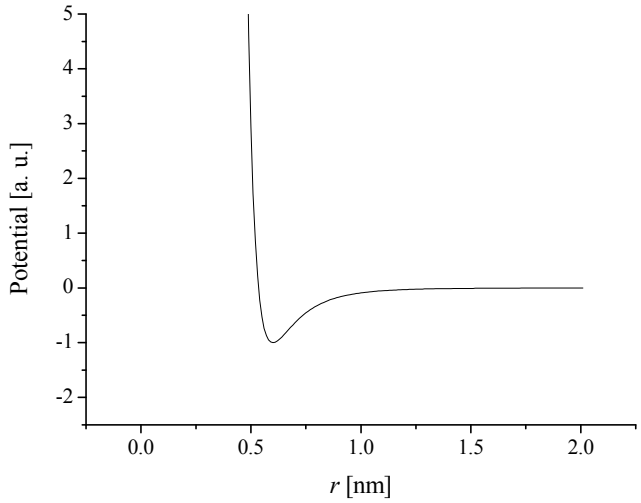


*Fig. 1: Typical plot of a Lennard-Jones potential with a negative potential well indicating attraction.*

**Dipole potential**

Two charges ($q_1$, $q_2$) with opposite sign and with a separation distance $d$ form a dipole potential ($\varphi_P$) that can be experienced by another molecule or ion at location P. This dipole potential at P can be described with the known dipole moment ($p_m = q \times d$) by [31, 32]

$$\varphi_P = \frac{p_m \cos\theta}{4\pi\varepsilon_0 r^2} \qquad 2.2.3$$

where $\theta$ is the angle of P to the dipole axis.

The molecule at P experiences an electric field that consists of a radial ($E_r$) and a vertical ($E_v$) component, while $E_r$ obeys the direction of $r$ and $E_v$ is perpendicular to $r$. Thus,

$$E_r = \frac{p_m \cos\theta}{2\pi\varepsilon_0 r^3} \qquad 2.2.4$$

and

$$E_v = \frac{p_m \sin\theta}{4\pi\varepsilon_0 r^3} \qquad 2.2.5$$

**Hydrogen bonds and the hydrophobic effect**

Typically, electronegative atoms such as oxygen (or N, F, Cl) form hydrogen bonds with neighbouring H atoms. A known example of hydrogen bonds is the DNA molecule. At a favourable distance two atoms share a hydrogen atom. This enables two complementary DNA strands to anneal via the inner bases, depicted for adenine and thymine in Fig. 2. Increased thermal energy breaks up the hydrogen bonds.

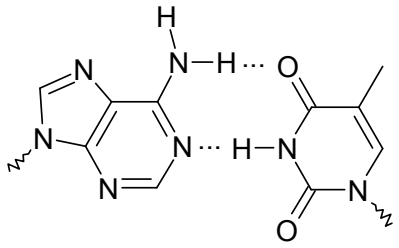


Adenine Thymine

*Fig. 2: Hydrogen bonds of two DNA bases.*

In general, hydrogen bonds are one of the important factors determining the tertiary structure in biomolecules, certainly proteins and DNA. But the most important molecule to describe hydrogen bonds is water, a molecule with unique properties. In the network of water molecules each molecules shares 1-1.5 additional hydrogen atoms [23]. Compounds that interrupt this network of hydrogen bonds are called to be hydrophobic. They exert a repelling effect on water because they do not form hydrogen bonds. This can lead to the situation that an organic solvent exerts a higher surface tension at the water interface compared to the vapour interface. The hydrophobic effect also drives a large attraction of nonpolar molecules brought into water. Typically, these 'hydrophobic attractions' of nonpolar molecules are of long range and decay exponentially between 1-10 nm [33].

## 2.3 Electric Double Layer (EDL)

**Historical development of concepts dealing with an electric double layer**

If one assumes a charged surface of a solid material, counterions of an adjacent electrolyte solution reside at the surface due to electrostatic interactions. These electrostatic interactions generate a depletion of coions and concentration of counterions by repulsive and attractive Coulomb forces. The interactions have been identified as phenomena of the defined electric double layer. In this section details are given comprising a historical review on the development of research on the electric double layer. The emphasis on the details has directly impact on the understanding of the results discussed in the following chapters.

The pioneering work of Hermann von Helmholtz has brought up a first model to elucidate the ion distribution at charged interfaces (Fig. 3A). Herein an approach suggests the adsorption of electrolyte ions at an interface. Similar to a capacitor, a parallel plane forms within the electrolyte solution to compensate charges at the solid substrate [34, 35]. Later, Gouy and Chapman added the thermal energy parameter for the Brownian motion of ions in solutions to the electrostatic interactions and renewed the view onto the EDL by treating it as a diffuse layer (Fig. 3B) [36, 37]. Although the Gouy-Chapman model does not give a final solution, it is appropriate for common problems and simplifies numerical simulations. Afterwards O. Stern combined both models and their basic ideas of a compact layer of adsorbed ions with an adjacent diffuse layer propagating into the bulk [38].

Fig. 3 schematically depicts the ion distribution according to the Helmholtz and Gouy-Chapman models. The later derived Stern model combines a compact layer of fixed counterions with a diffuse layer of uneven charge distribution to reveal an adequate description of the ion distribution at the interface (Fig. 4). The potential accrues from the uneven charge distribution at the interface and decays exponentially with the distance from the interface (Fig. 4). From the Shear plane towards the bulk charges are not fixed to the surface as the Brownian motion exceeds an electrostatic attraction. At the Shear plane the potential can be measured, e.g. using electrophoretic velocity

experiments to reveal the so called zeta potential ($\zeta$) using the Smoluchowski equation [39]. It is herein emphasised that this does not reflect the actual surface potential ($\varphi_s$) (Fig. 4). Moreover, the boundary condition is applied so that there is no slip flow at the shear plane.

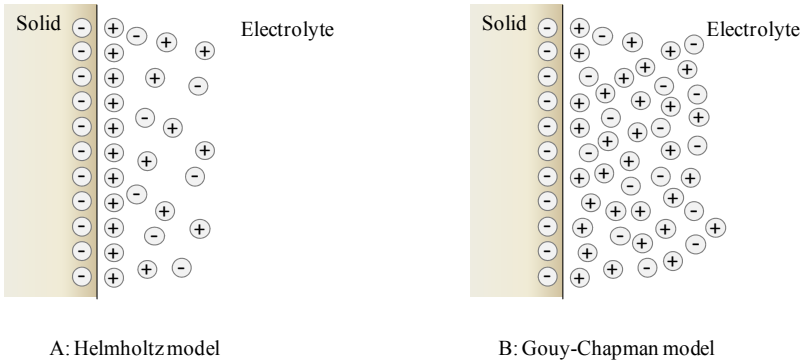


*Fig. 3: The historical concepts of an electric double layer at a negatively charged surface. The Helmholtz model (A) elucidates the EDL concept by two parallel planes. The Gouy-Chapman model (B) adds the Brownian motion into the model leading to a dispersion of charges at the interface.*

Although the figures above denote the model of ion adsorption at a solid-liquid interface, it can also be partly applied for vapour-liquid or liquid-liquid interfaces. This will be issued in Chapter 4.

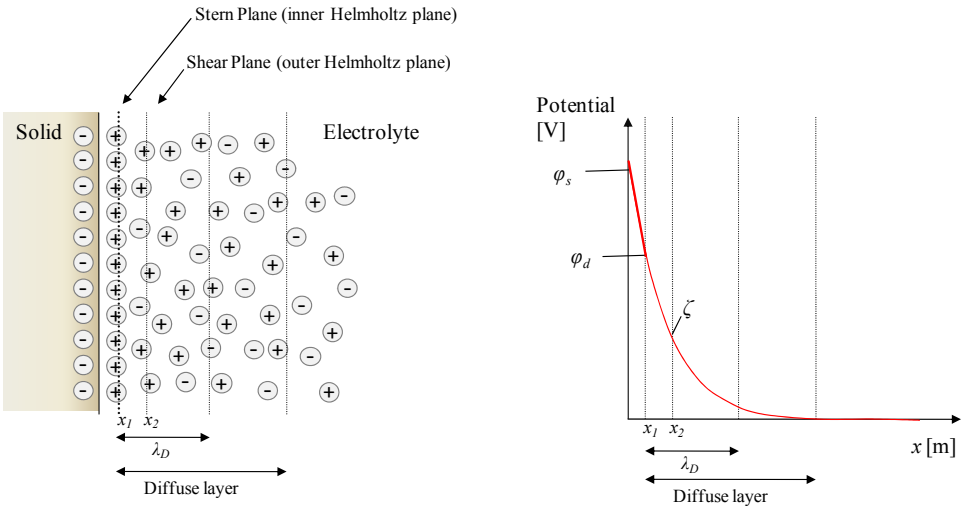


*Fig. 4: Schematic illustration of the ion distribution in the Stern model (Left) and the potential distribution (Right) representing the Debye length and diffuse layer. The Stern potential ($\varphi_d$) is located at the Stern plane ($x_1$) and the zeta potential ($\zeta$) at the shear plane ($x_2$). According to the Stern model the potential decays linearly between surface potential and Stern potential.*

**The Poisson-Boltzmann equation**

As mentioned above, for many analytical problems it is sufficient to use the Gouy-Chapman model. Therefore, in this section it is summarised how it mathematically describes the EDL. It is shown how to derive the differential capacitance of an EDL using the Gouy-Chapman approach. Later it is exemplified where the limitations of the model occur for solid-liquid and liquid-liquid interfaces and a description of the Stern model is given.

In order to relate the spatial distribution of ions normal to a charged surface with the potential, the Boltzmann distribution has to be employed [22].

$$n_i = n_{i\infty} \exp\left(-\frac{z_i e \varphi}{k_B T}\right) \qquad 2.3.1$$

Hereby it is shown that in the bulk electrolyte, where no potential is present ($\varphi = 0$), the ionic number concentration ($n_i$) equals $n_{i\infty}$, the ionic number concentration in the bulk. If the potential gets a value, the ionic number concentration will be larger or smaller than the ion number concentration far away from the solid surface or interface.

Now one can employ the Poisson equation to give an analytical expression for the distribution of the potential due to the presence of a charged surface in a dielectric medium. The Poisson equation is given by

$$\nabla^2 \varphi = -\frac{\sigma_f}{\varepsilon_0 \varepsilon_r}, \qquad 2.3.2$$

and for a one-dimensional problem simplified to

$$\frac{d^2 \varphi}{dx^2} = -\frac{\sigma_f}{\varepsilon_0 \varepsilon_r} \qquad 2.3.3$$

The charge density in the fluid can be written as

$$\sigma_f = \sum_{i=1}^{N} z_i e n_i, \qquad 2.3.4$$

which leads to the one-dimensional Poisson-Boltzmann equation

$$\frac{d^2\varphi}{dx^2} = -\frac{\sum_{i=1}^{N} z_i e n_{i\infty} \exp\left(-\frac{z_i e\varphi}{k_B T}\right)}{\varepsilon_0 \varepsilon_r} \qquad 2.3.5$$

where $N$ is the number of ion species.

The Poisson-Boltzmann equation, as a mean field theory, is appropriate for most of the investigated problems. However, it neglects effects of ion correlation appearing mainly with divalent ions under some conditions [40]. Furthermore, the presence of surfactants can change the actual surface charge and need to be considered in case of being used.

**The Debye length**

The previous section derived the Poisson-Boltzmann equation to relate the ionic number concentration with the potential in an electrolyte normal to an interface. The Debye length $\lambda_D$ can be derived according to Ref. [21] and is dependent on several constants and the concentration ($c_i$) and valence ($z_i$) of $N$ ion species.

$$\lambda_D = \sqrt{\frac{k_B T \varepsilon_0 \varepsilon_r}{N_A e^2 \sum_{i=1}^{N} c_i {z_i}^2}} \qquad 2.3.6$$

**Activity of ions**

Initially it has been mentioned that the electrostatic interactions of ions contribute to the activity coefficient of an ion species. In most of the cases the electrostatic interactions are dominating over all other interactions and the Debye-Hückel limiting law can be applied to derive the activity of an ion [41].

The screening length, a parameter of this coefficient, is related to the ionic strength in the medium (Equation 2.3.6). Further the Debye-Hückel limiting law is applied, which

determines the activity coefficient ($\gamma_i$) of an ion species in a dilute solution (≤ 10 mM) of a certain ionic strength. Therefore one can write according to Ref. [24]

$$\log(\gamma_i) = -\frac{z_i^2 e^2 \kappa}{8\pi\varepsilon_0\varepsilon_r k_B T} = -\frac{z_i^2 e^3}{4\pi(\varepsilon_0\varepsilon_r k_B T)^{3/2}}\sqrt{\frac{I}{2}}, \qquad 2.3.7$$

which relates the ionic strength ($I$) with the activity coefficient. Such an activity coefficient becomes important for calculating the chemical potential as shown in subsequent chapters.

**Capacitance of an EDL**

To derive the capacitance of an EDL according to the Gouy-Chapman model one has to consider the charge density at a surface ($\sigma_s$) in relation to the potential. If the charges in the diffuse layer in the fluid are now projected onto a flat plane, $\sigma_f$ is the phase charge density of the fluid, which equals the quotient of all charges ($q$) in the diffuse layer and area of that plane ($A$). Therefore it is obtained from $q = \varepsilon_0\varepsilon_r A(\mathrm{d}\varphi/\mathrm{d}x)_{x=0}$ and inserted $\mathrm{d}\varphi/\mathrm{d}x$ for symmetrical electrolyte according to Ref. [21]

$$\sigma_s = -\sigma_f = \sqrt{8k_B T\varepsilon_0\varepsilon_r c N_A}\,\sinh\left(\frac{ze\varphi_s}{2k_B T}\right) \qquad 2.3.8$$

Differentiation of the equation above yields the differential capacitance $C_d$

$$C_d = \frac{d\sigma_s}{d\varphi_s} = \sqrt{\frac{2z^2 e^2\varepsilon_0\varepsilon_r c N_A}{k_B T}}\,\cosh\left(\frac{ze\varphi_s}{2k_B T}\right) \qquad 2.3.9$$

Fig. 5 exemplifies the capacitance being dependent on the potential difference for certain ion concentrations.

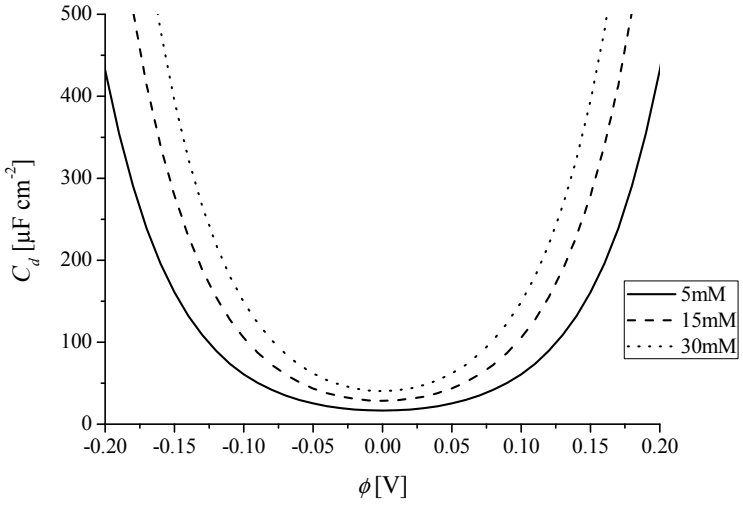


*Fig. 5: The capacitance of an EDL from Eq. 2.3.9 has been plotted for different ion concentrations in water. The absolute temperature has been set to 293 K.*

**Limitations of the Gouy-Chapman theory**

The Gouy-Chapman theory considers ions as point charges where only a diffuse layer is propagating from the interface towards the bulk. This leads to high potentials at the wall not taking into account that the ion size limits the adsorption and therefore the potential in the compact layer (Stern plane). This becomes obvious when the capacitance of the interface is calculated for different potentials (Fig. 6). For larger potentials a maximum capacitance is approached. Considering a potential at the Stern plane $\varphi_d$ at the coordinate $x_1$ as shown in Fig. 4, it applies for the electric field at $x_1$ according to the derivation described in Ref. [21] for symmetrical electrolytes

$$\left(\frac{d\varphi}{dx}\right)_{x=x_1} = -\sqrt{\frac{8k_BTcN_A}{\varepsilon_0\varepsilon_r}}\sinh\left(\frac{ze\varphi_d}{2k_BT}\right) \qquad 2.3.10$$

And the solution charge density at $x_1$ is

$$\sigma_s = -\sigma_f = -\varepsilon_0\varepsilon_r\left(\frac{d\varphi}{dx}\right)_{x=x_1} = \sqrt{8k_BT\varepsilon_0\varepsilon_r cN_A}\sinh\left(\frac{ze\varphi_d}{2k_BT}\right) \qquad 2.3.11$$

According to the approximation of the Stern model the potential decays linearly between the solid surface and the Stern plane (Fig. 4) [38]. Thus,

$$\varphi_s = \varphi_d - \left(\frac{d\varphi}{dx}\right)_{x=x_1} x_1 \qquad 2.3.12$$

while substituting yields the surface charge density to obtain a differential capacitance

$$\sigma_s = -\sigma_f = \sqrt{8k_B T\varepsilon_0\varepsilon_r N_A c}\,\sinh\left[\frac{ze}{2k_B T}\left(\varphi_s - \frac{ze\varphi_d}{\varepsilon_0\varepsilon_r}\right)\right] \qquad 2.3.13$$

The inverse of the differential capacitance ($C_d$) according to the Stern model is the sum of the inverse of the capacitance of the inner Helmholtz plane ($C_H$) and the diffuse layer ($C_D$) [21]

$$\frac{1}{C_d} = \frac{1}{C_H} + \frac{1}{C_D} \qquad 2.3.14$$

and therefore

$$\frac{1}{C_d} = \frac{\lambda_B}{\varepsilon_0\varepsilon_r} + \frac{\lambda_D}{\varepsilon_0\varepsilon_r \cosh(ze\varphi_d / 2k_B T)} \qquad 2.3.15$$

The concept becomes clear in Fig. 6. The maximum capacitance is limited by the Bjerrum length ($\lambda_B$), where the electrostatic interaction equals the thermal energy.

$$\lambda_B = \frac{e^2}{4\pi\varepsilon_0\varepsilon_r k_B T} \qquad 2.3.16$$

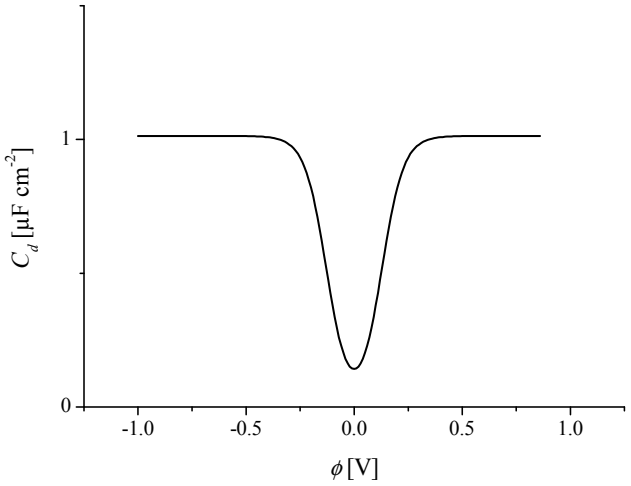


*Fig. 6: The Stern modified Gouy-Chapman theory considers the capacitance of the inner Helmholtz plane to calculate the differential capacitance. Although the parameters have been set as in Fig. 5, the graph is significant different. $\lambda_B$= 0.7 nm and equation 2.3.15 have been used.*

**Limitations of the Poisson-Boltzmann equation**

As documented above, the Boltzmann distribution relates the ionic number concentration with the potential, and recalling the Poisson equation, the potential is related with the permittivity of the medium. This approach assumes uniform permittivity in the solvent, which is often sufficient for general numerical simulations considering moderate charged solid surfaces, particles or molecules. However, in view of highly charged polyions and biomolecules, the complex structure and charged surface raises problems in fitting simulations to experimental data. For instance, the dielectric properties are different for the major or minor groove in the DNA helix due to different polarization of solvent molecules in the proximity [27, 42].

Beside the aforementioned drawbacks, in the Poisson-Boltzmann equation ions are considered as point-charges neglecting their size. In case of highly charged polyions such as DNA, a modification of the Poisson-Boltzmann equation is required that involves a finite ion size and image forces into the theory to evolve the potential distribution at the molecule's surface. In particular, this issue becomes significant for the presence of multivalent electrolyte ions, while for (1:1) electrolytes the Poisson-

Boltzmann equation is sufficient for simulation of the potential distribution for low to moderate salt concentrations at DNA [43].

## 2.4 Diffusion, electrophoresis and electroosmotic flow

**Diffusive transport**

Diffusion is a process that is involved in many problems concerning microfluidics. It is not directly an electrokinetic phenomenon, but overlays the electrokinetic phenomena and is therefore discussed in this section.

If a gradient in concentration of species *i* is present and pressure and temperature are constant, the thermal motion will cause an even distribution of the molecules or ions. This flux of molecules ($J_i$) is described by Fick's first law, where under the given conditions ($p$, $T$ = const) the chemical potential ($\overline{\mu}_i$) is the driving force to distribute the molecules evenly [41]

$$J_i = -\frac{D_i c_i}{RT}\left(\frac{\partial \overline{\mu}_i}{\partial x}\right) \qquad 2.4.1$$

where $D_i$ is the diffusion coefficient, $c_i$ the concentration of the molecule or ion species, $R$ the gas constant and $T$ is the temperature. The chemical potential can be derived from the activity coefficient [21, 24] and the concentration to yield

$$\overline{\mu}_i = \overline{\mu}_i^0 + RT \ln\left(\gamma_i \frac{c_i}{c_i^0}\right) \qquad 2.4.2$$

where $\overline{\mu}_i^0$ denotes for the standard chemical potential.

Although the issue of diffusion is only generally shown here, it must be noted that it becomes more complex, for instance, for semiflexible polymers such as DNA. Polymer chains with lengths larger than the persistence length experience segmental dynamics that add to the general diffusion [44]. This gives a specific size-dependent diffusion coefficient to each polymer length. Further it is necessary to distinguish between a

rotational and translational diffusion coefficient. Simplified, the diffusion coefficient of a small molecule is related to the radius of gyration ($r_g$) as follows

$$D_i = \frac{k_B T}{6\pi\eta r_g} \qquad 2.4.3$$

Moreover the Stokes-Einstein relation gives the relation of the diffusion coefficient to the electrophoretic mobility ($\mu_e$).

$$D_i = \frac{\mu_e k_B T}{q} \qquad 2.4.4$$

where $q$ denotes for the molecule's charge. The Stokes-Einstein relation accounts for many ions quantitatively, but not for polyions such as DNA. For simplicity, a more detailed discussion is here neglected, but revisited in Chapter 3.

**Electrophoresis**

Beforehand it has been evolved how the diffusion is related to the electrophoretic mobility of a charged species. Using the simple relation [39]

$$u = \mu_e E^{ext} \qquad 2.4.5$$

the velocity of a molecule ($u$) can be derived from the applied electric field ($E^{ext}$), if the electrophoretic mobility ($\mu_e$) is known.

This equation is also useful to calculate the electroosmotic flow in a channel due to the adsorption of counterions to a charged surface. In Chapter 2.3 the nature of such an ion adsorption in relation to a surface potential has been extensively described. An applied electric field guides the ions either to the anode or to the cathode. Eventually, the ions push solvent molecules in their direction of migration and cause a net flow of liquid. This effect is called electroosmotic flow.

For charged particles and macromolecules such an electroosmotic flow appears at the molecule surface. The electrophoretic mobility is proportional to the zeta potential ($\zeta$) and Equation 2.4.5 can be rewritten [39]

$$u = \frac{\varepsilon_0 \varepsilon_r \zeta \cdot E^{ext}}{\eta} \qquad 2.4.6$$

To accomplish the discussion it is emphasised that an electroosmotic slip at a particle's surface drives the electrophoretic migration of the particle as long as the Debye length is much smaller than the particle [45-47]. The electrophoresis of ions is described by the polarization of the hydration shell [24, 25]. However, polarization effects can also be present, e.g. for asymmetrical particles that are subjected to a non-uniform slip due to a non-uniform shape [48].

**Diffusive and electrophoretic transport: The Nernst-Planck equation**

Generally, transport of molecules or ions involves more than one process. Diffusion is always present and requires a consideration in electrophoretic transport investigations for some applications. To accomplish the flux involving diffusion and electrophoresis, the Nernst-Planck equations describe the problem accurately. If a volumetric flux is present, a velocity parameter of the fluid $u$ can be also accounted for the net transport. In general, this gives the superposition of all transport phenomena for the species $i$ for a one-dimensional problem being

$$J_i(x) = -D_i \frac{\partial c_i(x)}{\partial x} - \frac{z_i F}{RT} D_i c_i \frac{\partial \varphi}{\partial x} + c_i u \qquad 2.4.7$$

where the ion flux ($J_i$) is given in mol $s^{-1}$ $m^{-2}$, $\varphi$ is the potential, $R$ gas constant, $F$ Faraday constant, $T$ temperature, $z_i$ valence of the ion $i$, $c_i$ concentration and $D_i$ is the diffusion constant. The first term covers the diffusion, the second term the electrophoretic transport, sometimes also called migration, and the latter term denotes the convection [21].

## 2.5 Electroosmotic flow

**General principles**

The accumulation of counterions in an electrolyte adjacent to a charged surface, for instance a solid substrate, is the condition for the presence of an electroosmotic flow if an external electric field is applied longitudinal to the surface. The counterions, which are dominating the electrolyte over the coions adjacent to the surface of the material, start to migrate towards their respective electrode. The migration in the Debye-layer at the solid-liquid interface acts mainly in one direction and solvent molecules are pushed with the counterions resulting in an electroosmotic flow. In microchannels this flow transfers the liquid from one side to another and its velocity is [22]

$$u_{eo} = \frac{\varepsilon_0 \varepsilon_r \zeta \cdot E^{ext}}{\eta} \qquad 2.5.1$$

where $\zeta$ is the zeta potential of the substrate and $\eta$ the dynamic viscosity.

An illustration of the velocity profile at the wall of a negatively charged substrate is depicted in Fig. 7. Practically a back pressure counteracts with a Hagen-Poiseuille profile to an electroosmotic flow (Fig. 7A). In an ideal situation the velocity profile is flat without any contributions of a pressure-driven flow (Fig. 7B). The first case is commonly present at larger time scales, if the liquid in one reservoir at the end of a microchannel increases the filling height causing a back pressure, while the latter case resides only in the beginning of the pumping process.

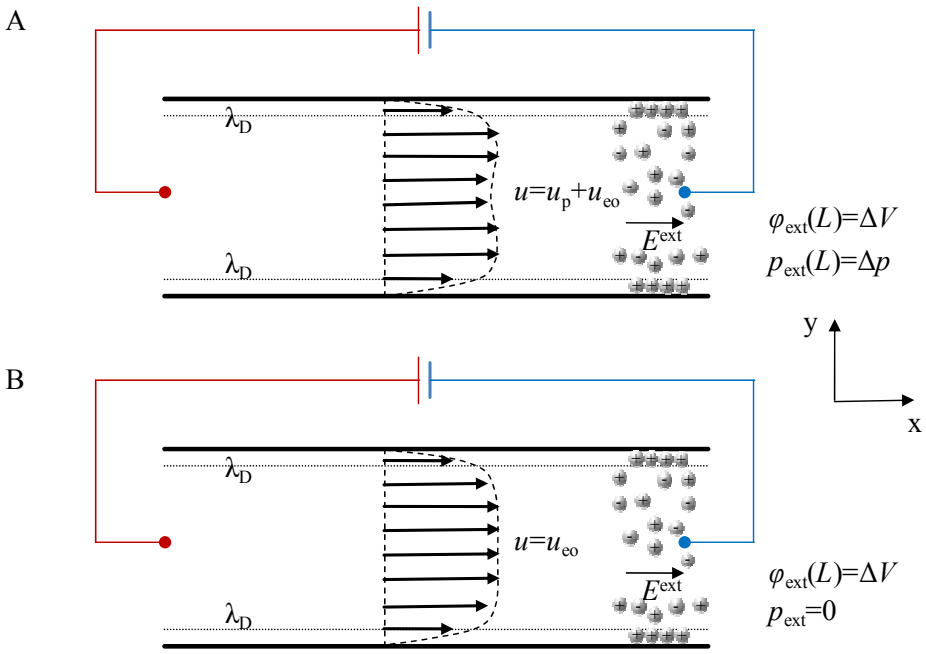


*Fig. 7: Sketch of the electroosmotic flow velocity (u) profile in a microchannel with (A) and without (B) a backpressure (p). The ion distribution in the liquid due to a charged surface is sketched.*

The applied back pressure follows the Hagen-Poiseuille law in absence of slip and causes a back flow with the velocity

$$u_p(r) = \frac{\Delta p}{4\eta l}(a^2 - r^2) \qquad 2.5.2$$

where $a$ is the radius and $r$ the distance from the centre of the circular microchannel. As sketched in Fig. 7, the electroosmotic flow and the flow due to a pressure gradient follow the superposition principle.

The principles of the electroosmotic flow (EOF) have been used for a variety of electrokinetically driven pumps with the advantage of not containing moving parts [49-65]. Certainly for lab-on-a-chip devices, EOF pumps have shown a great applicability [8, 66, 67].

Electroosmosis or electroosmotic flow advanced lab-on-a-chip devices enormously. Thereby, the electroosmosis in natural systems sometimes becomes forgotten. Electroosmosis is found in many biological systems. For instance, sugar transport in the phloem of plants is driven by electroosmosis [68].

**Efficiency of the electroosmotic flow**

Theoretical papers describe the efficiency of EOF pumps being dependent on the zeta potential, the Debye length and Levine number at a condition of maximum pump work. For small zeta potentials the efficiency increases with the square of the zeta potential and reaches the maximum at large zeta potentials. The Levine number describes the nominal ratio of convective and conductive electric currents [69, 70].

Such evaluations help to design a microfluidic setup with incorporated EOF pumps where energy efficiency is important. This is attributed to battery-driven microchips for e.g. invasive drug delivery purposes [8, 9] or other medical implants [71].

In nanochannels the flat plug-flow profile, typical for EOF flows, deviates. The velocity field is rather curved [72].

**The electroviscous effect**

Applying a pressure driven flow in a nanochannel or slit microchannel of a few hundreds nanometres high, an electroviscous effect is observed, if the substrate is charged. The flow establishes a potential gradient between the ends of the channel and an electric field is generated. Due to the electrostatic repulsion from the channel wall co-ions are retarded. The arising potential is also denoted as streaming potential [22] and can be used to derive the zeta potential of channel walls [73].

## 2.6 Capillarity, surface tension and Young's equation

Capillary forces are primary relevant in microfluidics when macroworld forces such as gravity become irrelevant. The Young-Laplace equation sets the pressure difference across, e.g. the fluid-vapour interface into relation with the surface tension and is the nonlinear partial differential

$$\Delta p = \gamma \nabla \cdot \vec{n} \qquad 2.6.1$$

where $\vec{n}$ is the unit vector normal to the interface. Local gradients in the surface tension will cause pressure gradients and Marangoni convection. Marangoni convection is the result of liquid moving from regions of low to regions of high surface tension. Such convections are relevant for any interface and account also for liquid-liquid interfaces [74].

In order to relate the interfacial tension to the surface potential one can consult Lippmann's equation [75], which is important for electrowetting applications and in general

$$\left(\partial\gamma/\partial E_A\right)_{T,p,\bar{\mu}_i \neq \bar{\mu}} = -Q_A \qquad 2.6.2$$

Eq. 6.7.3 relates the excess charge ($Q_A$) to the interfacial tension and electric field ($E_A$) at a certain area ($A$). Further it can be transformed using the surface charge density and the potential ($\varphi$) [76]

$$\left(\partial\gamma/\partial\varphi\right)_{T,p,\bar{\mu}} = -\sigma_s \qquad 2.6.3$$

The surface charge density is

$$\sigma_s = \frac{C}{A}\varphi = \frac{\varepsilon_0 \varepsilon_r \varphi}{d} \qquad 2.6.4$$

where $C$ is the capacitance of the interfacial electric double layer and for a capacitor of two parallel planes it applies

$$C = \frac{\varepsilon_0 \varepsilon_r A}{d} \qquad 2.6.5$$

In electrowetting applications an applied potential between an aqueous droplet placed above an insulator and an electrode induces a change in the contact angle of the aqueous droplet. This relation allows estimating the applied potential from the change in the surface tension [76, 77]

$$\gamma_{0,1} = \gamma_{0,1}^0 - \frac{\varepsilon_0 \varepsilon_r \varphi^2}{2d} \qquad 2.6.6$$

According to Young's equation the contact angle modifies with surface tension and is accordingly [76]

$$\cos\theta^{\varphi\neq 0} = \cos\theta^{0} + \frac{\varepsilon_0 \varepsilon_r \varphi^2}{2\gamma_{0,1} d} \qquad 2.6.7$$

The principle can be used for processing optical lenses made of liquids in microfluidics with low response times [78].

# Chapter 3: Fundamentals of nucleic acids in electric fields

## 3.1 Summary

Nucleic acids are definitely the most important biomolecules in any way. No life is possible without them. They are present in the nucleus of a cell as well as in mitochondria, plastids and viruses. Nucleic acids can also occur cell-free after cell degradation and have enzymatic functions in form of ribozymes [79]. Nucleic acids are the only molecules that allow the conservation of life for all organisms known. The chemical stability of some nucleic acids is outstanding and makes them last for hundreds of years. The latter fact is the condition for the possibility of forensic analysis, a topic that gained interest in microfluidics [67].

Two complementary nucleic acid strands can anneal to form double-stranded desoxyribonucleic acid (dsDNA), a helix that is 2 nm thick for B-DNA. In biological systems (*in vivo*) the strand interaction is co-controlled by proteins and undoubtedly complicated to understand. Theoreticians evolved theories of the annealing process *in vitro* by looking at the structure of the energy well DNA experiences, if two strands slide along each other [80]. The DNA helix carries a sugar-phosphate backbone exposed to the outer space of the molecule. The phosphate with its three oxygen atoms gives the molecule a negative charge at neutral to basic pH. The extension of many segments, each carrying a base pair at the inner side encoding the genetic code, and outside a phosphate, multiplies the charge. In that sense DNA fulfils the properties of being a polyion and makes it interesting to study its electric and dielectric properties. This chapter focuses on these properties of DNA and describes a variety of applications beside its behaviour in electric fields.

## 3.2 Electrophoresis of DNA

### General properties of DNA

The repeating structure of nucleic acids with the bases adenine, thymine, cytosine and guanine being connected via (desoxy)ribose units, enables the utilisation of bead-spring models for molecular dynamics simulation concerning DNA. Such evaluations elucidate e.g. the condensation of DNA supported by counterions and coulomb interactions [81]. Large DNA molecules experience an energy minimum in a coiled state. Small molecules of the order of a few persistence lengths remain in a rigid rod-like conformation. The difference in the DNA structure contributes to alterations in the electrophoretic mobility of DNA molecules. Molecules of less than 500 bp exert a decreasing electrophoretic mobility with decreasing length [82-85]. Tab. 2 summarises several parameters concerning B-DNA apart from the aforementioned data. B-DNA is the common conformation of double stranded DNA (dsDNA) in aqueous solutions. Beside B-DNA the coexistence of A-DNA and Z-DNA is known. The Z-DNA conformation is directed by certain proteins bringing the DNA helix in a higher energy minimum and changes its structural parameters such as from a right-handed to a left-handed direction of rotation [86, 87].

*Tab. 2: Some important parameters for B-DNA*

| dsDNA Characteristics | Data | Ref. |
|---|---|---|
| Polarizability | $10^{-34}$ F m$^2$ bp$^{-1}$ | [88-92] |
| 1 µg λ-DNA 48502 bp | 0.03 pmol; 1.8 $10^{11}$ molecules | [93] |
| Molecular weight of 1 bp | 650 Dalton | |
| Density | 1.7 g cm$^{-3}$ | [94] |
| Electrophoretic mobility λ-DNA (in 45 mM Tris/borate pH 8.3) | $4.5 \times 10^{-8}$ m$^2$ V$^{-1}$ s$^{-1}$ | [85] |
| Segment radius | 1 nm | |
| Persistence length | 50 nm | [95, 96] |

**Diffusion and electrophoretic mobility of DNA**

The Einstein relation gives the dependence of the diffusion coefficient on the electrophoretic mobility using $z$ as the number of charged residues in the ion and $e$ the elementary charge.

$$D = \frac{\mu_e k_B T}{ze} \qquad 3.2.1$$

The diffusion coefficient has been modified for nucleic acids. Further, a macromolecule underlies a rotational ($D_r$) and a translational diffusion coefficient ($D_t$) [97]. The rotational diffusion coefficient for a rod-like macromolecule is [98]

$$D_r = \frac{3k_B T(\ln(p) + \delta)}{\pi\eta L^3} \qquad 3.2.2$$

where $p$ is exclusively here the axial ratio ($p = L/d$) with the end-to-end length ($L$) of the chain, $d$ is the diameter, correction factor ($\delta$), thermal energy ($k_B T$) and $\eta$ is the viscosity. Eventually, the translational diffusion coefficient is given by [98]

$$D_t = \frac{k_B T(\ln(p) + v)}{3\pi\eta L} \qquad 3.2.3$$

where $v$ is a correction for end effects and given as $v = 0.312 + 0.565/p - 0.1/p^2$ [97]. A measure for the end-to-end length of polymers idealized to a chain of beads connected by springs can be practically derived from the Zimm model [99-101], which is sometimes consulted to model DNA polymers [102, 103].

The size dependence of the diffusion coefficients proceeds in the electrophoretic mobility of DNA. The electrophoretic mobility of double stranded DNA increases with chain length until ≈ 500 bp and remains constant above this length [85, 104]. Further the electrophoretic mobility is dependent on the electrolyte composition used. The DNA conformation being dependent on the electrolyte is also partly accounted for a different electrophoretic mobility [83]. Beside the length dependence on the conformation of a DNA molecule the sequence contributes to the conformation. Long adenine tracts cause a significant bending in the molecule that changes the conformation and the electrophoretic mobility [105, 106], which proceeds due to an asymmetric counterion

condensation [98]. However, in general the length dependence contributes at most to the difference in the mobility, certainly for stiffed rods, which is the dominant conformation of DNA of a few hundreds base pairs. Coiled DNA molecules (> 500 bp) enter a constant electrophoretic mobility [83].

**Isotachophoresis**

Isotachophoresis (ITP) is a common technique separating charged molecules or ions according to their electrophoretic mobility [107]. The sample molecules or ions are packed into a discontinuous electrolyte system consisting of anions and cations, whereas two different types of sample co-ions are provided, a leading electrolyte (LE) of co-ions with a higher electrophoretic mobility and a terminating electrolyte with co-ions of lower electrophoretic mobility than the sample ion. For negatively charged DNA, chloride anions can be chosen for the leading electrolyte and HEPES/imidazol, MOPS or glycine for a terminating electrolyte [108, 109]. A potential is applied between the discontinuous buffer system resulting in a stacking of the sample ions in its specific zone of electrophoretic mobility. Hence, isotachophoresis can be used as a stacking technique or for separating different species of charged molecules or ions if the electrophoretic mobilities of the analytes are sufficiently distinct. Several reports used isotachophoresis as a preconcentration technique for nucleic acids [108, 110-117].

A transient isotachophoresis accounts for the change of electrolyte after a certain stacking period to achieve a homogeneous electrolyte system [118-120]. This enables to enter a size separation in gels due to a sieving effect after the preconcentration is accomplished. In general this has been shown to be also applicable for nucleic acids in complex lab-on-a-chip devices [121].

**Field-amplified sample stacking**

Nucleic acids and other charged components can be stacked in a microchannel, if they are placed in a region of lower conductivity that is surrounded by regions of higher conductivity. This is controlled by establishing gradients of ion concentrations in a microchannel. The large electric field in the sample zone accelerates the polyions to stack at the neighbouring zone of higher conductivity with lower field strengths. Usually this is successfully applied in microfluidics where a small diffusion potential limits the mixing of such zones. However, the electric field must be applied immediately after the zones have been brought into contact as the diffusion potential will mix them [122-124].

Field-amplified sample stacking can be easily combined with other stacking methods such as isotachophoresis and electrokinetic trapping to achieve improved preconcentration of analytes [121].

## 3.3 Size separation of DNA

Size separation of DNA in matrix-filled capillaries or microchannels is known for many years and mainly used for analytical purposes [13, 125]. Unfortunately, many procedures performed in microchips have been limited to analytics as the recovery of DNA from microchips remains challenging. The preparative size separation of DNA in microfluidics is interesting for diagnostic purposes such as isolation of free fetal DNA from maternal blood of pregnant women to enable non-invasive prenatal diagnosis as the sample can be transferred to a subsequent analysis of genetic disorders. The DNA fragments of such fetal DNA circulating cell-free in maternal blood is smaller in size than the maternal DNA and can be significantly enriched using a preparative size separation [18, 19, 126]. The need for new DNA separation methods is not limited to the latter example. New DNA sequencing devices require a fast size separation often on chip in multiplexed systems [127, 128]. Traditional gel electrophoresis in capillaries may be the time-limiting factor for these applications.

The last decade increased the interest in gel free DNA separations also with the perspective to achieve a size separation of entire chromosomes that has been previously limited to pulsed field gel electrophoresis [129]. Gel free DNA separation is achieved in microchannels with micro-pillars [130] or periodic arrays of obstacles [131, 132] that alter the electrophoretic velocity in respect to the molecule's size. Such approaches have been combined with pulsed field gel electrophoresis to separate larger DNA molecules [133] or are just driven by a hydrodynamic flow while DNA is interacting with the charged surface of the patterned obstacles [134, 135]. Others report about electrophoresis in combination with a dielectrophoretic trapping where a thermally induced escape from a potential energy minimum drives the size dependent migration of molecules out of one or more trapping regions aligned along a microchannel [91]. The work utilises the size dependent polarizability of DNA in electric fields and achieves a separation. Entropic traps enable the separation of large DNA fragments that are initially coiled and are forced to pass a narrow region of some nanometres in an extended conformation [136].

# Chapter 4: Liquid-liquid interfaces

## 4.1 Summary

Research devoted to smart interfaces with certain functionalities is predominantly looking at solid-liquid interfaces. However, functionalisation of liquid-liquid interfaces is a merging area just in the beginning of its potential. The processes at such interfaces are still not completely understood to develop applications exploiting the properties of these systems. This argument involves the detailed structure of a liquid-liquid interface and the ion transfer processes, diffusive or due to an external electric field.

Liquid-liquid interfaces reside between two immiscible electrolyte solutions (ITIES). An interfacial zone of a few nanometres contains a Gibbs dividing surface separating phase 1 and phase 2. In general, scientists are looking at systems containing solutions of an organic phase and water, such as nitrobenzene and water. The herein presented work focuses on ATPSs as they offer some advantages compared to organic-phase-water systems. For instance, ATPSs are biocompatible and can be easily stabilised in a microfluidic chip. The advances in miniaturised systems in combination with optical techniques offer new possibilities to elucidate more details of the interfacial transport processes. Further, the possibility to apply an electric field perpendicular to the liquid-liquid interface makes ATPSs outstanding in their stability compared to systems with higher surface tensions as in ITIESs. In oil-water systems the interfacial area strongly tends to minimise itself due to a large surface tension, and a stable interface with a longitudinal direction is difficult to maintain in quiescent conditions even in a microfluidic device.

This chapter introduces into the physical properties underlying in an ITIES in general. All the discussed problems account also for ATPSs. The specific properties of an ATPS consisting of poly(ethylene glycol) (PEG) and dextran are illustrated and the present research concerning the physical understanding of such systems is also summarised.

## 4.2 Ion solvation and consequences

### Introduction

The transfer of solutes from one medium into another has been of general interest for many research areas. Interfacial ion transfer determines the rate of chemical reactions at phase boundaries and transport phenomena across them. For instance, molecular chlorine formation in the atmosphere [137] occurs due to the photolysis of ozone in presence of salt particles [138]. Interfacial transport is also relevant in microfluidic applications as the miniaturisation allows generating larger surface areas in respect to volume to increase the reaction rate of a gas and solutes in a liquid. This is of interest as experiments and simulations show sometimes enhanced reaction rates at interfaces [139]. Solvation is probably the most important criterion in interfacial transport processes as it determines the preference of the solute to one of the phases. In the following, the contribution of solvation to the interfacial ion transport is reviewed. Further, the consequence of an uneven ion partition due to the difference in solvation is discussed. The latter fact results in a potential difference between both phases. The topic is reviewed from an electrochemical and molecular dynamics point of view.

### Gibbs free energy of transfer – the difference in solvation

Firstly, it is important to derive a macroscale approach describing ion transfer in terms of the Gibbs free energy of transfer, which is the difference in solvation that a solute experiences in the transfer between two phases. The classical approach for calculating the Gibbs free energy of transfer of a solute is given by Born and sometimes also denoted as Born energy [140]. The Born energy ($\Delta G_{Born}$) of an ion expresses its partition between two media and is a function of its radius ($a$) and the dielectric properties of the media. The Born energy states the ion solvation energy difference, or Gibbs energy of transfer, considering two media with their respective dielectric

constants $\varepsilon_{r_1}$ and $\varepsilon_{r_2}$. If phase 1 is a vacuum, $\varepsilon_{r_1}$ is considered to be 1. If the relation is $\varepsilon_{r_2} > \varepsilon_{r_1}$, the ion tends to stay in medium 2, regardless of its size. Eventually the Born energy is given in SI units by

$$\Delta G_{Born} = \frac{z^2 e^2}{8\pi\varepsilon_0 a}\left(\frac{1}{\varepsilon_{r_1}} - \frac{1}{\varepsilon_{r_2}}\right) \qquad 4.2.1$$

Some decades onwards the traditional view on the Gibbs energy of transfer of an ion has been extensively revised because the Born theory fails to explain the partition of larger ions where solvophobic effects need to be considered. Certainly for large ions with hydrophobic chains the rearrangement of water molecules causes large hydrophobic effects [33] contributing to the solvation. For this solvophobic effect the Uhlig formula [141] has been found to be appropriate and the Gibbs free energy is represented as a sum of the electrostatic and the solvophobic term [142, 143]. The Uhlig formula states the solvophobic free energy ($\Delta G_{ne}$) contribution as a function of the surface tension and particle surface area. Analogously, this has been shown by Still et al. [144].

In many cases it is sufficient to approximate the surface tension ($\gamma_{1,2}$) of the liquid-liquid interface being independent of the radius. However, Richard Tolman has mathematically shown that surface pressure decreases with the radius ($a$) of a phase droplet [145]. Nevertheless, an approximate solution for the solvophobic term is given by [143]

$$\Delta G_{ne} = 4\pi a^2 \gamma_{1,2} \qquad 4.2.2$$

while $4\pi a^2$ accounts for the surface area of a spherical particle and $\gamma_{1,2}$ is the surface tension of the liquid-liquid interface. Thus, the final Gibbs free energy of transfer ($\Delta G_t$) e.g. of an ion between two immiscible solvents will be considered as a superposition of a dielectric and a solvophobic term. [143]

$$\Delta G_t = \Delta G_{Born} + \Delta G_{ne} = \frac{z^2 e^2}{8\pi\varepsilon_0 a}\left(\frac{1}{\varepsilon_{r_1}} - \frac{1}{\varepsilon_{r_2}}\right) + 4\pi a^2 \gamma_{1,2} \qquad 4.2.3$$

It is obvious from Equation 4.2.3 that for small ions the electrostatic effect dominates over solvophobic effects and the Born model gives approximate values for an estimation.

Under some conditions it has been shown that the Born energy of the aforementioned model is not sufficient to describe ion transfer across liquid-liquid interfaces. Short-range interactions (the dipolar ordering of water around a charge) and others are suggested to contribute to the ion transfer itself. Such theories consider the hydration shell in the process of an ion transfer saying that a hydrophilic ion carries a hydration shell while entering the more hydrophobic (e.g. organic) phase [146, 147].

**The electric potential at liquid-liquid interfaces**

Beforehand it has been shown that ions commonly partition unevenly between two immiscible liquid phases. This partition is determined by the solvation difference contributing to the free energy of a solute or particle. These will prefer the phase where its Gibbs free energy is at a minimum. The uneven partition of ions in two immiscible electrolyte solutions has great impact on the properties of the liquid-liquid interface itself as it causes a potential gradient (Galvani potential) and a back-to-back double layer on each side of the interface with opposing charge. The interfacial electric field due to the potential gradient contributes to the partition.

A herein presented overview summarises the research focussing on organic-phase-water interfaces where uneven ion partition is naturally strong. For an organic phase a variety of alkyl ammonium or alkyl borate salts are available to provide an electric conductivity to an organic phase. For an aqueous phase standard salts as lithium chloride, sodium phosphate and many more are available. Values for the Gibbs free energy of transfer for different ions in a multitude of solvents can be found in Ref. [142].

Verwey and Niessen [148] presented a first model describing the ion distribution at a liquid-liquid interface by two back-to-back double layers according to the previously mentioned Gouy-Chapman approach. Later, the model has been extended by the existence of an ion-free compact layer of solvent molecules separating the back-to-back

double layer. [149-151] The addition of a compact layer into the classical Verwey-Niessen model has been shown to fit better with the experimental data regarding surface tension [152-154] and capacitance measurements [155-157]. However, the characteristics of the compact layer of a liquid-liquid interface are controversially discussed and its structure is not clearly identified. More recent work presumes ion species within the compact layer and some authors identified an overlapping compact layer [158, 159]. Molecular dynamics simulation and X-ray reflectivity measurements of the ion distribution at a nitrobenzene-water interface support the idea that ions are not always clearly separated as predicted by the Gouy-Chapman theory and can be found in the opposing double layer [160].

In respect to all investigations so far, it is essential to stress that the underlying phenomena are strictly dependent on the system properties such as ion type and solvent. Some ions species adsorb at interfaces and some others repel into the bulk [161]. By definition, the ion interactions can be repulsive for structure-making ions or attractive for structure-breaking ions [162]. This means, structure-making ions experience a better solvation in the bulk fluid and repel from the liquid-liquid interface.

The field of electrochemistry has gathered a multitude of data regarding different systems of solutes and solvents that sometimes result in controversies. To call some examples, the capacitance at interfaces of 1,2-dichloroethane and water elucidates differences from the Gouy-Chapman prediction. The mutual solubility of 1,2-dichloroethane and water is presumed to evolve an inner layer of mixed solvent molecules with a capacitance that adds to the differential capacitance of the diffuse layer. On the contrary, 2-heptanone, 2-octanone or 1,3-dibromopropane interfaces with water seem to form specific adsorption due to ion-pairs [163]. In consequence, the solvent properties change the structure of the compact layer and give different potentials. Beside the nature of the solvent, the ionic radius has a major influence on the interfacial differential capacitance. Decreasing radii results in increased capacitance because more charges can occupy the same volume [29].

Kakiuchi et al. found ion adsorption at nitrobenzene-water interfaces in AC polarography experiments [164]. Interestingly, the rate of ion transfer has been found to be dependent on the ion size for different alkylammonium ions. Larger ions are stronger retarded at the interface than smaller ions. Nowadays, the conditions to obtain

adsorption of molecules at an ideally polarized ITIES are identified. Polarized interfaces can be obtained if the ion pair $R^+X^-$ separates into one phase while the other ion pair $S^+Y^-$ separates into the other phase [165, 166]. Recently, such polarized interfaces have been exploited to adsorb various biomolecules [167-171]. In ITIES the choice of ion pairs such as lithium chloride and tetrabutylammonium tetraphenylborate ensures that the former partitions into the aqueous phase and the latter one into the organic phase.

In principle, ion adsorption at liquid-liquid interfaces is possible, if e.g. polarization effects reside at the interface. A theory and simulation of adsorption of ionic species at such polarizable liquid-liquid interfaces has been presented by Su et al. [172]. This work uses the Gouy-Chapman model to describe the potential distribution at the interface. Further, two inner planes are introduced with the condition of electroneutrality. In this inner layer ion adsorption has been theoretically shown to reside.

**The liquid-liquid interface – a molecular approach**

The literature cited in the previous section summarises mainly investigations in the field of electrochemistry and arrives at limitations when trying to explain the molecular structure of an interface. It has been shown how to derive the solvation energy of an ion and how it determines its partition between two immiscible electrolyte solutions. The energy contributions are mainly of electrostatic nature with a solvophobic contribution in such a macroscale approach. Usually, the interface itself is not considered to have further contributions to the solvation. In the world of molecular dynamics some authors included an additional term due to short-range hydration interactions at e.g. a vapour-liquid interface [147, 162, 173]. The outcome of such molecular dynamics investigations is summarised in this section.

The availability of molecular dynamics simulation methods offers a multitude of new confluences giving progress in the molecular understanding of an interface [174]. Liquid-vapour interfaces have been mainly investigated so far, and although they appear to be different from liquid-liquid interfaces, one could claim that they are just different

in the magnitude of the dielectric constant. Most of the underlying phenomena are similar. However, this criterion neglects density gradients, which are expected to contribute to the ion transfer processes across interfaces.

In molecular dynamics the potential of mean force is calculated. This parameter offers a measure of the difference in free energy between two states as a function of one or more given degrees of freedom. In this case, the potential of mean force incorporates the Newtonian motion of a defined number of objects interacting in a defined time scale and volume. The potential of mean force depends greatly on the degrees of freedom chosen for such calculations, e.g. the incorporation of the Coulomb energy and dipole interactions etc. Ions of various types give different results in such simulations, e.g. iodide ion transfer from water to a vapour phase reveals a minimum at the interface on the aqueous side. This has been elucidated by including the polarization of the solute at the interface. This interfacial minimum indicates ion adsorption [175]. Further, in molecular dynamics simulations some molecules show anisotropic diffusivities at liquid-vapour interfaces. On the one hand water molecules and chloride ions show a decreased diffusion perpendicular to the liquid-vapour interface, where the lateral diffusion is not affected. On the other hand sodium ions move more quickly perpendicular to the interface [176].

Beside ion transfer across liquid-vapour interfaces also ion transfer across liquid-liquid interfaces has been of interest, partly because of their relevance for lipid bilayer transport process in biological systems [177, 178]. The recent molecular dynamics simulations are heavily discussing transport processes across liquid-liquid interfaces mainly with a focus on simple systems such as organic phase-water interfaces. As exemplified for vapour-liquid interfaces the ongoing research suffers from controversies and so far no model is available covering the complex dynamics at such interfaces for all parameters (ion type, solvent). Another example for the debates is the fact that large ions like tetramethylammonium crossing a water-nitrobenzene interface apparently strip off their hydration shell when entering the organic phase [30], while small hydrophilic ions tend to keep the hydration shell [146]. Osakai et al. developed therefore a theory involving a term for the short-range interactions contributing to the Gibbs free energy of transfer [147]. In this contribution the squared electric field donates to the short-range interaction energy. Other authors followed this approach concerning vapour-water

interfaces [162, 173, 179] and found, the interactions between ions and the neighbouring water molecules can generate additional short-range interactions, which are either repulsive (for structure making ions) or attractive (for structure breaking ions) [162]. This is supported by experiments measuring surface tension in respect to the ionic strength of a certain ion species. Some ions adsorb at the interface and decrease the surface tension, while others repel from the interface and increase surface tension [161]. Structure-making ions are typically kosmotropic ions of the Hofmeister series such as phosphate, sulphate, sodium or potassium, and structure-breaking ions are chaotropic such as guanidinium or thiocyanate [180].

## 4.3 Surface tension at liquid-liquid interfaces

The surface tension of a liquid-liquid interface of an ATPS is far lower than at interfaces from ITIES, but might contribute to a potential energy minimum a molecule experiences in contact with the interface. For instance, an ATPS of 13% PEG (MW 8,000) and 13% dextran (MW 10,000) attains about 300 μN $m^{-1}$ at the boundary [181], while oil-water interfaces attain a few hundred mN $m^{-1}$. For small phase droplets in another phase of any kind a size-dependence of the surface tension is shown to reside [145, 182]. The issue also might become relevant, if particles adsorb at a liquid-liquid interface and deform the boundary significantly.

It is known for a long time that increased electrolyte concentrations in the bulk increase the surface tension for kosmotropic ionic species, which feel an energy minimum far away from the liquid-liquid interface [161, 183, 184]. Considering the Gibbs adsorption isotherm, the relation of the change in surface tension and surface excess is

$$-d\gamma = \sum_i \Gamma_i d\overline{\mu}_i \qquad 4.3.1$$

while the chemical potential for an ion concerning the activity coefficient ($\gamma_i$) is

$$\overline{\mu}_i = \overline{\mu}_i^0 + RT \ln\left(\gamma_i \frac{c_i}{c_i^0}\right) \qquad 4.3.2$$

Thus, if the increase in the ionic strength in the system results in increased surface tension, the consequence is a decreased surface excess, which means, ions normally repel from the interface. This behaviour is contrary to surfactants and chaotrop ions, which normally adsorb at the interface and decrease surface tension.

The historical models of ion hydration interactions are repulsive for any ion concerning the interface because the ion prefers the medium with a larger dielectric constant to be better hydrated. It has been discussed that moderate electric fields reside at the liquid-liquid interface and decrease the local dielectric constant [140]. Consequently, an ion experiences a better solvation in one of the phases. However, not all ions might behave as suggested from the traditional view, and some ions decrease surface tension as experimentally shown in Ref. [161]. The short-range interactions between the ions and the neighbouring solvent molecules at an interface codetermine whether ions are repelled or adsorbed at interfaces.

## 4.4 Line tension

There is also a contribution of the line tension to a possible energy minimum at a liquid-liquid interface [185, 186]. This line tension is the excess free energy at the three-phase boundary between the molecule or particle and the two liquids or two liquid phases at the three-phase line on a solid substrate [187, 188]. Mainly Van der Waals forces and electrostatic interactions contribute to the value of line tension, but short-range interactions also might be significant. In systems with polymers, the configurational entropy of the polymers at the boundary also contributes to the line tension. Consequently, density profiles at the interfaces are important in calculating line tension [188].

## 4.5 Liquid-liquid interfaces in aqueous two-phase systems (ATPS)

**Polymer partition**

ATPSs can be prepared from two polymers such as poly(ethylene glycol) (PEG) and dextran. PEG separates also from high salt solutions to form two separate phases. Poly(vinylpyrolidone) or Ficoll are polymers that can replace PEG to change the system properties [189].

Initially, it needs to clarify the experimental determinants for separation of two polymers. Albertson and others presented a variety of binodial diagrams for the separation of ATPSs. Such a binodial curve is a measure when phase separation occurs.

A theory for phase separation of two polymers has been proposed by Flory and Huggins [190, 191]. Mixing a polymer in a solvent results in a change in the Gibbs free energy of mixing being a sum of the enthalpy of mixing ($\Delta H_m$) and the product of entropy of mixing ($\Delta S_m$) and absolute temperature ($T$) [41].

$$\Delta G_m = \Delta H_m - T\Delta S_m \qquad 4.5.1$$

Flory and Huggins solved the entropy and enthalpy change

$$\Delta G_m = RT[n_1 \ln(\phi_1) + n_2 \ln(\phi_2) + n_1\phi_2\chi_{1,2}] \qquad 4.5.2$$

where $n_1$ is a function of the number of moles in the volume fraction ($\phi_1$) of component 1 (e.g. solvent), $n_2$ the number of moles in volume fraction ($\phi_2$) of component 2 (polymer) and the introduced parameter $\chi_{1,2}$ accounts for the energy of interdispersing polymer and solvent molecules.

In systems consisting of two polymers in a solvent such as PEG and dextran the Gibbs free energy of mixing is [192]

$$\Delta G_m = RT[n_1 \ln(\phi_1) + n_2 \ln(\phi_2) + n_3 \ln(\phi_3) + (n_1 + n_2P_2 + n_3P_3)(\phi_1\phi_2\chi_{1,2} + \phi_1\phi_3\chi_{1,3} + \phi_2\phi_3\chi_{2,3})] \qquad 4.5.3$$

where number 1 means the solvent and 2 and 3 the respective polymer phase. $P_2$ and $P_3$ denote the relative molecular volumes.

In order to describe the phase separation, a phase diagram (Fig. 8) displays a binodial curve illustrating the polymer content in each phase. From such diagrams it can be elucidated, which amount of a polymer is present in the other polymer phase [193].

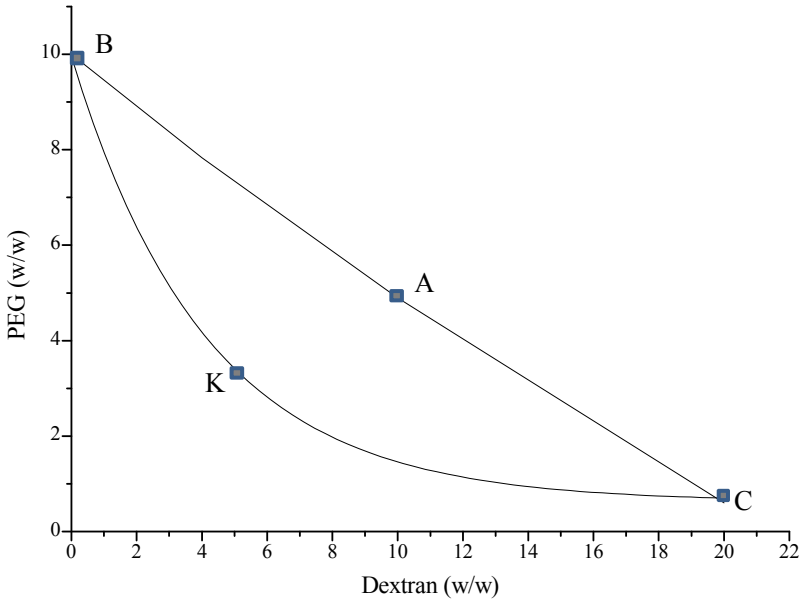


*Fig. 8: Schematic presentation of a phase diagram of PEG/dextran in wt%. Above the binodial curve B-K-C phase separation occurs according to the polymer concentrations. Point A exemplifies a polymer system of 10 wt% dextran and 5 wt% PEG. From the binodial curve it can be estimated that the dextran phase contains here 1.5 wt% PEG.*

**Electrolyte partition**

It has been previously illustrated how ions partition in systems of two immiscible electrolytes driven by the Gibbs free energy of transfer (difference in solvation). The same set of equations can describe the ion partition resulting in a potential difference (Galvani potential) between both phases in an ATPS. The potential difference itself also contributes to the partition, and is, if subjected between two phases of PEG and dextran

$$\Delta\varphi = \varphi^{PEG} - \varphi^{Dex} \qquad 4.5.4$$

For ATPSs such potential differences have been examined with various ions. In general, it has been found that multivalent ions as phosphate and sulphate partition with preference into the dextran phase causing Galvani potentials of about 2-4 mV [194-196] between both phases. For some monovalent electrolytes the Galvani potential has been electrochemically determined and is about 0.3 mV for a Tris/BES buffer [197]. Here the dextran phase is slightly negatively charged. It must be noted that the underlying electrochemical measurements are difficult to accomplish as they are of the order of a liquid junction potential arising at the electrodes. This makes it non trivial to interpret the potentiometric data [198]. Nevertheless, the data gives evidence for a potential difference and for the known ion evaluates the dextran phase as the negatively charged phase for electrolytes such as sodium phosphate/sulphate and Tris buffers [192-195, 197]. The partition of an ion is expressed by the partition coefficient

$$k_i = \frac{c_i^{PEG}}{c_i^{Dex}} \qquad 4.5.5$$

The partition of an ion can be also determined by the equilibrium of the chemical potentials in each phase considering an electrostatic term [192]

$$\bar{\mu}_i^{0PEG} + RT\ln\left(a_i^{PEG}\right) + z_i F\varphi^{PEG} = \bar{\mu}_i^{0Dex} + RT\ln\left(a_i^{Dex}\right) + z_i F\varphi^{Dex} \qquad 4.5.6$$

where $a_i$ denotes the activity of the ion species in the respective phase ( $a_i = \gamma_i\left(c_i / c_i^0\right)$), and $\bar{\mu}_i^0$ is the standard chemical potential of an ion in the respective polymer phase. Most of the ATPS literature favours such an expression. The previously introduced Gibbs free energy of transfer is just one contribution to the partition. Diffusion and electric potential must be considered separately.

Here, the partition coefficient is accordingly

$$\ln k_i = \frac{-\Delta\bar{\mu}_i^0}{RT} - \ln\frac{\gamma_i^{PEG} c_i^{PEG}}{\gamma_i^{Dex} c_i^{Dex}} - \frac{z_i F\Delta\varphi}{RT} \qquad 4.5.7$$

where

$$\Delta\bar{\mu}_i^0 = \bar{\mu}_i^{0PEG} - \bar{\mu}_i^{0Dex} \qquad 4.5.8$$

and $\gamma_i$ is the respective activity coefficient in the polymer phase.

If the potential difference is not known, it must be determined from the partition of anions (-) and cations (+) in the system by the following expression [192]

$$\Delta\varphi = \frac{RT}{(z_+ + z_-)F}\left[\frac{\left(\Delta\bar{\mu}_-^0 - \Delta\bar{\mu}_+^0\right)}{RT} + \ln\left(\frac{\gamma_- c_-}{\gamma_+ c_+}\right)\right] \qquad 4.5.9$$

The expression neglects the presence of a third ion such as DNA that is investigated in the system. Thus, DNA must be present in low concentrations, otherwise it contributes to the potential gradient.

**Properties of poly(ethylene glycol) (PEG)**

PEG is a polymer with *n* repeating units of H-[O-$CH_2$-$CH_2$-O]$_n$-H. Its addition increases the osmotic pressure in cells [199] as PEG has a high affinity to water molecules. Typically this effect is accompanied by a 'salting out' where ions reside in excluded volumes. Eventually, this gives the opportunity to prepare ATPSs of PEG and electrolyte to form a top-phase consisting mainly of PEG and a bottom-phase of aqueous electrolyte. Moreover PEG decreases the dielectric constant of the solution with increasing polymer weight [200].

The ability of PEG on partition with electrolyte giving an aqueous two-phase systems and the prevention of unspecific adsorption of biomolecules at surfaces can be explained by the influence of PEG to the water molecules in its proximity and a repelling force to ionic charges in the local environment [201-204]. There have also been shown attractive forces of PEG to proteins while these attractive forces are present in the short range (2.5-5.0 nm) and repelling forces on the larger range (> 5 nm) for a molecular weight of 2,000 [205]. Besides, the use of pegylated lipids prevents fusion of liposomes [206], which has great impact on the development of new drug delivery systems based on liposomes as PEG increases their life time circulation in blood [207]. Interesting for this study have been investigations showing a repulsive force of PEG on DNA that leads to condensation of phage DNA [208]. The condensation of DNA in high PEG concentrations results in a transition from a coiled to a globular structure [209] and has been exploited for directed partitioning of DNA in ATPSs [203, 210].

The different partitioning enables to separate DNA with a different tertiary structure, such as supercoiled and open circular plasmids. The compaction of λ-DNA due to macromolecular crowding in aqueous PEG solutions has been also investigated by several scientists [211, 212].

Although PEG is very soluble in water it has some hydrophobic character, e.g. it forms thin monolayers at the air-water interface, a behaviour that is normally associated with amphiphilic molecules [213]. This hydrophobic character codetermines the partition of proteins in ATPSs due to the contribution to the Gibbs free energy of transfer. The hydrophobicity of an aqueous PEG solution can be further increased by covalently attached palmitate to increase the affinity of proteins like bovine serum albumin to the PEG phase in ATPSs [214]. Previously, a variety of research concerning ATPSs has been devoted to the partitioning of peptides in respect to the chain length of hydrophobic amino acids [215, 216].

The radius of gyration for a PEG molecule from $r_g = 1.09 \times (MW_{kDa})^{0.5}$ giving $r_g$ in nm and is for a molecular weight of 35 kDa calculated to be 6.4 nm. The relation gives for PEG MW 6 kDa $r_g$ = 2.7 nm [217]. The values do not consider changes in the configurational entropy that may result in a different polymer conformation at high concentrations where the orientational entropy becomes important. Under normal conditions the persitence length is 0.37 nm [218].

**Properties of dextran**

Dextran is a polysaccharide and consists of glucose units where the main chain is connected via α-1,6 glycosilic linkages and side branches either by α-1,3 or α-1,4 glycosilic linkages. A glucose unit has a molecular weight of 180 Da. In general dextran can be synthesized by dextransucrase, an enzyme from e.g. *Leuconostoc mesenteroides* [219]. The structure is coiled in solutions of molecular weights above 2 kDa and rod-like in the lower molecular weight regime [220]. The radius of gyration for a dextran with a molecular weight of 10 kDa is calculated to be 2.9 nm from $r_g = 0.88 \times (MW_{kDa})^{0.5}$ giving $r_g$ in nm [217].

Further, dextran forms complexes with alkali ions such as Fe and is used to treat anaemia [221-223]. Interactions with borate ions are also known [224]. The hygroscopic character leads to an adsorption of water at ambient temperature of about 10 wt% [225]. The dielectric constant in a dextran solution decreases in dextran with increasing polymer content in an ATPS [200].

Koralewski et al. determined the electronic polarizability at frequencies of the visible light of saline dextran solutions obtained from refractive index measurements [226]. The electronic polarizability increases with increasing polymer content and levels off at about 5% (w/w) in aqueous electrolyte. Further, they described a dependence of the polarizability $\alpha$ being proportional to the inverse of the radius of gyration of the polymer ($1/r_g$).

The most interesting parameter might be the electronic polarizability of the glucose units. α-D-glucose, the subunit of a dextran molecule, exhibits a large permanent dipole moment of about 4.5 Debye [227]. It is also known that dextran gets an induced dipole moment in presence of an external electric field. Anhydrous dextran exerts two different dielectric relaxation times [228], a $\beta$- and a $\gamma$-peak. The $\beta$-relaxation process is slower than the $\gamma$-relaxation. Both are ubiquitary present in di- and polysaccharides [229-231]. The interpretation of the $\gamma$-relaxation is rather difficult. Some authors suggest water molecules attached to the glucose units cause the relaxation process [232, 233], while Kaminski et al. explains the drawbacks of this interpretation and refers to reoriented hydroxy groups driving this relaxation process [231]. The $\beta$-relaxation in dextran is related to the rotation of the hydroxymethyl groups and well identified. It is therefore the precursor of a structural relaxation with an activation energy barrier of 85 KJ $mol^{-1}$ [228, 231]. The low $\beta$-relaxation process resides also in other polymers and is accounted for a structural change [234-249]. This interpretation is a result of the dependence of the relaxation process on the concentration of polymers in solution. Satoru Mashimo explains the process with a Kramers reaction rate theory combined with a free volume theory that gained wide acceptance [250, 251].

**Dielectric relaxation of polymers**

The structural changes in anhydrous polymers are a result of the $\beta$-relaxation process occurring at low frequencies in an alternating current. The $\beta$-relaxation is not always identified and its occurrence dependents on polymer type and solvent. But a dielectric $\gamma$-relaxation resides ubiquitary in polymer solutions. The time constant for this process is, similar to the $\beta$-relaxation process, dependent on the polymer concentration, which shows that both processes are restricted by the volume available for a conformational change of the polymer, chemical groups or attached water molecules [238, 250, 251]. A structural change follows the dielectric relaxation in the $\beta$-relaxation process at low frequencies and emerges also in di- and polysaccharides. Further, it has been clearly identified to accompany structural molecular changes also in dextran [230, 231]. The activation energy for the relaxation process in dextran, and thus for a structural change, is about 85 KJ mol$^{-1}$ [228, 231].

The dielectric response function in any polymer is of Kohlrausch type [251]

$$\Phi_k(t) = \exp\left[-\left(\frac{t}{\tau_0}\right)^{\beta_k}\right] \qquad 4.5.10$$

where it applies $0 < \beta_k \leq 1$ and the complex permittivity $\varepsilon^*$ at the high frequency limit is then

$$\frac{\varepsilon^* - \varepsilon_\infty}{\varepsilon_s - \varepsilon_\infty} = \int_0^\infty \exp(-j\omega t)\left(\frac{-d\Phi_k(t)}{dt}\right)dt \qquad 4.5.11$$

where $\varepsilon_s$ accounts for the static, $\varepsilon_\infty$ the limiting high frequency permittivity and $\omega$ the angular frequency. Noteworthy is the existence of a conformational change in the polymer, at least in dextran in an alternating current. This conformational change due to the $\beta$-peak occurs with a time constant of $10^{-4}$ - 10 s depending on the temperature [231].

# Chapter 5: Chip fabrication and experimental techniques concerning liquid-liquid interfaces

## 5.1 Summary

This chapter summarises utilised fabrication techniques, experimental setups and characterises the used microfluidic device to investigate the electrophoretic transport of nucleic acids in an ATPS consisting of PEG and dextran. The setup consists of a polydimethylsiloxane (PDMS) chip bonded to a glass cover slide providing the required optical properties. The microsystem is used for DNA size separation employing an ATPS. Herein a novel separation facility has been achieved. The design properties enable investigations under quiescent conditions.

## 5.2 PDMS micro device for size separation in ATPSs

### Fabrication

SU8 patterned wafers of the specific design have been kindly fabricated via photo lithography by Christine Ruffert (IMT, Universität Hannover, Germany) and Anika Kohlstedt (EMK, TU-Darmstadt, Germany) with two different depths, 70 and 40 µm. The chrome mask for the photo lithography process has been obtained from DeltaMask (Netherlands). PDMS (Sylgard 184, Dow Chemicals) has been used for the fabrication of PDMS casts. The casts are healed at 75°C for 30 min and covered with glass slides of 24 x 40 mm employing oxygen plasma bonding (Diener). To fasten the bonding with plasma activation the microchip has been heated up to 70°C for further 5 min and stored 1-2 weeks at 4°C before use. The storage enables the charge at the surface due to the plasma activation to decline.

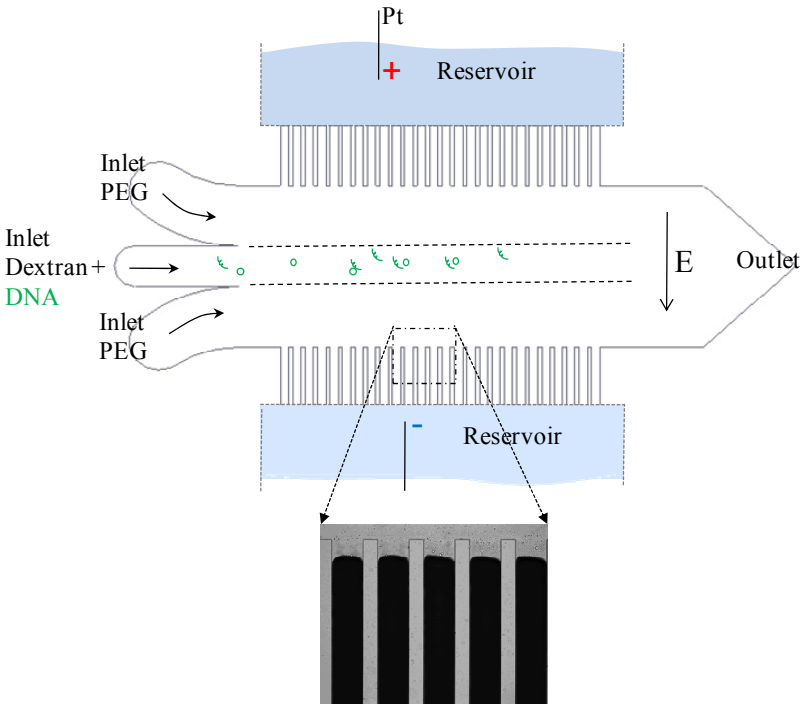


*Fig. 9: Schematic illustration of the PDMS micro device for size separation of DNA in ATPS. The electrodes are placed in two reservoirs separated from the inner compartment by a gel bridge. The gel (black, of 200 µm width) is polymerised between PDMS bars of 100 µm width (white) (blow-up). The comb structure is of 15 mm length. The ATPS polymer solutions are introduced via 3 inlets containing also sample molecules. Under quiescent conditions an electric field is applied perpendicular to the interface.The compartment containing the polymer phases is of 8 mm width and approximately 30 mm length.*

The bonded microchips are silanised with 3-(trimethoxysilyl)propyl methacrylate (Sigma-Aldrich) while preparing a 0.5% (v/v) solution in 50 mM sodium acetate pH 4.0 and keeping the solution for 24 h within the compartment at room temperature. Subsequently, a solution of 18% (w/v) acrylamide, 3% (w/v) N,N-methylene-bisacrylamide and 3% (w/v) dimethoxyphenyl acetophenone (Sigma-Aldrich) is prepared in 2-propanol and introduced into the microchip. The comb structure is exposed with 350 nm for 30-60 s to photopolymerise the acrylamide using a simple mask and a Hamamatsu mercury lamp at 300 W. The lamp is connected with an optical fibre placing it 20 cm apart from the microchip. After the polymerisation process, the microchip is flushed with isopropanol and deionised water, respectively. PTFE tubings for the inlets and outlet are connected to pin holes with stainless steel connectors and fixed using silicon glue (BestKlebstoffe GmbH, Germany). The fabricated microdevices are used as disposables.

The reservoirs are filled with 1 ml of the respective adjacent phase, either PEG, dextran phase or the aqueous electrolyte utilised in the main compartment (Fig. 9).

## 5.3 Experimental set-up

**Set-up for optical tracking of DNA in ATPSs**

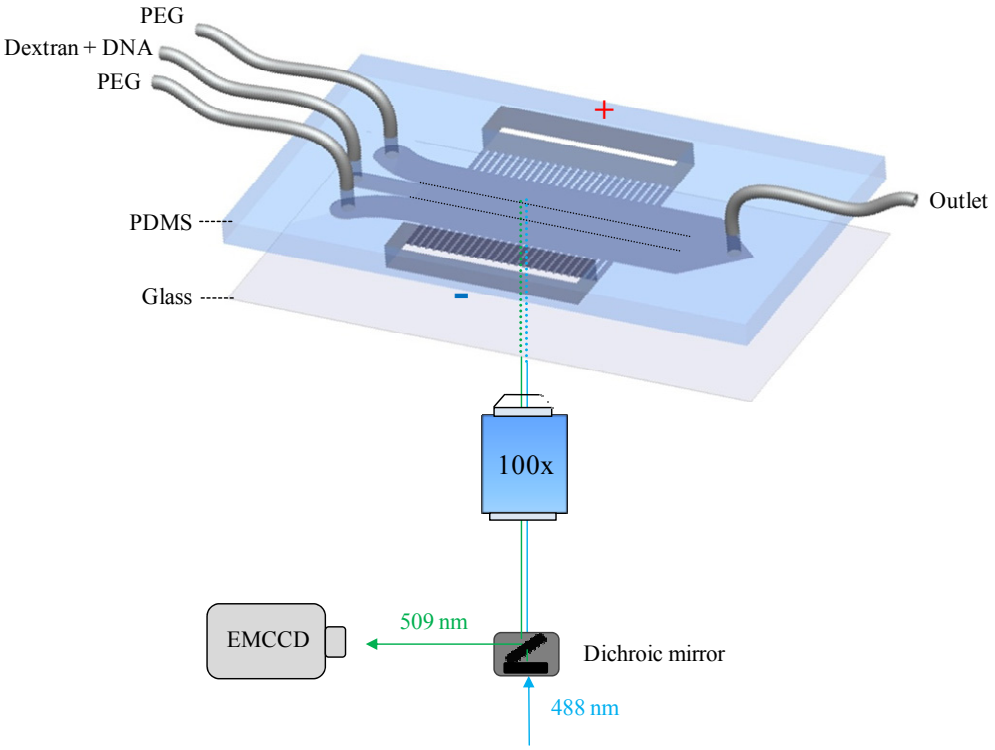


*Fig. 10: Experimental setup. The DNA is excited with an argon laser (488 nm) and a dichroic mirror transfers the emission signal to an electron multiplied charged coupled device (EMCCD).*

Two syringe pumps (KD Scientific, model KDS210) are used to inject the polymer phases or electrolyte. The phases occupy 1/3 of the compartment (Fig. 10) unless otherwise stated. An outlet serves for fluid removal from the other end of the compartment (Fig. 10). The microchip is placed on a stage of the epifluorescence microscope (Nikon, T*i*) and excited with various wavelengths using a diode laser at 405 nm (PicoQuant, PDL 800-D), an argon laser at 488 nm or a helium-neon laser at 543 nm. Dichroic mirrors in a filter block limit the emission spectrum of the specific

dye used and the image is projected to the camera (Andor, iXon 897). Rhodamine B and Cy3 are excited at 543 nm and the emission is detected at about 580 nm. YOYO-1 and fluorescein are excited at 488 nm. YOYO-1 emits with a maximum at 512 nm, fluorescein at 525 nm. For a series of z-slices the optical signal has been transmitted to a confocal unit (C1, Nikon). Quantum dots have been scarcely used and are excited at 405 nm using the diode laser, and the emission spectrum is detected by the confocal scan unit.

## 5.4 Fluorescent dyes and DNA sample preparation

The intercalating fluorescent marker used for DNA experiments is mainly YOYO-1 (Invitrogen, Germany). The ratio of dye to base pair has been 1:4. At higher YOYO-1 concentration significant DNA enlargement is expected [252] and therefore avoided. 1 µl of a respectively diluted YOYO-1 stock solution have been added to 1-2 µl DNA and left for 5 min. Subsequently, dextran with a final volume of 1000 µl has been added to yield the final sample. In general DNA concentrations between 0.33-132 pg $\mu l^{-1}$ have been used and are clearly specified in the result sections.

In experiments using simultaneous two different DNA fragments labelled with Cy3 or fluorescein images are recorded with 1 s of time shift. This time shift has been required to initiate a filter change to track the specific dye. The different labelled DNA fragments of 75 and 300 bp have been synthesized by PCR using Cy3 and fluorescein labelled primers (Metabion GmbH, Germany), and a plasmid vector as template DNA. The PCR has been performed in a common thermocycler provided by Carsten Zeilinger (University Hannover, Germany). The PCR-fragment size has been estimated via agarose gel electrophoresis using a 100 bp-ladder as a marker. Further, single DNA fragments are generated by cutting single fragments from such a 100 bp-ladder, pBR328 (mix) or pUC19 (MspI) DNA ladder (Serva, Germany), are stained with GelStar (Lonza, Switzerland) and visualized on a UV transilluminator exciting at 312 nm. The fragments are recovered using a gel extraction kit (Qiagen, Germany), stored at 4°C and

later used as single additives to the dextran phase. λ-DNA has been purchased from Invitrogen and human male chromosomal DNA from Promega.

If mentioned, rhodamine B labelled dextran (MW 10,000; Sigma-Aldrich, Germany) has been added to the ATPS composition to highlight the dextran phase or rhodamine B is added as an unattached dye to the dextran phase to a final concentration of 1-5 ng $\mu l^{-1}$.

## 5.5 Composition of a standard ATPS

The system utilised in here is prepared using various electrolytes. Mostly sodium phosphate and a Tris borate buffers are used in concentrations between 5-50 mM and pH 7.9-8.0. If not separately noted, an electrolyte concentration of 5 mM is utilised. Importantly, in 5 mM Tris/borate pH 8.0 electrolyte, borate is present in a total concentration of 48 mM, but only 2.78 mM are negatively charged as $[B(OH)_4]^-$.

The PEG fraction consists of two different molecular weights. PEG 6,000 is added to 7.72% (w/w) and PEG 35,000 to 2.28% (w/w). Dextran is added to 12.5% (w/w) at a molecular weight of 10,000. Once the compounds are dissolved in the electrolyte solution with a final weight of 40 g, the system is allowed to separate at 20°C overnight. The fractions are separated as described in [253]. After pipetting the top phase, denoted as PEG phase, into a new tube, the preparation tube is pierced from the bottom to carefully extract the bottom phase (dextran phase). This yields to a volume of the bottom phase of 13.5 ml and the top phase of 24.5 ml and gives roughly a dextran concentration of 35% in the bottom phase and PEG concentration of 15.5% in the top phase neglecting that few percent of polymers partition also into the other phase.

## 5.6 Electrical setup

A software-controlled direct current power supply (QL-355TP, Thurby Thunder Instruments, UK) is connected to platinum electrodes that are placed into the reservoirs

of the microchip. The software enables to establish a time-controlled operation for the potential application for highly reproducible conditions. The multimeter A34410 (Agilent, Germany) records the current for each experiment once per second. The current is either measured in a U-tube of polyethylene or in the microchip itself.

# Chapter 6: Characterisation of the ATPS

## 6.1 Summary

Initially, to start sophisticated evaluations of an electrophoretic DNA adsorption at a liquid-liquid interface, the basic principles as the electric field propagation within the microchip compartment and the ion flux are experimentally determined. In the following, the nonlinear time dependence of the current itself is measured in a microchip and a U-tube.

Further investigations cope with the apparent viscosities adjacent to the DNA molecule in polymer solutions such as a PEG and dextran phase obtained from a standard ATPS. Herein the electrophoretic mobility of DNA in the polymer phase is measured and compared to the expected value from viscosity measurements. The microchip presented in Chapter 5 serves for studying these ATPS characteristics.

## 6.2 Characterisation of the electric field in the main channel

The electric field within a channel is an important parameter of interest if an external potential is applied to a microfluidic device. The fabrication process causes variations in the gel matrix and raises the exigency to determine precisely the electric field strength in each microchip. Therefore, previous to an experiment, the velocity of fluorescently stained λ-DNA has been measured to elucidate the specific electric field strength.

For this purpose, a 45 mM Tris/borate/EDTA electrolyte of pH 8.3 has been prepared. The electrolyte gives λ-DNA an electrophoretic mobility of $4.5 \times 10^{-8}$ $m^2$ $V^{-1}$ $s^{-1}$ in capillaries of 50 µm radius [85], which is close to the dimensions of the microchip. The electroosmotic flow has been minimised due to the silanisation with methacrylate silanes. A potential is applied between 10 - 40 V and the velocity ($u$) of twelve particles is tracked in total to give the electric field strength ($E^{ext}$) using $u = \mu_e \times E^{ext}$. An example

of the curve of the electric field in respect to the potential is presented in Fig. 11. It illustrates the linear dependence.

It is noted that in reference to possibly different electric fields, which might reside in a multiphase system, $E^{ext}$ denotes the herein measured electric field strength in relation to the applied potential for forthcoming experiments.

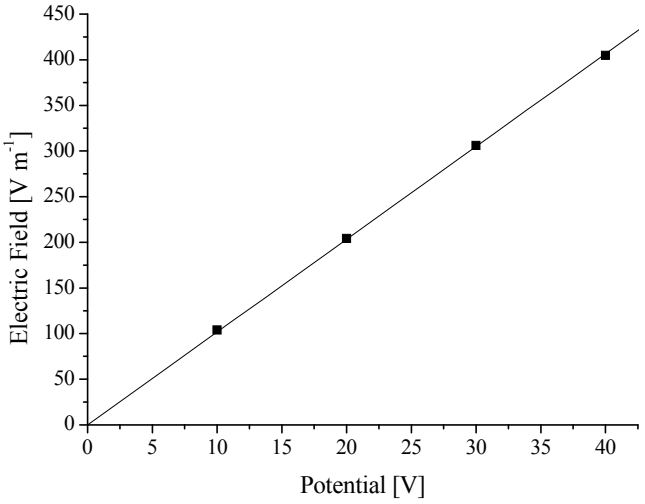


*Fig. 11: Exemplified electric field measurement for 4 different potentials in a microchip ($E^{ext}=10.2\times\varphi^{ext}$).*

## 6.3 Electrophoretic mobility of λ-DNA in a polymer phase

**Comparing micro and macro viscosity**

In order to study an effect due to the presence of large polymer concentrations on the electrophoretic mobility of λ-DNA, it has been motivated to measure the velocity of these molecules in applied electric fields. Volume exclusion effects of polymers such as PEG are extensively described [210, 211, 254-256] and are herein suggested to drive an alteration of the electrophoretic mobility of DNA. Further, the reduced configurational entropy of a dextran molecule in proximity to a particle or cell has been previously described [257-260], which results in a polymer depletion at surfaces. An

electrophoretic mobility that differs from the expected value has been seen as an incidence for viscosity gradients at a particle compared to the bulk solution [260].

In this study it is motivated to measure the electrophoretic mobility of λ-DNA (6.6 pg $\mu l^{-1}$). Beforehand the viscosity of the polymer phase of a standard ATPS prepared in a 5 mM Tris/borate electrolyte is elucidated with a rheometer as described in Chapter 5. The PEG phase exhibits a viscosity of $19.6 \times 10^{-3}$ Pa s and the dextran phase of $22.5 \times 10^{-3}$ Pa s. Further, the electrophoretic mobilities are measured for various applied potentials causing an electric field in the microchip compartment ($E^{ext}$). In a pure 5 mM Tris/borate electrolyte (pH 8.0) the electrophoretic velocity of λ-DNA is linearly proportional to the applied electric field (measured between 100 - 800 V $m^{-1}$). The same applies to experiments if the chip is filled with one of the polymer phase solutions. The electrophoretic mobilities are calculated using the known Smoluchowski equation

$$u = \frac{\varepsilon_0 \varepsilon_r \zeta E^{ext}}{\eta} \equiv \mu_e E^{ext} \qquad 6.3.1$$

The mobility data is given in Tab. 3.

*Tab. 3: Electrophoretic mobility of λ-DNA.*

| System filled with (all pH 8.0) | Electrophoretic mobility $\mu_e$ [$10^{-8}$ $m^2$ $V^{-1}$ $s^{-1}$] |
|---|---|
| PEG phase in 5 mM Tris/borate | -1.25 (± 0.128) |
| dextran phase in 5 mM Tris/borate | -1.14 (± 0.079) |
| 5 mM Tris/borate | -16.35 (± 0.277) |

*Tab. 4: Viscosity data for the bulk polymer phase and the hypothetical micro viscosity at λ-DNA calculated from mobility measurements.*

| Polymer phase | Bulk viscosity $\eta_b$ [$10^{-3}$ Pa s] | Micro viscosity $\eta_p$ [$10^{-3}$ Pa s] | Viscosity ratio $\eta_b / \eta_p$ |
|---|---|---|---|
| PEG | 19.6 | 13.1 | 1.5 |
| dextran | 22.5 | 14.3 | 1.6 |

Considering the measured bulk viscosities in both polymer phases, the DNA molecules migrate faster than expected, if compared to the electrophoretic mobility obtained in pure electrolyte. Applying Eq. 6.3.1 and the boundary condition that the zeta potential remains constant in all polymer phases for all potentials, the determination of the hypothetical micro viscosity and the viscosity ratio is feasible. The viscosity data is summarised in Tab. 4 and suggests a depletion layer around a DNA molecule.

**The thickness of the hypothetical depletion layer**

It has been envisaged to measure the electrophoretic mobility in electrolyte and polymer phases prepared in different ionic strengths.

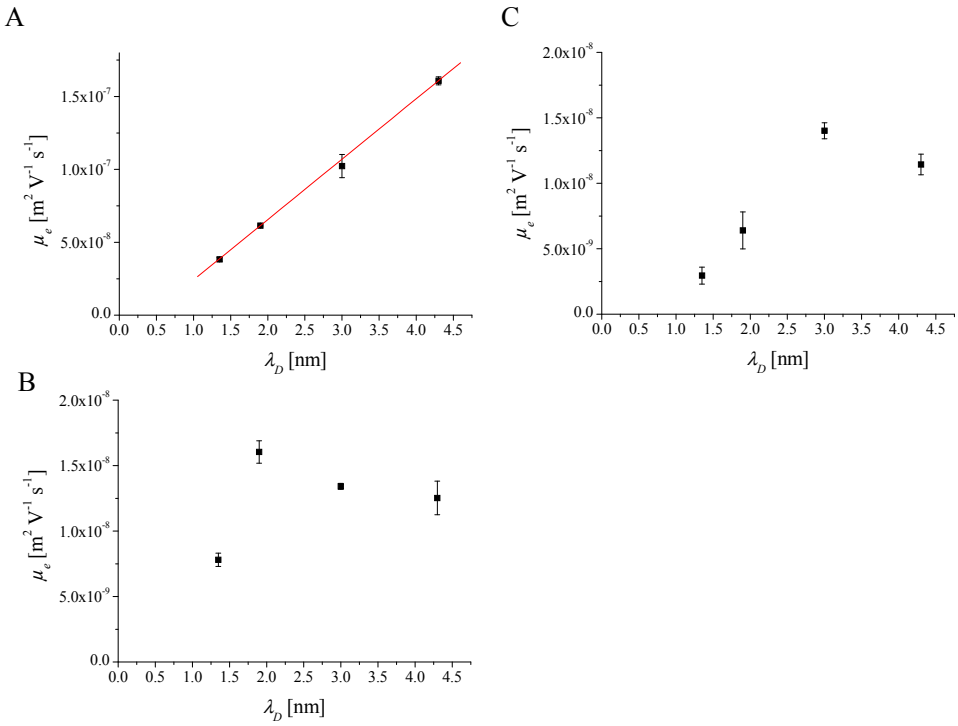


*Fig. 12: The electrophoretic mobility of λ-DNA has been measured in different molarities of Tris/borate electrolyte pH 8.0 (A), PEG phase (B) and dextran phase (C) prepared in the same electrolyte. In pure electrolyte the mobility follows linear the length scale of the corresponding Debye length, while for the polymer phases a sharp transition occurs at certain $\lambda_D$. It is speculated, if $\lambda_D$ is larger than the supposed polymer depletion layer, an increased friction reduces the electrophoretic mobility.*

The electrophoretic mobility of λ-DNA shows in the PEG and dextran phase a sharp transition, where it does not increase linearly with the Debye length as it is measured in pure electrolyte (Fig. 12A). In the PEG phase this transition occurs at 2.0 nm (Fig. 12B) and in the dextran phase at 3.0 nm (Fig. 12C). The Debye length has been estimated assuming $\varepsilon_r = 78$ and $T = 293$ K. It is suggested that at larger $\lambda_D$ a greater electroosmotic slip resides at a DNA molecule and the electrophoretic mobility is increased. This could explain the linear increase of the electrophoretic mobility in respect to $\lambda_D$. It may be speculated, if $\lambda_D$ is larger than the supposed delpetion layer, a larger friction coefficient reduces the electrophoretic mobility as proposed for spherical particles [261].

## 6.4 Electric current in polymer phases of an ATPS

**Purpose of current measurements**

The ion flux at certain applied potentials allows some qualitative statements to estimate the electric properties of the system. The system is defined by polymer phases subjected to the microchip. This section identifies the ion transport in the polymer phases within and outside of a microchip.

**Current-time dependence in one or more polymer phases in a microchip**

Firstly, the ion flux in each single polymer phase needs to be quantified under quiescent conditions in the PDMS-glass microchip. The experiments reveal representative measures of the current through a dextran and a PEG phase for an electric field that resides in the compartment of $E^{ext}$ = 94 V m$^{-1}$ and $E^{ext}$ = 141 V m$^{-1}$. In these experiments, the single phase, either PEG or dextran phase, is introduced into the same microchip in absence of DNA. The reservoirs are filled with the same polymer phase as in the compartment to achieve a system with homogenous conditions. Nevertheless, it has been found that no considerable electrode effects are present. This is performed by

introducing a 5 mM Tris borate pH 8.0 electrolyte into the reservoirs while the compartment is filled with a polymer phase. The current-time dependence keeps its characteristic decay. Fig. 13 shows a representing measure of the current in a single PEG and dextran phase introduced into the microchip and exerted to moderate electric field strengths in the compartment.

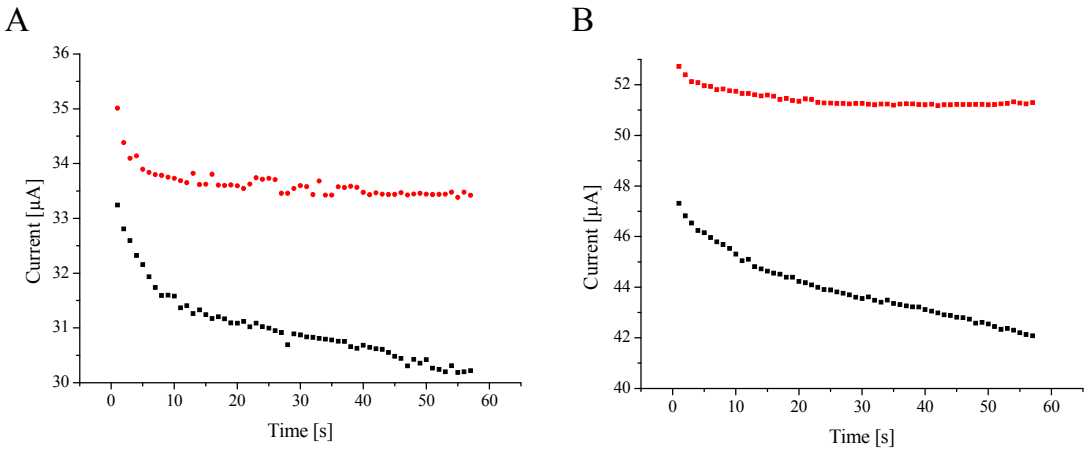


*Fig. 13: Currents for $E^{ext}$ = 94 V $m^{-1}$ (A) and 141 V $m^{-1}$ (B) in a single PEG phase (●) or dextran phase (■) introduced into a microchip. The dextran phase exhibits a decreasing current with time.*

The major phenomenon that requires attention in Fig. 13 is the decay in the current with time, appearing dominantly in the dextran phase for moderate electric fields. The PEG phase provides a constant current, with the exception of a small exponential decay in the beginning of a potential application. This accounts for electric fields $E^{ext}$ until ≈ 150 V $m^{-1}$. Within the chosen experimental parameters the decay of current in a dextran phase is independent of the reservoir volume, which has been determined comparing 1 and 5 ml dextran phase within the reservoirs. Therefore the decreasing current cannot be ascribed to electrolyte depletion within the reservoirs.

Remarkably, the PEG phase changes its current-time characteristics, if the electric field increases above ≈ 200 V $m^{-1}$. For large electric fields, the current decays even more than in the dextran phase introduced into a polymer chip as single phases (Fig. 14).

The decreasing current in respect to time is supposed to be an important parameter that requires a fundamental understanding to ensure a correct interpretation of the results concerning interfacial electrokinetic phenomena shown in subsequent chapters. The

decreasing current in the dextran phase in respect to time shows a decreasing conductivity of the entire system. Moreover, the conductivity of the PEG phase is initially larger than for the dextran phase. It is emphasised that this accounts for polymer phases present in the microchip setup including gel bridges.

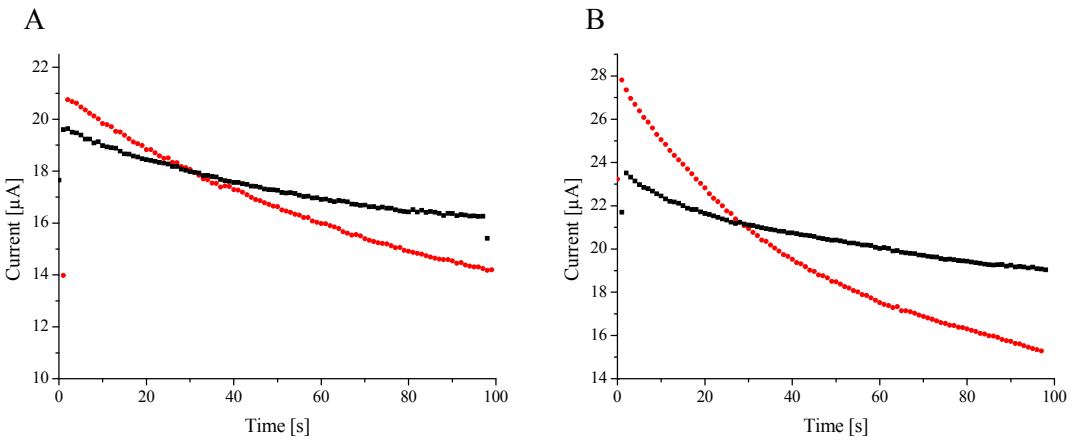


*Fig. 14: Currents for $E^{ext}$ = 570 V $m^{-1}$ (A) and 712 V $m^{-1}$ (B) in a pure PEG phase (●) and dextran phase (■) introduced in a microchip are shown. At large field amplitudes the PEG phase exhibits a larger slope of the current decreasing with time.*

**Current-voltage characteristics in one or more polymer phases in a microchip**

Beside the time dependence of the current the current-voltage (*I-V*) characteristics of a single polymer phase introduced into the microchip reveals a non-ohmic behaviour. Different potential values have been applied to measure the current over a time for 100 s. The currents at 30, 60 and 99 s are plotted in Fig. 15 for different polymer phases, when the reservoirs contain the same polymer phase as introduced into a microchip compartment. The data of Fig. 15 has been recorded in different microchips with different cross sectional areas.

The trend of the current in respect to the applied potential illustrates the non-ohmic character of the resistance of polymer phases in a microchip. In pure electrolyte the current is linearly following the applied potential. Experiments with a dextran phase in the microchip compartment show an increasing conductivity in respect to the applied potential, while the PEG phase exhibits a decreasing conductivity. These characteristics

remain present, if the reservoirs are filled with electrolyte. Hence, the polymers do not contribute to considerable electrode effects.

Eventually, it needs an explanation for the non-ohmic behaviour of a polymer phase in the microchip compartment. This requires another experimental setup that looks at the current-voltage behaviour of a polymer phase outside of a microchip to investigate the source of the non-ohmic resistance. This is highlighted in the following section.

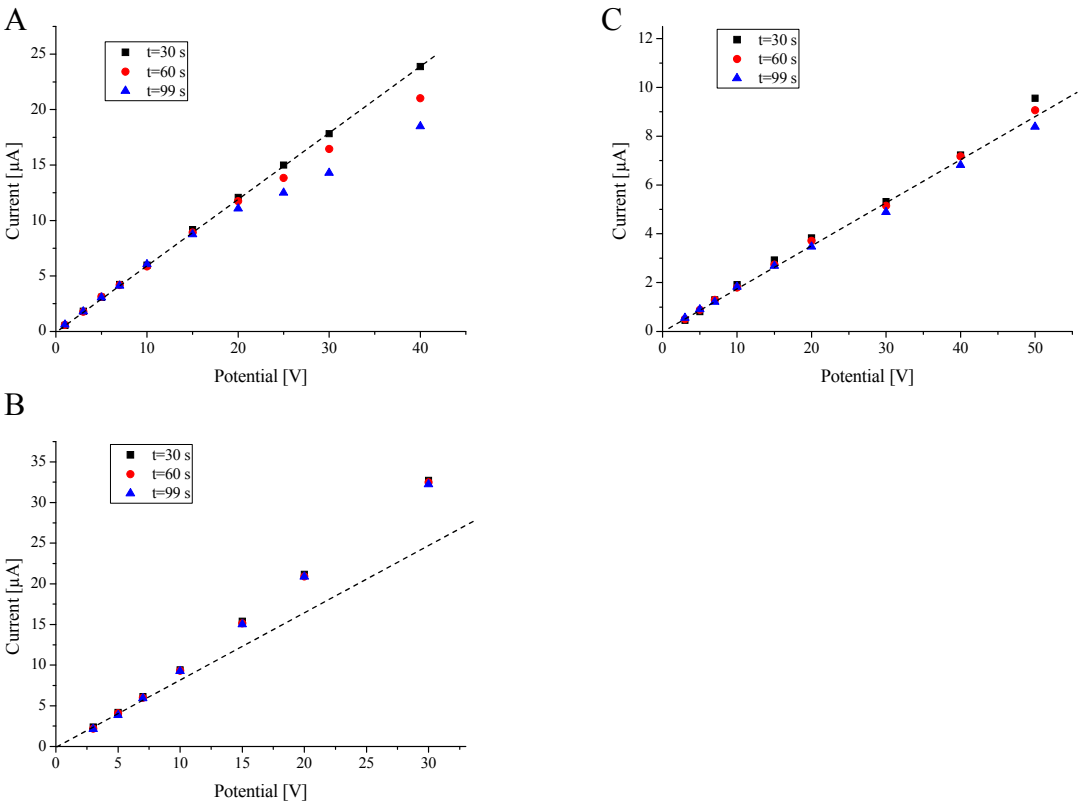


*Fig. 15: The current at different applied potentials shows nonlinear I-V characteristics for different polymer phases. PEG phase (A), dextran phase (B) or 5 mM Tris/borate electrolyte (C) have been introduced into the microchip. The dashed line depicts the expected plot from an ohmic behaviour. The current in the polymer phases is non-ohmic, in electrolyte ohmic.* $E^{ext} = 15 \times \varphi^{ext}$

**Current-voltage characteristics of the polymer phases in an U-tube**

Determining the contribution of the polymer phases to the nonlinear behaviour of the conductivity examined in the previous section by subjecting the polymer phase to a

microchip, it requires a detailed analysis of the conductivities of a polymer phase placed within a tube of polyethylene. The setup ensures to measure the current-voltage behaviour of a polymer phase outside of a microchip compartment without any effects exerted from the gel-bridges. A platinum electrode is placed on each end of the tube that is formed to a U-shape and filled with either electrolyte or a polymer phase. The tube has a radius of 0.385 cm and length of 15 cm. The current at different applied DC potentials is followed for 100 s and plotted against the electric field strength that resides in the tube.

The ohmic behaviour of the current is illustrated in Fig. 16 for the dextran phase (A) and the PEG phase (B). The data shows that the previously found non-ohmic behaviour of the polymer phases is an effect of the polymers in combination with the gel bridges in a microchip. The U-tube does not contain any gel bridges and the current remains linear over time and for different applied electric fields. The same is observed with pure electrolyte. Fig. 16 indicates polarization effects at the platinum electrodes as the current does not follow the linear trend at very small electric fields.

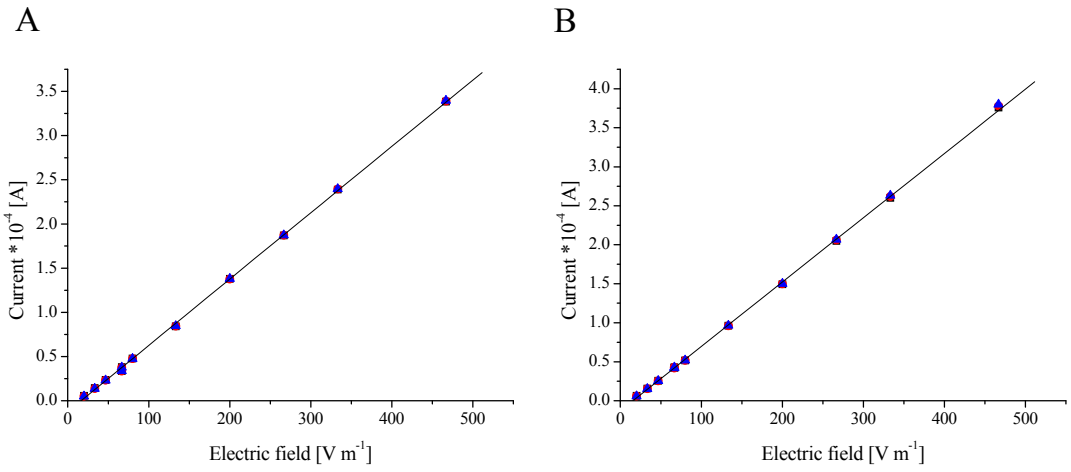


*Fig. 16: Current in a U-tube filled with dextran phase (A) or PEG phase (B). The current in the polymer phases follows a linear behaviour in respect to the applied electric field ($\varphi^{ext} = E^{ext} / 6.67$). Currents are measured at 30 s, 60 s and 90 s using same symbols as in Fig. 15.*

**Reverse current of polymer phases in a microchip**

Eventually, if once the applied DC potential is switched off, a reverse current is measured, bringing the system back to equilibrium. The reverse current decays exponentially from a few µA at 100 s and declines to zero within 1 minute (Fig. 17). For a single polymer phase or just electrolyte this phenomenon is ubiquitary present and typical for any capacitor and resistor in series. The applied potential can be estimated from the given electric field strength in the major compartment by $\varphi^{ext} = E^{ext}$ / 15.3 as depicted in Fig. 17 and Fig. 18. The illustration of currents for different electric fields has been chosen to simplify the comparison with the following experimental data. In order to compare the time constant at different applied potentials in a real system with a liquid-liquid interface, the current is measured in a three-phase system where a dextran phase is surrounded by PEG phases. Each phase occupies 1/3 of the compartment. Next, the effect of DNA in such a three-phase system is studied while the current is measured with addition of DNA into the dextran phase. For lower applied potentials, λ-DNA in concentrations of 6.6 pg µl$^{-1}$ in a dextran phase shows a decreased current compared to a three-phase system of PEG-dextran-PEG in absence of DNA (Fig. 18).

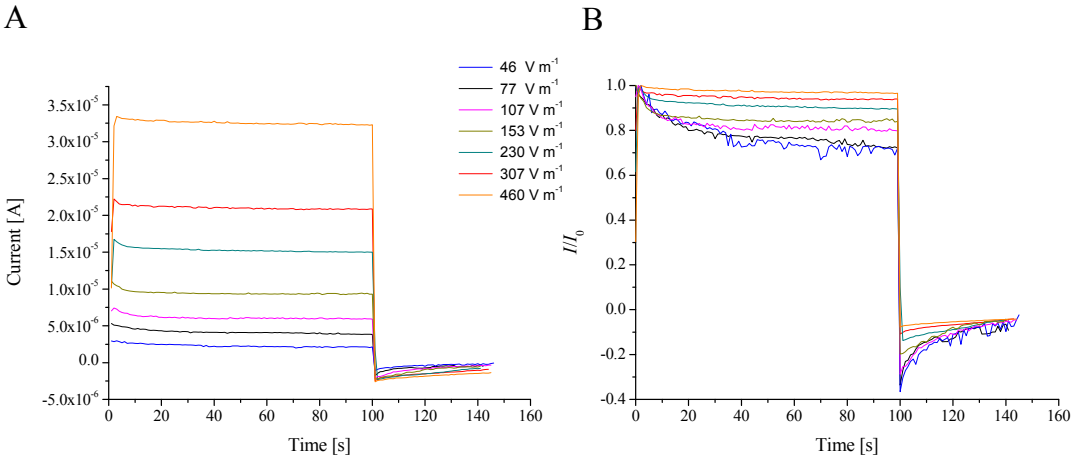


*Fig. 17: Current in a single dextran phase of an ATPS introduced into the microchip and measured under quiescent conditions (A). The curves are normalised to the maximum at the beginning of the potential application and reveal the dependence of $I/I_0$ according to $E^{ext}$ and time (B).*

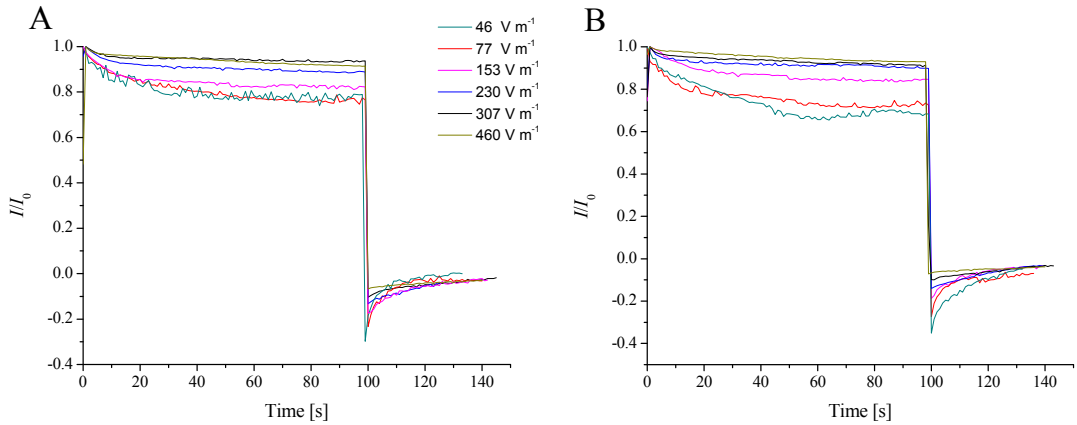


*Fig. 18: Normalised currents for an ATPS with a dextran phase surrounded by PEG phases occupying each 1/3 of the compartment without (A) and with 6.6 pg µl$^{-1}$ λ-DNA (B). The addition of λ-DNA in the dextran phase causes a stronger decay in the current, certainly for low electric fields.*

**The time constant of the current in a microchip**

The reverse current is used to determine the time constant ($\tau$). For simplification, the reverse current as a discharge current in a circuit with a resistor and capacitor in series is considered. Fig. 18 presents the current at different applied electric fields and the reverse current at 100 s, when the potential is switched off. The time dependent discharge current is then

$$I(t) = I_{\max} \exp\left(-\frac{t}{\tau}\right) \qquad 6.4.1$$

where $I_{\max}$ is the value when the discharge process starts at 100 s (Fig. 19) as the applied potential is switched off. It is also observed that 6.6 pg µl$^{-1}$ DNA contributes to the capacitance of the system.

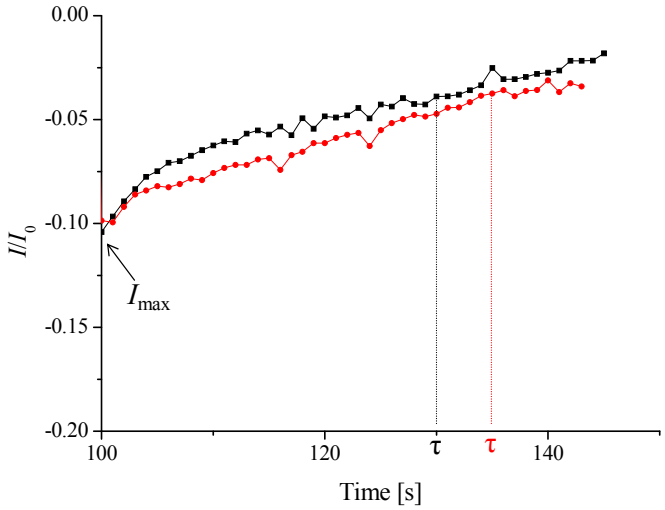


*Fig. 19: Illustration presenting the estimation of τ with (●) and without (■) added DNA in a dextran phase of a three-phase system and an applied potential of 20 V.*

The time constant ($\tau$) is the time when the absolute value of the discharge current decays to $I_{max}$ / e (≈ 37 % of the initial value). Once $\tau$ is evaluated from the data in Fig. 17 and Fig. 18, the relation $\tau = R \times C$ can be used to estimate these parameters of the entire system. The resistance ($R$) in a single dextran phase and also in a three-lamellae configuration is about 10 V / $10^{-5}$ A = $10^{6}$ Ω in the microchip where the experiments of this section have been performed. The parameter $C$ represents the capacitance.

This ideal relation can just give a qualitative estimation of a capacitance and resistance, and how it evolves in the system involving the parameters revealing different $\tau$ in Fig. 20 increasing almost linear with the electric field for the applied potential range. It is further emphasised that the time constant evaluated here describes the properties of the entire system and therefore, it cannot be directly accounted for the electrokinetic phenomena at the liquid-liquid interface.

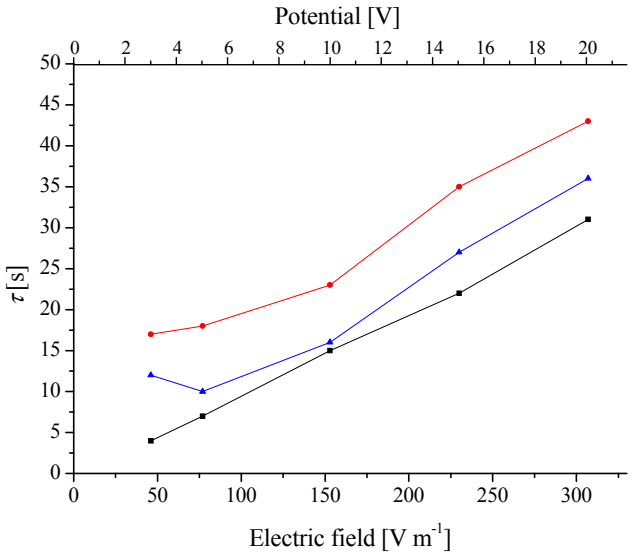


*Fig. 20: τ in seconds in respect to the applied electric field/potential in a single dextran phase (●), three-phase system PEG-dextran-PEG (■) and three-phase system containing 6.6 pg µl$^{-1}$ λ-DNA in the dextran phase (▲).*

## 6.5 The interfacial electric field – a parameter of great interest

**Summary**

In order to understand the contributions to a potential energy minimum at a liquid-liquid interface where the molecules may get trapped, the interfacial electric field is of great interest. In a simple view the Galvani potential between both polymer phases could be used to derive the electric field in respect to the calculated Debye length of the interfacial back-to-back double layer. This might be not sufficient to explain the interfacial electric field, e.g. if a polarization potential must be considered. Other non-discussed phenomena could also contribute to an interfacial potential minimum and a theoretical picture might not include all relevant terms. Therefore it is of high interest to find experimental setups revealing the interfacial electric field. In spite of the difficulties that rose in the following some methods are illustrated and the suitability for interfacial electric field measurements is discussed. Eventually, it is shown that all

illustrated methods have drawbacks and a good estimation for the interfacial potential or electric field remains desirable.

**Electrophoretic mobility of liquid phase droplets in another liquid phase**

In view of the principles concerning electrophoresis of particles, the simplest way to investigate surface potentials is the measurement of the particle velocity under an applied electric field. The Smoluchowski equation is utilised to determine the electrophoretic mobility and zeta potential. An electroosmotic slip at the boundary of a solid particle drives its electrophoretic motion [47].

In contrary, the electrophoretic mobility of liquid phase droplets is not easily used to derive a surface potential as done for solid particles. Firstly, the electrophoretic mobility of a polymer phase droplet of an ATPS opposes the expected direction derived from data concerning Galvani potentials acquired with electrochemical methods. The electrochemical measurements clearly show a negatively charged dextran phase compared to the PEG phase for most of the electrolytes used for ATPS preparations, such as sodium phosphate or Tris/BES buffers [192, 194, 195, 197]. Vice versa, dextran phase droplets migrate towards the cathode [194]. The electrophoretic mobility of such droplets is also linearly dependent on the droplet radius [192, 194, 262-264], which increases the complexity of the problem. Some authors observed even a nonlinear dependence of the droplet velocity in respect to the applied electric field [262].

For liquid phase droplets in another liquid phase so far no theory covers all parameters. In simulations, Baygents and Saville illustrate under which circumstances an opposing electrophoretic mobility can be present and how the mobility is dependent on the droplet radius [265]. A reversed electrophoretic mobility may come from different sources, such as impurities resulting in Marangoni slip or polarization of the double layer. Ohshima et al. have presented a theory explaining the mobility of mercury droplets owing to droplet polarization [266]. In ATPSs and under the given chemistry data impurities are very unlikely for the reported experiments, also because the data concerning mobility measurements in the literature [192, 194, 262-264] coincides with

each other although different batches of chemicals are used. If impurities are present, different data was expected, such as for the zeta potential of PMMA [267].

Nespolo and co-workers developed a theory determining the electrophoretic mobility of decane phase droplets in an aqueous environment [268]. In their case, they used different concentrations of a surfactant and compared, among others, surface tension data with the surface excess of the surfactant and the corresponding mobility. The theory has not been proven to account also for ATPSs.

Nevertheless, the performance of experiments to reveal the electrophoretic mobility of polymer phase droplets of an ATPS can be still constructive and a few experiments are described in the following. For this purpose, an applied electric field of 1073 V $m^{-1}$ in the microchip initialises the migration of dextran phase droplets. The droplets have been generated by applying a very slow flow of dextran surrounded by two fast PEG flows. The enclosed dextran phase disrupts into droplets and the flow of all lamellae is stopped to apply the electric field under quiescent conditions.

The electrophoretic mobility of dextran phase droplets has been measured for 5 and 50 mM Tris/borate pH 8.0 standard ATPSs. It must be noted that dextran phase droplets suffer from friction at the glass slide due to a higher density than the PEG phase. Certainly, lower electric fields do not initiate a droplet migration because the droplets do not overcome a critical momentum necessary to initialise migration. Electrophoretic mobility measurements of such phase droplets require more sophisticated setups that diminish the problem of surface friction as presented in Ref. [262-264]. Still, the direction of migration is of interest of an ATPS in Tris/borate electrolyte.

Dextran phase droplets from ATPSs prepared in 5 - 50 mM Tris/borate pH 8.0 show a positive and PEG phase droplets a negative electrophoretic mobility, meaning dextran phase droplets migrate towards the cathode and PEG phase droplets towards the anode. Thus, the Tris/borate ATPS concurs qualitatively with the behaviour of sodium phosphate buffered ATPSs [194]. The dependency on the radius is also observed although beyond 50 µm droplet diameter the electrophoretic mobility levels off in the presented experiments (Fig. 21). This phenomenon might be due to the confined compartment in the microchip of ≈ 70 µm height or the settling effect, which gives a deviation from a spherical structure. For droplet radii smaller than 45 µm the

measurements concur with the literature where the electrophoretic mobility decreases with decreasing droplet size [192, 194, 262-264].

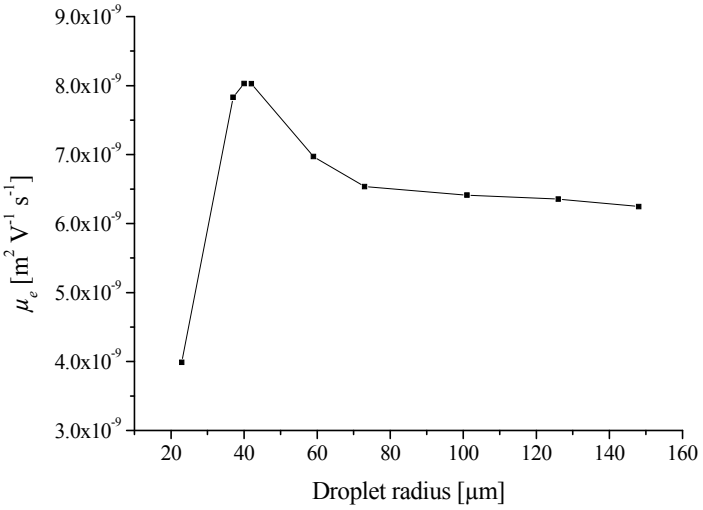


*Fig. 21: Dextran phase droplets in a PEG phase of a 5 mM Tris/borate pH 8.0 standard ATPS show a dependence of the radius on the electrophoretic mobility. The microchip height is ≈70 µm.*

The electrophoretic mobility of droplets of the polymer phases enables to perform electrophoretic segregation of an ATPS. This has been shown by several authors. [262, 269] Remarkable is the fact that apparently the segregation process with view onto the electrophoretic mobility is dependent on the electric field strength [262].

**Circulations in dextran phase droplets**

It has been mentioned that under low electric field strength, the dextran phase droplets do not initiate a migration expected due to friction at the glass surface where a dextran phase droplet settles. This property is exploited to measure the inter-droplet flows at the steady dextran phase droplet. By previously flushing the tube with the PEG phase followed by a dextran phase, the generation of a dextran phase droplets that contain another PEG phase droplet has been elaborated. An electric field of 614 V $m^{-1}$ keeps the dextran phase droplet quiescent at its position while the inner PEG phase droplet circulates in one half of the dextran phase droplet. The circulation is depicted in Fig. 22

by squares illustrating the position of the PEG phase droplet each 0.5 s for a complete circulation at the beginning of the experiment.

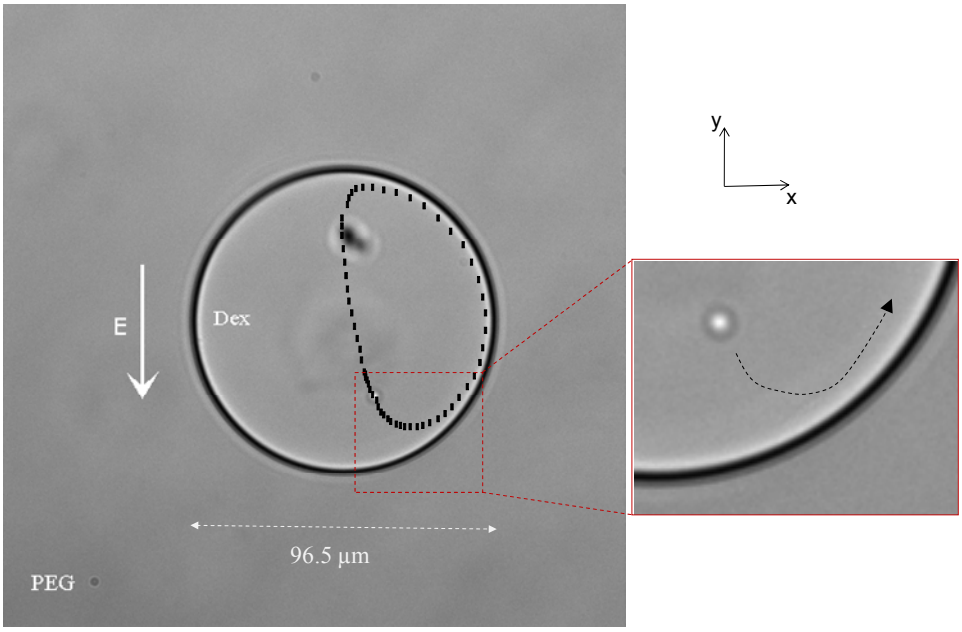


*Fig. 22: A little PEG phase droplet is trapped within a dextran phase droplet. The dextran phase droplet is trapped in the compartment and remains quiescent for low electric fields. The little PEG phase droplet circulates in the second half of the dextran phase droplet due to the presence of an electric field. (2 frames/s)*

The circulation radius decreases with the time. The time for a complete round is initially 30 s and levels off at the 6$^{th}$ circulation to 22 s. The acquired data suggests a nonlinear behaviour of the system. The recirculating eddies in a viscid droplet have been previously described by Baygents and Saville [265]. There it is shown, that non-viscid droplets experience an interfacial polarization and show reversed electrophoretic mobilities. Viscid droplets may also show reversed electrophoretic mobilities. If Maxwell stress and electrokinetic stress counterbalance, Baygents and Saville suggested Marangoni convection to reverse droplet mobilities, because of one-sided adsorption of ions or impurities.

**Mass transfer across the liquid-liquid interface**

The diameter of the dextran phase droplet (Fig. 22) has been measured in respect to the time. Noteworthy, the apparent size of the dextran phase droplet decreases in x and y-direction (Fig. 23). The z-plane has been assured to be constant by the microscope display giving the z-coordinate with an accuracy of 50 nm. The temperature has been maintained in an air conditioned room at 20°C. Hence, the decreasing size of dextran phase droplets can be only explained by either a loss of mass or a significant change of the curvature of the liquid-liquid interface that gives an apparent change in the droplet diameter in the focal plane. The latter one is unlikely due to confocal measurements that reveal a contact angle deviation within the experiments leading to smaller shifts.

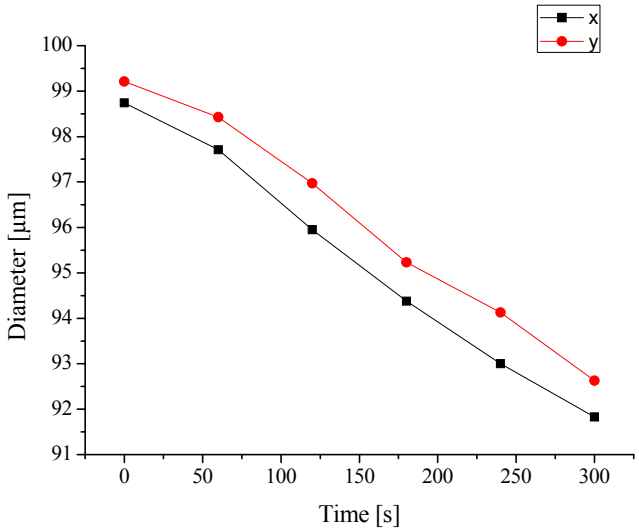


*Fig. 23: The dextran phase droplet size decreases with time.*

The loss of mass is conceivable because a dextran lamella sandwiched between two PEG lamellae reduces its width significantly with time, if an electric field is applied perpendicular to the liquid-liquid interface. In such an experimental setup it has been difficult to argue whether exerted fluid stress is responsible for a phase ordering with time or really a mass transfer occurs. But the decreasing dimensions of a dextran phase droplet coincide with the idea of mass transfer occurrence across the interface. Recently

a report has elucidated a moving boundary of a polarized liquid-liquid interface if an electric field is applied [270].

**Stark shift in electrostatic fields**

It has been theoretically proposed by Flatté et al. to elucidate the electric field strength that resides at a liquid-liquid interface by examining the Stark shift of quantum dots [271]. Quantum dots change their emission spectra in respect to the electric field strengths, to which they are subjected [272]. Such electric fields can be applied by an external source or due to the presence of an electrostatic energy at a charged interface.

Quantum dots (Invitrogen, Q10101MP) with an emission of 605 nm have been exited using 405 nm while prepared in the polymer phases PEG and dextran and introduced into the PDMS-glass microchip in a two-lamellae configuration. The larger density of the quantum dots enable them to settle at the lower glass substrate of the microchip.

The adsorbed quantum dots at the glass surface exert a different emission spectrum than quantum dots in the bulk of a dextran phase (Fig. 24). However, it has been impossible to obtain a different emission spectrum of quantum dots at a liquid-liquid interface compared to the ones in the bulk solution. Large zeta potentials of about -50 mV reside at glass surfaces [273]. The known Galvani potential between two polymer phases in an ATPS is ≈ 2 mV and probably too small to generate significant electric fields that may alter the emission spectrum of the quantum dots. Moreover, it has been difficult to obtain a signal just from the interface as the region is only of a few nanometres.

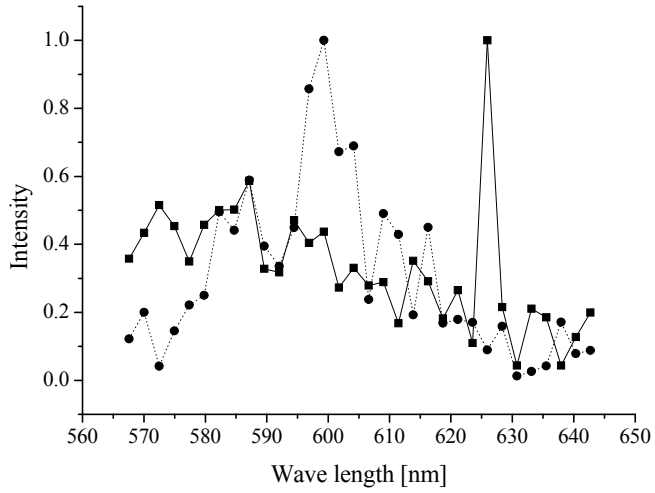


*Fig. 24: The emission spectrum of quantum dots 605 at a glass substrate (solid line) differ significantly from quantum dots in the bulk of a polymer phase (dashed line).*

## 6.6 The contact angle of the liquid-liquid interface

Previous experiments of dextran phase droplets in a PEG phase indicate an apparent loss of mass. Hence, it has been motivated to acquire a series of z-slices with the confocal microscope and reveal the contact angle of the interface to the glass and PDMS surface. The objective has been to measure the interfacial tension with such a technique to reveal more details of the liquid-liquid interfacial character.

For highest accuracy, the 100x oil immersion objective with a numerical aperture of 1.49 and a confocal microscope setup is used. The polymer phases are introduced in a three lamellae configuration. A great difficulty under the experimental setup is to keep the liquid-liquid interface stable at its position. The z-series recording requires about 30 s and a migration of the interface even for a few micro metres results in deviations while an electric field is applied. The dextran phase has been initially prepared with a 1 $\mu g\ ml^{-1}$ rhodamine B labelled dextran (MW 10,000) and introduced with a width of 300 µm between two equal PEG phases. The optical setup focuses on the liquid-liquid interface that is closer to the anodic side, where an adsorption of negatively charged biomolecules is investigated. The data is analysed by NIS Elements AR (Nikon)

drawing a circle along the liquid-liquid interface and measuring the contact angle to the glass substrate as depicted in Fig. 25.

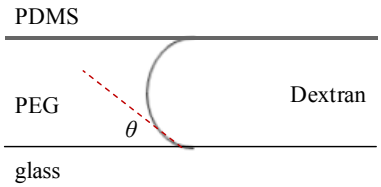


*Fig. 25: Schematic presentation of the contact angle of the liquid-liquid interface (θ).*

The contact angle of the liquid-liquid interface (Fig. 25) has been measured at $E = 0$ V m$^{-1}$ being about 24° and for 60 s applied $E = 154$ V m$^{-1}$ being about 29° at the glass surface, which is the lower border in Fig. 26. The data error of 6° that has been derived from three measurements is still too large to obtain a significant difference in the contact angle. Further, it has not been possible to prove whether a possible change in the contact angle is not due to interfacial stress caused by the interface migration in applied electric fields. A dextran lamellae surrounded by two PEG phases always thins out over an experimental period. This can be attributed to a loss of mass as previously suggested (Fig. 23). The migration of the interface exerts a fluid stress onto the liquid-liquid interface and does not enable to relate the change in the contact angle to the applied electric field.

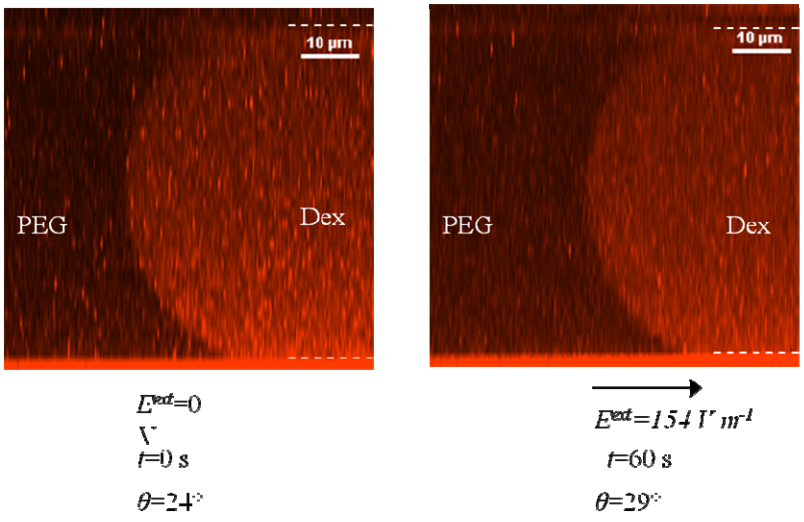


*Fig. 26: Curvature of the interface of a PEG-dextran ATPS in 5 mM Tris/borate electrolyte. The contact angle to the glass surface is at $E^{ext}$=0 θ=24° and at $E^{ext}$=154 V m$^{-1}$ θ=29°. The large deviation of about ±6° does not indicate a significant change between both states.*

Nevertheless, experiments measuring the contact angle might give an idea about changes in the interfacial tension due to a possible ion adsorption. In general this becomes obvious, if the Gibbs adsorption isotherm is considered. The Gibbs adsorption isotherm explains the change in surface tension due to a change in the chemical potential and the surface excess concentration ($\Gamma_i$) [21]

$$-d\gamma_{Dex,PEG} = \sum_i \Gamma_i d\bar{\mu}_i \qquad 6.6.1$$

The surface excess concentration is the ionic number concentration per unit area ($A$) of the interface and the chemical potential is given by

$$\bar{\mu}_i = \bar{\mu}_0 + RT \ln\left(\gamma_i \frac{c_i}{c_{i_0}}\right) \qquad 6.6.2$$

In conclusion, it must be noted that the experimental results from this section do not indicate a significant ion adsorption at a liquid-liquid interface. This may be also related to the insensitivity of this technique.

## 6.7 Partition of DNA in a standard ATPS of PEG and dextran

**Purpose of determining the partition coefficient**

It has been shown that the partition coefficient of DNA in an ATPS of dextran and methylcellulose is dependent on the sedimentation coefficient [193, 274] and moreover, a size dependence of the sedimentation coefficient on the molecular weight of DNA is reported [275, 276]. Different DNA species such as open circular and supercoiled plasmids, chromosomal DNA or RNA partition differently in ATPS of salt and low molecular weight PEG mainly due to a different packing [203, 274, 277-279]. Thus, it is interesting to study the partition of DNA in the ATPS composition of this thesis.

**Partition in respect to the DNA fragment length**

The partition of various DNA fragments stained with YOYO-1 is measured as the ratio of the fluorescence intensities of both phases in different ATPS buffered in 5 - 50 mM Tris/borate electrolyte. The DNA concentration is chosen to be ≈ 6 pg $\mu l^{-1}$. The DNA is subjected to the top phase and mixed with the ATPS to allow partitioning for 15 hours at 20°C in a volume 800 µl in a reaction tube. At this time DNA partition is expected to be completed in the used volume of a mixed solution. The two phases have been introduced in a two-lamellae configuration into a PDMS-glass chip and the fluorescence is measured under quiescent conditions. The average and standard deviation is calculated from three fluorescence intensity measurements.

At 5 mM ionic strength all DNA fragments partition entirely into the dextran phase (Fig. 27), which also shows that partition is completed after 15 h. The fluorescence in the PEG phase equals the background fluorescence of a single PEG phase without DNA. The fluorescence signal of the DNA containing polymer phase is about 120% of that obtained from the background. It is emphasised that small variations in the DNA concentration may change the estimated fluorescence ratio if DNA partitions entirely into one phase, and give slightly different values for the fluorescence ratios of the phases in 5 mM ionic strength due to an unfavourable signal to noise ratio. This applies to 653 bp and 2200 bp DNA.

All DNA fragments partition almost entirely into the PEG phase at 50 mM ionic strength, which is observed comparing the fluorescence intensity of the dextran phase with the background (fluorescence intensity without DNA-YOYO-1 addition). The plots of Fig. 27 also show that all DNA fragments partition equally between both phases at an ion concentration of 30 mM.

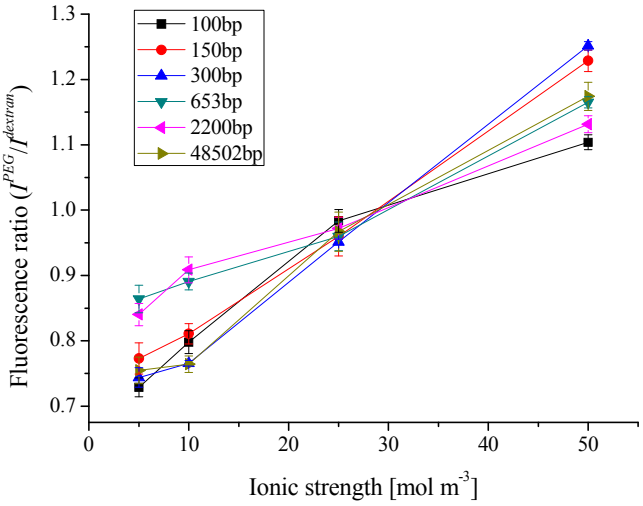


*Fig. 27: Partition of various DNA fragments. The fluorescence intensity ratio of PEG/dextran phase is measured in a microchip to illustrate the partition in respect to the ionic strength. All fragments partition evenly at about 30 mM ionic strength.*

In conclusion, from these experiments no significant size dependent partition is observed for DNA fragments between 100 - 48502 bp in this ATPS. But, the experimental design may limit the access to a possible small size-dependent partitioning. Previously, Lif et al. showed that the partition coefficient of DNA is dependent on the sedimentation coefficient in dextran-methylcellulose ATPSs [280]. The sedimentation coefficient is the ratio of the velocity of a particle to the applied centrifugal acceleration and dependent on the molecular weight and tertiary molecule structure [275]. The dissimilar behaviour in partition of such DNA species could be due to an altered charge density for differently packed molecules such as supercoiled and open circular plasmids. The charge density would alter the Born energy as a part of the Gibbs free energy of transfer.

# Chapter 7: Adsorption and desorption of DNA at a liquid-liquid interface

## 7.1 Summary

The chapter addresses the electrophoretic transport of DNA in a standard ATPS consisting of PEG and dextran to investigate the electrophoretic adsorption of these molecules at the liquid-liquid interface. The ATPS has been prepared in different electrolytes, and the experimental observations highlight several electrokinetic phenomena dominating in the adsorption process depending on the electrolyte used in the investigations. DNA of the Lambda phage (λ-DNA), which is stained with an intercalating dye, is mainly used to monitor the interfacial adsorption. Under a critical electric field strength applied perpendicular to the liquid-liquid interface, DNA remains trapped. Thus, this method contains a novelty in electrophoretic preconcentration of DNA at such an interface. An important outcome is that the adsorption of DNA is solely feasible if the molecules are transported from the dextran phase towards the PEG phase.

In sodium phosphate ATPSs of PEG and dextran, island formation is observed, where the DNA molecules merge to form concentrated islands along the liquid-liquid interface. In ATPSs prepared in Tris-buffers the island formation is strongly reduced and a homogenous adsorption is achieved, which allows continuous experiments to elucidate more details of the desorption process into the non-preferred PEG phase occurring at larger applied electric fields. Once more, the microfluidic setup of Chapter 5 is utilised.

## 7.2 Adsorption of DNA at the liquid-liquid interface of an ATPS prepared in sodium phosphate

**Adsorption using a 5 mM sodium phosphate pH 7.9 ATPS**

By following the experimental procedures described in Chapter 5, a PEG phase and dextran phase with equal width have been introduced into the proposed PDMS-glass microchip, while the dextran phase contains λ-DNA in concentrations of 6.6 pg $\mu l^{-1}$. The ATPS has been initially prepared in 5 mM sodium phosphate pH 7.9. An electric field is applied perpendicular to the liquid-liquid interface and the DNA adsorption is followed utilising the epifluorescence microscope setup described in Chapter 5.

Under quiescent conditions island formation accompanies the electrophoretic adsorption of λ-DNA at the liquid-liquid interface of an ATPS. In particular, the use of sodium phosphate electrolyte in a PEG-dextran ATPS results in merged λ-DNA molecules to form an island. The larger the merged island, the more it affects its surroundings by attracting more molecules, which adsorb at the interface.

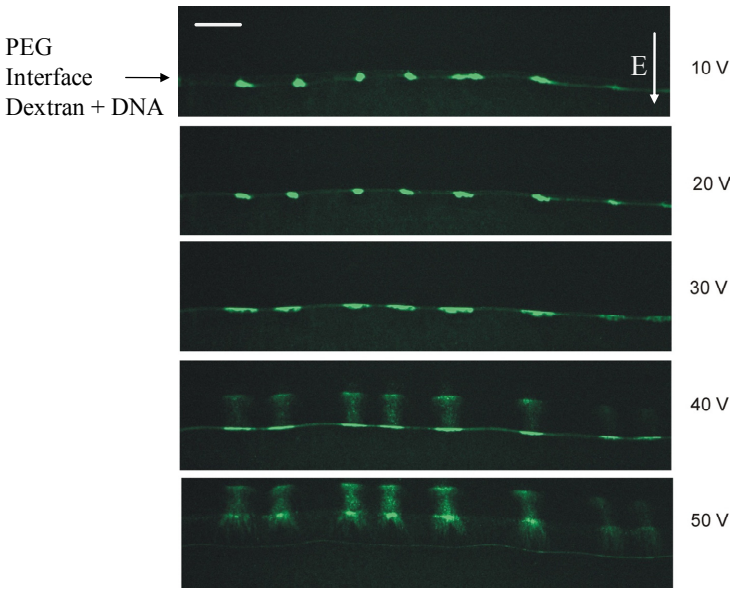


*Fig. 28: Adsorption of λ-DNA at a liquid-liquid interface results in an island formation with a longitudinal alignment (bar top-left: 200 μm). The potential has been gradually increased to change the shape of such islands (10-30 V) and to desorb them (40-50 V).*

The islands at the liquid-liquid interface condense more at lower applied potentials than at larger ones. Above a critical potential, desorption into the PEG phase occurs (Fig. 28). Desorption takes place from the centre of such an island. At even larger potentials the entire island desorbs from the interface (Fig. 28).

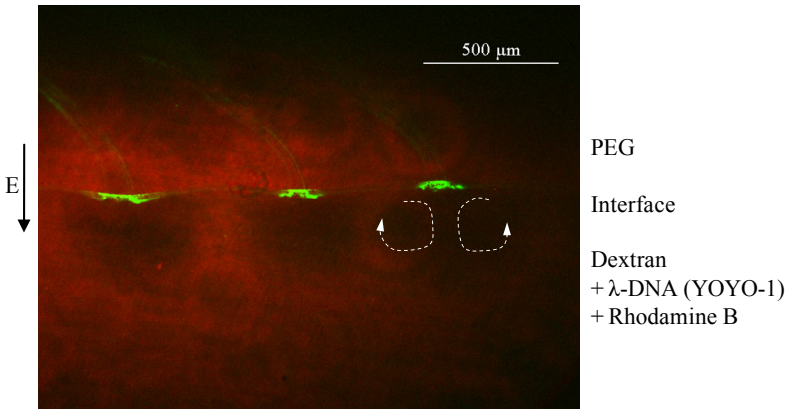


*Fig. 29: Convection zones below the DNA islands lead to a rhodamine B (red) depletion in the lower dextran phase. The rhodamine B is visualized with 543 nm excitation and overlaid to a DNA (YOYO-1) excited at 488 nm. Two arrows illustrate the convection flows underneath a DNA island within the dextran phase.*

In order to evaluate the nature of the island formation rhodamine B and YOYO-1 stained λ-DNA are simultaneously added to the dextran phase to track the convection flows appearing below the interfacial DNA islands (Fig. 29). The convection flows have been identified to appear within the dextran phase and to cause depletion zones of rhodamine B. This uncharged dye diffuses into the PEG phase and is depleted due to convection underneath a DNA island. Moreover, some λ-DNA molecules migrate backwards into the dextran phase and oppose the electrophoretic transport due to the convections.

Although dsDNA does not diffuse into the PEG phase at 5 mM ionic strength, ssDNA diffuses through the liquid-liquid interface with almost no resistance (Fig. 30). SsDNA does also not accumulate at the interface by applying an electric field and transport it from the dextran towards the PEG phase. With the standard PEG/dextran system in sodium phosphate electrolyte solely dsDNA adsorbs electrophoretically and forms islands at the liquid-liquid interface.

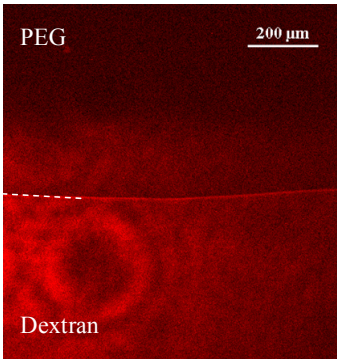


*Fig. 30: Diffusion of 22 bases ssDNA across the boundary. Initially the Cy3 labelled ssDNA is dissolved within the dextran phase to 1 pmol $\mu l^{-1}$.*

**Measurements of DNA island formation**

The following data illustrate the number of islands forming within an experiment at a constant applied potential (30 V). λ-DNA is initially dissolved within the dextran phase to 6.6 pg $\mu l^{-1}$ and the dextran phase is sandwiched between two PEG phases with a flow injection of 5-1-5 µl $min^{-1}$ (PEG-dextran-PEG). The island formation prevails in the adsorption process in a standard ATPS prepared in 5 mM sodium phosphate pH 7.9. The number of islands have been counted using NIS Elements (Nikon) and certain set parameters such as minimum island size being 2 - 3 merged λ-DNA molecules.

Fig. 31 illustrates the number of islands on a length scale of 821 µm corresponding to the view field in x-direction. The number of islands at the interface increases rapidly. After more than 50 s the island condensation exceeds the formation of new islands although DNA molecules continuously adsorb.

In video sequences it has been qualitatively observed that the strength of the convection flow increases in respect to the time. Once the islands have formed, the convection amplitude remains on a similar level.

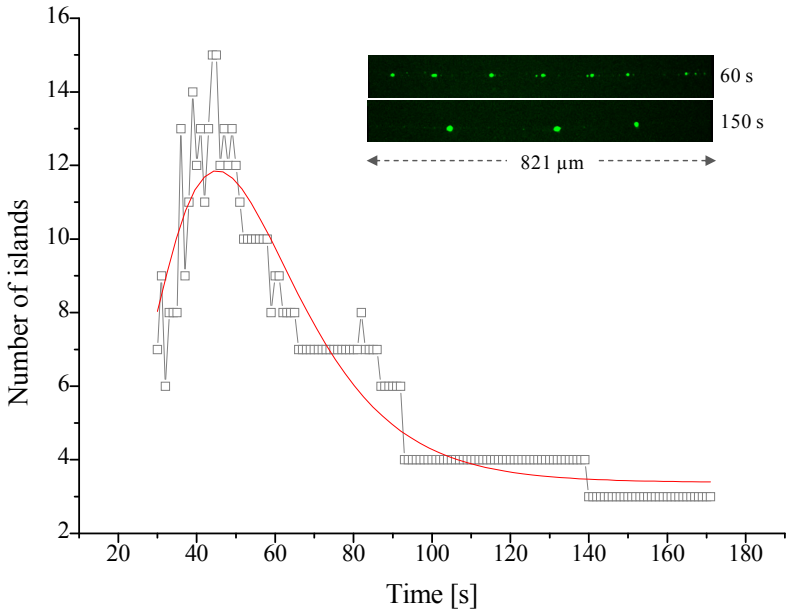


*Fig. 31: The number of islands at an 821 µm long interface increases rapidly within the first 40 s. Later, the islands merge and this number decreases. ($\varphi^{ext}$=30 V; $c_{\lambda\text{-}DNA}$=6.6 pg µl$^{-1}$). At this time the merging of islands and λ-DNA with the islands is faster than the formation of new ones.*

**Discussion of the phenomena provoking island formation**

The driving force of the island formation cannot be solved from the experimental data given above. Nevertheless, some important phenomena are herein discussed to give an outlook and put the data into a context that helps to identify the underlying principles in upcoming theoretical models.

Firstly, a protrusion of the interface in the region between two islands accompanies the island formation (Fig. 29). In view of the surface tension, which is dependent on the curvature of an interface [145, 182, 281], a lower surface tension in curved regions is expected, which means regarding the Marangoni effect, liquid moves away from the islands. This opposes the observed tangential migration of DNA along the interface that is directed towards the DNA island (Fig. 29). Differences in local polyion concentrations along the interface may also contribute to a Marangoni effect.

In the literature the presence of a dipole potential at the liquid-liquid interface of ATPSs has appeared [194, 282]. Such a dipole potential is also observed from nanoparticles

adsorbed at liquid-liquid interfaces [283, 284]. Here, the dipole potential arises from the particle itself. However, the experimental results can just be a basic scaffold and help to develop a theory covering all complex interfacial phenomena.

## 7.3 Adsorption of DNA in ATPSs prepared in Tris/borate electrolyte

### Adsorption using a 5 mM Tris/borate pH 8.0 ATPS of PEG and dextran

The previous section has identified the DNA island formation at a liquid-liquid interface of an ATPS prepared in sodium phosphate. The observed uneven adsorption pattern has some disadvantages for studying fundamental issues at the boundary and also for possible applications where a homogenous distribution is favoured. Eventually, an even adsorption is achieved employing a Tris/borate electrolyte. The choice of ions has shown a major impact on the interfacial island formation. However, island formation is not totally absent even in Tris/borate electrolyte ATPSs, but the convections are greatly reduced to offer a time frame sufficient to investigate the boundary in more detail.

Fig. 32 represents the even adsorption of λ-DNA at the liquid-liquid interface while an electric field is applied perpendicular to the interface. The image represents a typical DNA concentration used in the majority of such experiments. Single molecules and clusters of 2 or 3 are mainly observed at the interface.

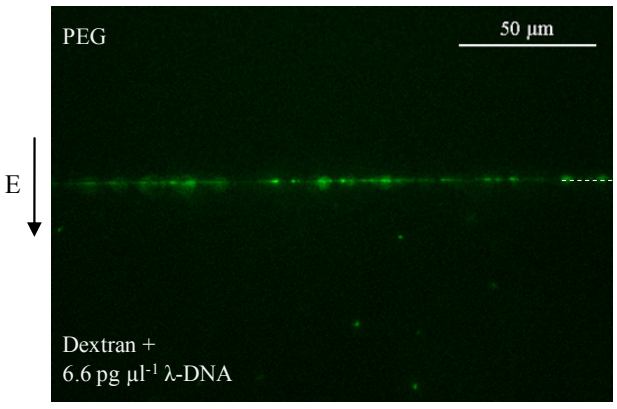


*Fig. 32: Adsorption of λ-DNA at a phase boundary of an ATPS of PEG and dextran prepared in 5 mM Tris/borate pH 8.0 results in a homogenous distribution. DNA is transported from the dextran towards the PEG phase.*

Adsorption of DNA at the liquid-liquid interface is not observed, if the molecules are initially subjected to the PEG phase and transported towards the dextran phase (Fig. 33A). This accounts for an ionic strength of 5 mM and 50 mM in the ATPS. Solely a slight mass transfer resistance is observed in 5 mM ATPSs that traps some molecules for a few seconds and sometimes stretches them (Fig. 33B).

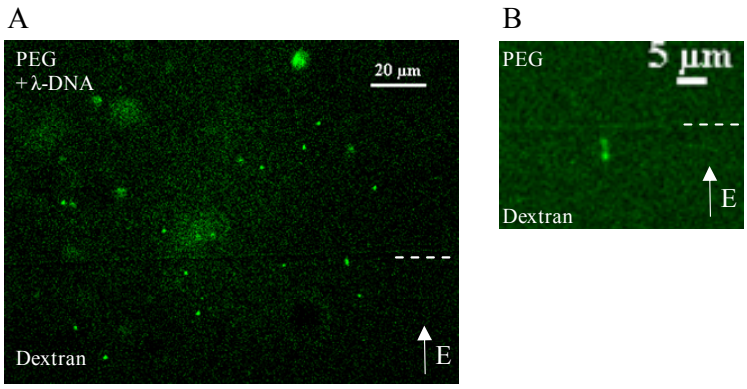


*Fig. 33: Electrophoretic transport of λ-DNA from the PEG towards the dextran phase. No accumulation is observed, neither in ATPSs of 5 mM nor 50 mM ionic strength (A). A few molecules remain at the interface in 5 mM ATPSs for some seconds. The trapping results in stretching, but no permanent DNA adsorption is observed (B).* $E^{ext} \approx 100\ V\ m^{-1}$.

In conclusion, it is obvious that the preference of DNA to a certain polymer phase does not initiate adsorption. Chapter 6.7 elucidated a strong preference of DNA to the PEG phase in 50 mM ionic strength ATPSs, but no electrophoretic adsorption is achieved while transported from the PEG towards the dextran phase (Fig. 33A). Hence, solely the Gibbs free energy of transfer as presented in Chapter 4.2 cannot be accounted for an adsorption of DNA at the liquid-liquid interface and its partition. The electrokinetic phenomena may play a major role. In the following the experiments focus on an electrophoretic DNA adsorption when DNA is transported from the dextran phase towards the PEG phase to reveal more details. A discussion about the consequences of the observations is revisited in Chapter 10.

## 7.4 Desorption triggered by an external potential

**Desorption of λ-DNA in a Tris/borate ATPS of PEG and dextran**

Once λ-DNA is adsorbed at the liquid-liquid interface, it desorbs if the applied potential is increased to a critical value. Fig. 34 represents a typical desorption process of λ-DNA previously being dissolved in a dextran phase and electrophoretically adsorbed at the interface. Desorption is triggered by increasing the applied potential and occurs in Tris/borate electrolyte ATPS of PEG and dextran evenly along the entire interface.

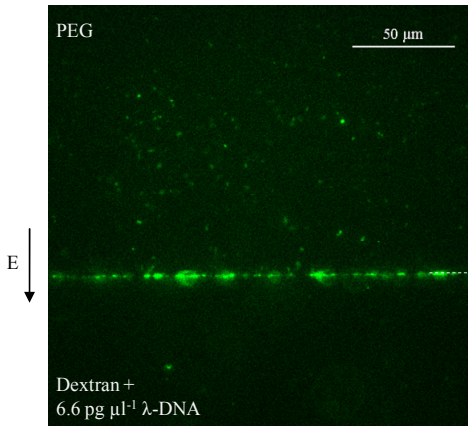


*Fig. 34: The desorption process of λ-DNA into the PEG phase by increasing the applied potential is exemplified.*

**Desorption of 150 bp DNA in a Tris/borate ATPS of PEG and dextran**

λ-DNA is a molecule with some internal degrees of freedom and a large configurational entropy. The cohesive ends of 12 bp enable the molecule to form circles, if the ends anneal. The molecule structure differs from globular to coiled conformations being all present in the polymer solutions. In view of these inhomogeneities a 150 bp DNA fragment has been chosen to study the desorption process at increased electric fields in more detail. The 150 bp DNA fragment has a stiffed rod-like shape with the dimension

of about one persistence length (50 nm) and is expected to be similar throughout all molecules in the system.

Thus, 150 bp DNA is introduced into the dextran phase at final concentrations of 8 pg $\mu l^{-1}$ stained with YOYO-1 (dye:bp, 1:4). The dextran phase is sandwiched between two PEG phases with flow rates of 5-2-5 µl $min^{-1}$ for PEG-dextran-PEG. Once the ATPS input flow has stopped and the interface shows stability in quiescent conditions, an electric field of 112 V $m^{-1}$ is applied to accumulate the DNA at the boundary. At 120 s the electric field is increased to induce desorption (Fig. 35).

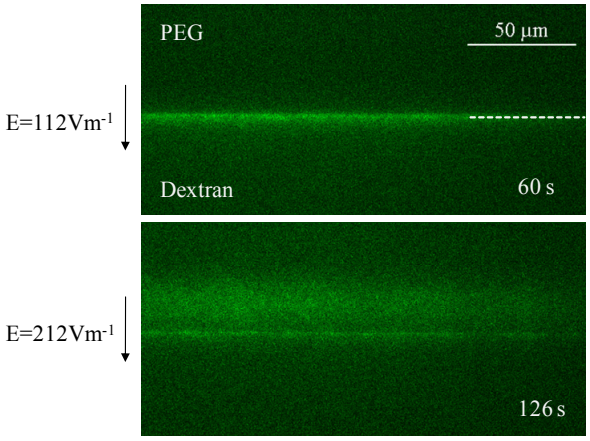


*Fig. 35: Appearance of the interface at 60 s showing the adsorption process, and at 126 s illustrating desorption. The electric field is increased at 120 s to trigger desorption.*

In order to quantify the desorption process, the interfacial fluorescence is analysed. A field of interest is defined just to cover the liquid-liquid interface along the entire view field (Fig. 35). The fluorescence intensity is measured every second exciting the chamber only 100 ms per frame with 488 nm (5 mW) to minimise photo bleaching. The image is corrected to account for the background and normalised. The interfacial fluorescence is plotted in Fig. 36 for different electric fields triggering the desorption event at 120 s, which corresponds to 0 s in the graphs.

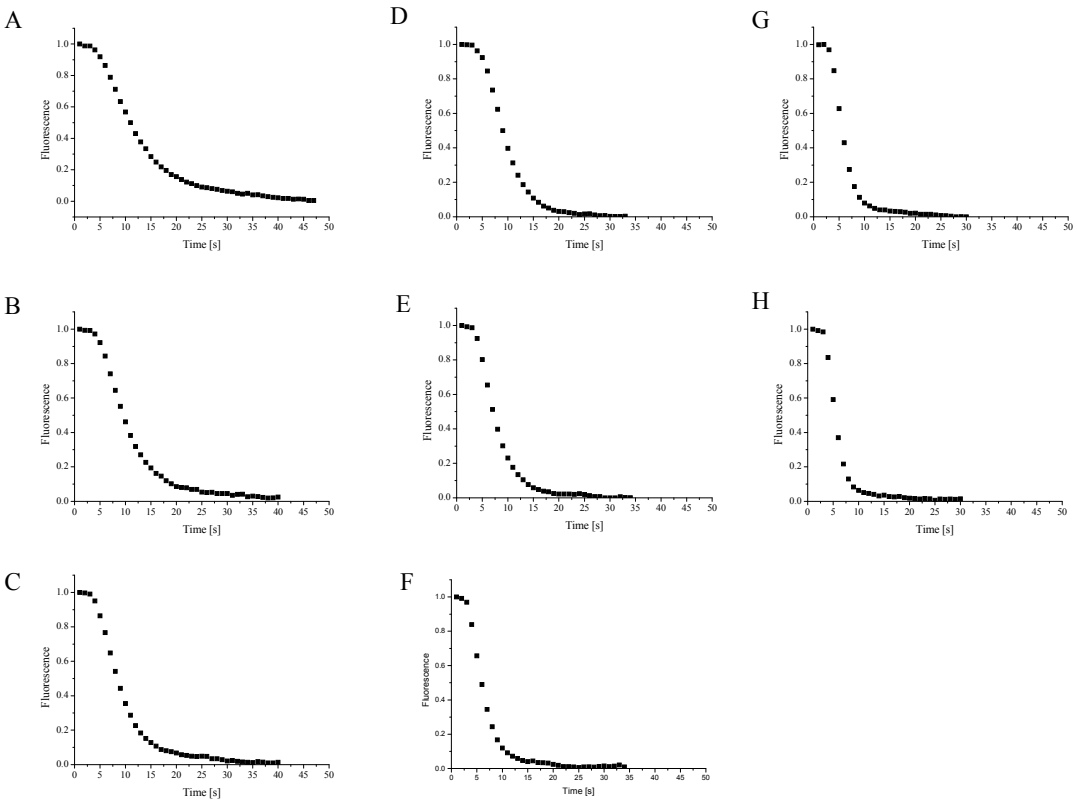


*Fig. 36: The normalised fluorescence intensity ($I/I_0$ while $I_0$ at 0 s) is measured at the interface (■). After preconcentration for 120 s at 112 V $m^{-1}$ the external electric field has been increased to 162 V $m^{-1}$ (A), 175 V $m^{-1}$ (B), 181 V $m^{-1}$ (C), 187 V $m^{-1}$ (D), 199 V $m^{-1}$ (E) or 212 V $m^{-1}$ (F), 224 V $m^{-1}$ (G) and 237 V $m^{-1}$ (H) to induce DNA desorption at t=0.*

Revising the plots in Fig. 36, the exponential decay appears after approximately 5 s. The delayed desorption is not related to the ramp speed of the power supply, which takes less than 1 s for the potential shift. It is assumed that the external applied electric field requires some time to change the involved parameters.

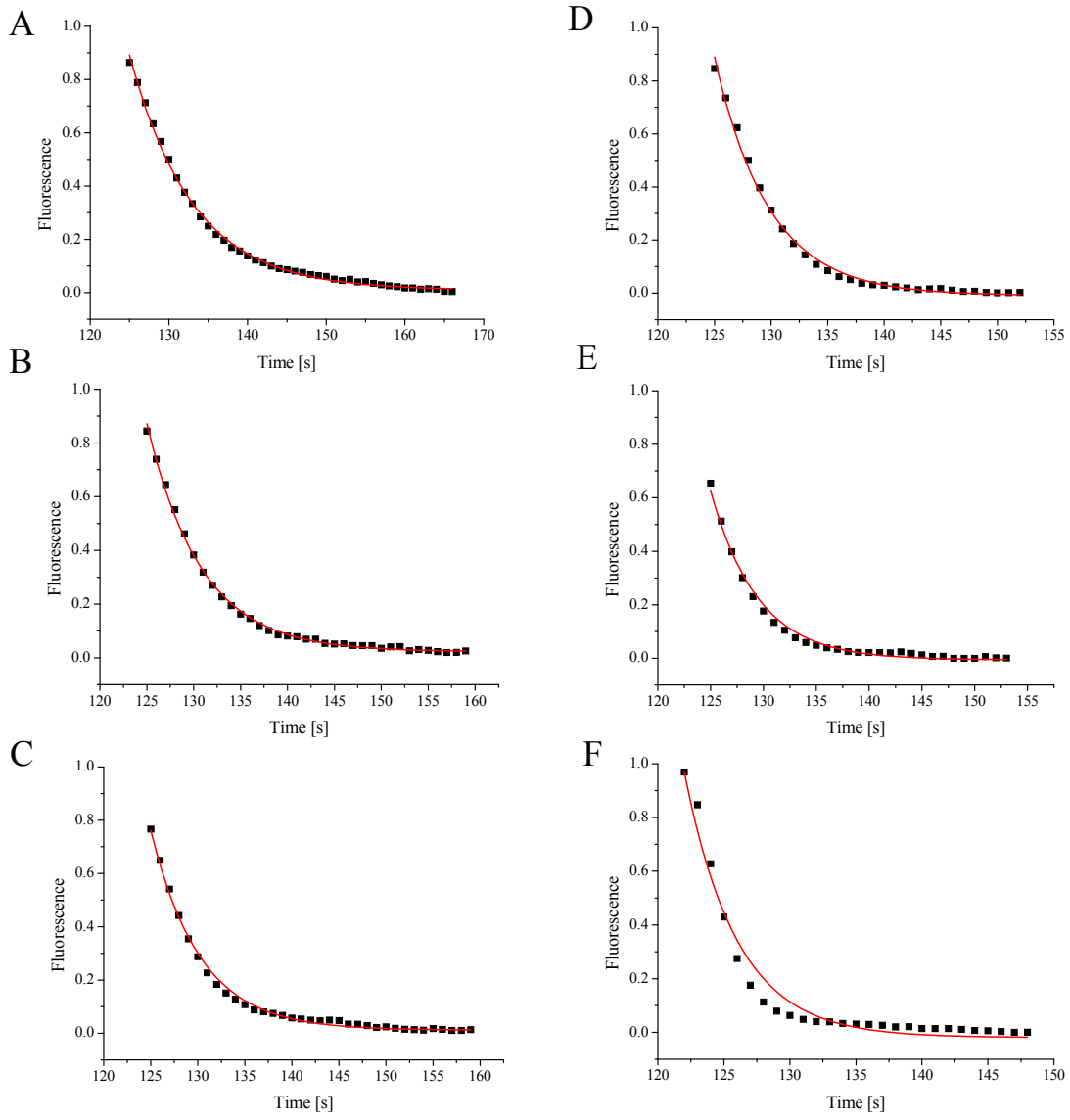


*Fig. 37: The normalised fluorescence intensities at the interface during the desorption process initiated at 120 s using different electric fields, 162 (A), 175 (B), 181 (C), 187 (D), 199 (E), 224 (F) V m$^{-1}$ show an exponential decay. The fluorescence has been fitted to an exponential function (solid lines).*

In order to evaluate a first principle describing the desorption process, one can consult Kramers' reaction rate theory [285]. The decay of the interfacial fluorescence as seen in Fig. 36 is described by a relationship of the type

$$f(t) = A\exp\left(-\frac{t}{\tau_b}\right) \qquad 7.4.1$$

where $A$ is exclusively here the initial fluorescence intensity, $1/\tau_b$ the escape rate and $t$ the progressed time. The function corresponds well to the measured interfacial fluorescence as exemplified in Fig. 37.

The data of Fig. 37 indicate that the exponential curves fit the experimental results very well for electric fields below 200 V $m^{-1}$, while the concurrence deteriorates for field strengths above that value.

The exponential decay of the fluorescence, which equals the number of adsorbed molecules, is in agreement with what would be obtained for the thermally induced escape from a metastable state. If a DNA molecule has to overcome a free-energy barrier $\Delta F$ to escape from the interface into the PEG phase, Kramers' reaction rate theory predicts that

$$\tau_b \propto \exp\left(\frac{\Delta F}{k_B T}\right) \qquad 7.4.2$$

where $k_B T$ is the thermal energy. In Fig. 38 the dependence of $\tau_b$ on the applied electric field is shown. Apparently $\tau_b$ decreases exponentially with $E^{ext}$.

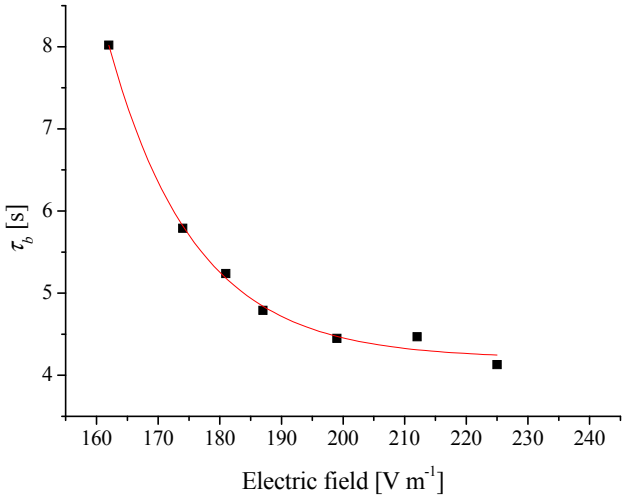


*Fig. 38: Escape time of a 150 bp DNA fragment as a function of electric field strength.*

In subsequent chapters more results to the adsorption and desorption will support a discussion about the nature of this interfacial processes. Concluding for now, the

applied electric field has a comparatively large influence on the interfacial adsorption process, which was not expected. This is illustrated, if one relates the Galvani potential known for such ATPSs being between 0.3 - 4 mV [192, 194, 195, 197, 286] to a theoretical Debye length, which results in electrostatic fields of about $10^5$ V $m^{-1}$ at the interface. Therefore the influence of external fields of the order of 100 V $m^{-1}$ is surprising and shows the inconsistence between the expectations from a simple view.

**Interfacial DNA repulsion at $E^{ext} = 0$**

In the following, the interfacial repulsion of λ-DNA from the interface at suddenly switched off potentials is investigated. A standard ATPS prepared in 5 mM Tris/borate is chosen. Originally, λ-DNA is dissolved to 0.66 pg $\mu l^{-1}$ within the dextran phase, which is introduced with the same width between two PEG phases for the experiments of this section. Such low DNA concentrations provide a few molecules per view field and permit to follow the adsorption process of single molecules. The electric field is 300 V $m^{-1}$ and applied for 100 s to track the velocity of single molecules.

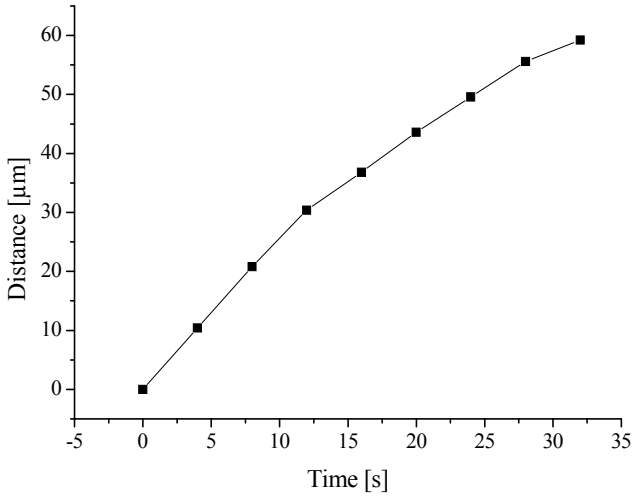


*Fig. 39: A measurement of a single λ-DNA molecule that repels from the interface. At a time of 0 s, the applied potential is switched off and the distance of the molecule to the interface is measured in respect to the time. The DNA concentration is 0.66 pg $\mu l^{-1}$.*

λ-DNA DNA moves backwards into the dextran phase once the applied potential is switched off by connecting the two electrodes to ground. The repelling nature of the interface onto a λ-DNA molecule appears even several micrometres apart from the boundary. Other interfacial forces such as surface tension do not compensate the repellence to keep a molecule trapped at the interface. Fig. 39 shows the distance of a molecule from the interface in respect to the time. The repellence is faster than it would be expected from diffusion. It is known that certain parameterised ATPSs enable permanent adsorption of DNA at the liquid-liquid interface even if the external potential is switched off [203, 210, 277]. In the ATPS of this study, DNA experiences a lower free energy in the bulk of a dextran phase if no electric fields are applied. A reversed current is also expected to contribute to the repellence. This has been measured in Chapter 6.4. The time constants from the reversed current coincide with the time value in Fig. 39.

## 7.5 Time-induced desorption of λ-DNA at the liquid-liquid interface

**Self-destabilisation of the adsorption process at constant applied potentials**

It has been previously worked out that desorption of DNA into the PEG phase occurs at a critical potential applied perpendicular to the interface. Once the electric field in the compartment is increased to a certain value, DNA desorbs from the boundary into the PEG phase. It has been shown that this critical value of the electric field decreases with time. If the experimental time is long enough, the critical electric field attains the value, which is used to preconcentrate DNA at the interface. Desorption of DNA is consequently observed. In the following it is investigated, which factors account for the destabilisation of the interfacial adsorption process and trigger desorption at a certain time.

The time dependence of this destabilisation is herein identified for a standard ATPS prepared in 5, 10 and 20 mM Tris/borate or 5, 7.5, 10 and 15 mM Tris/borate. The flow

introduction of the three lamellae configuration is 10-10-10 µl $min^{-1}$ (PEG-dextran-PEG) and ensures that molecules adsorb constantly over the entire experiment. The flow configuration provides three lamellae of equal width.

The time of desorption has been defined as the time when a maximum fluorescence intensity is measured at the interface (Fig. 40). Although still molecules migrate from the dextran phase towards the interface, desorption is the dominating process and the measured interfacial fluorescence decreases. The time-induced desorption is measured for all prepared ATPSs.

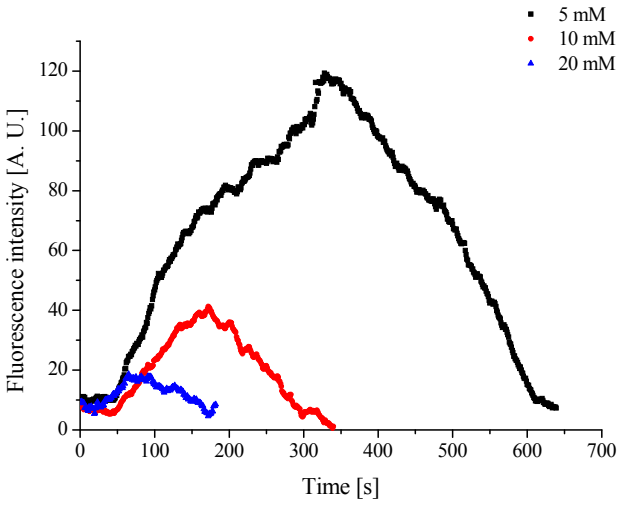


*Fig. 40: Fluorescence intensities of the interface showing adsorption of λ-DNA applying a constant electric field of 122 V $m^{-1}$. The maximum represents the time of desorption. Different ion concentrations in an ATPS between 5-20 mM reveal a dependence on the ionic strength.*

A linear relation is observed, considering the time of desorption from experiments obtained such as seen in Fig. 40 against the Debye length calculated for different ionic strengths at $T$ = 20°C and $\varepsilon_r$ = 80. For any electric field ($E^{ext}$) chosen between 122 and 374 V $m^{-1}$ the linear plot subtends the x-axis at a Debye length of ≈ 1.7 nm (Fig. 41).

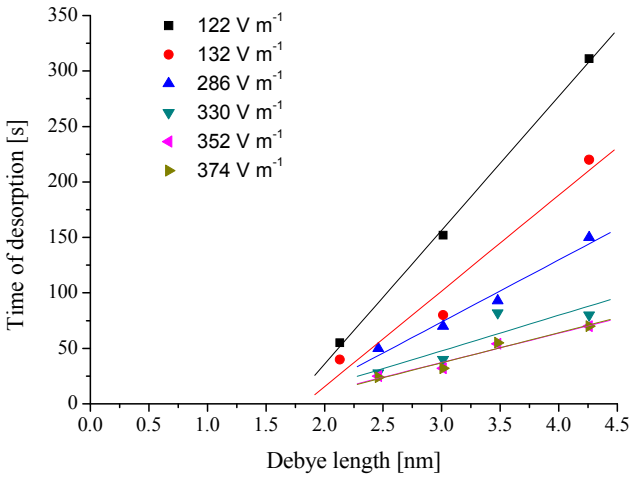


*Fig. 41: Increasing ionic strength causes decreasing Debye length and therefore reduces the time at which the adsorption is stable. The destabilisation is denoted here as the time when desorption starts. An electric field between 122-374 V $m^{-1}$ is applied to adsorb and desorb λ-DNA. The adsorption limit is achieved for $\lambda_D$ < 1.7 nm – at the hypothetical time of desorption, t = 0.*

The Debye length of 1.7 nm corresponds to an ion concentration of 32 mmol $L^{-1}$. In a standard ATPS using a Tris/borate electrolyte of at least this ion concentration no interfacial adsorption is achieved. It has been confirmed by preparing a standard ATPS in 50 mM Tris/borate pH 8.0 that λ-DNA does not adsorb at such a liquid-liquid interface, if electrophoretically transferred from the dextran phase towards the PEG phase or conversely. It is noted that λ-DNA partitions entirely into the PEG phase at such ionic strength (Chapter 6.7).

Electric fields above $10^5$ V $m^{-1}$ reduce significantly the dielectric constant and give a different Debye length than calculated as for Fig. 41. As the electric field and hence, the permittivity at the interface is not known, it is suggested to refer the Debye length of 1.7 nm to a concentration of electrolytes of 32 mmol $L^{-1}$. At this concentration the hypothetical time of desorption is zero, meaning no DNA adsorption is feasible. The time of desorption seems to be linear dependent on the Debye length. Although the indication for a time dependent concentration of ions at the interface is given by these experiments, interfacial tension measurements of Chapter 6.6 do not reveal such a physical process with a required significance and this issue remains unclear.

**Variations in the local electric field over time**

The analysis of the velocity of λ-DNA in respect to time in the microchip compartment, which is filled with polymer phases in a three-lamellae configuration, requires attention because time dependent variations in the velocity have been observed. The alterations in the velocity are directly related to changes in the local electric field strength by consulting the Smoluchowski equation. Therefore, 8.4 pg $\mu l^{-1}$ λ-DNA are added to a dextran phase of a standard ATPS prepared in 5 mM Tris/borate pH 8.0 in a three-lamellae configuration with a flow introduction of 5-2-5 µl $min^{-1}$ (PEG-dextran-PEG).

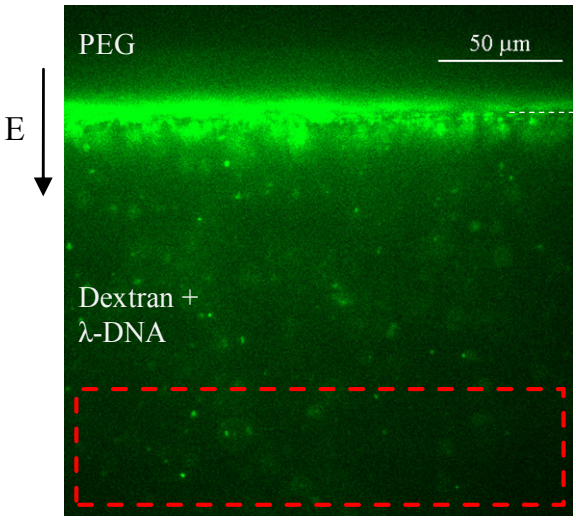


*Fig. 42: Exemplified image of an experiment measuring the velocity of λ-DNA in the lower quarter (red rectangle). For better visualisation λ-DNA of 16.8 pg $\mu l^{-1}$ is present in the dextran phase.*

The view field of the chip section is chosen so that the interface appears in the upper quarter. Below, the dextran phase is present containing λ-DNA at the above mentioned concentration. The lower quarter of the view field has been used to measure the velocity of single λ-DNA molecules (Fig. 42).

The simultaneous observation of interface and dextran phase enables to correlate the time of desorption from the interface with the velocity of λ-DNA in the lower quarter of the image being at least 120 µm apart from the interface. The velocity of various λ-DNA molecules is measured at different time points and illustrated in Fig. 43 by calculating the electric field strength using the Smoluchowski equation. Three different

potentials have been applied, 14 V ($E^{ext}$ = 219 V m$^{-1}$), 15 V ($E^{ext}$ = 234 V m$^{-1}$) and 16 V ($E^{ext}$ = 250 V m$^{-1}$) giving a specific electric field strength measured according to Chapter 6.2.

The data in Fig. 43 shows for all applied potentials that the electric field in the dextran phase in proximity to the interface suddenly increases. It is emphasised that the increase of the electric field strength, which corresponds to the increase of the velocity of λ-DNA, occurs at the time of desorption for each applied potential (Tab. 5). Initially, the electric field decays, which is more pronounced for lower applied potentials.

Although not shown in these experiments, it has been observed that the system gets back to equilibrium after 400-500 s and the electric field decreases again to its initial value.

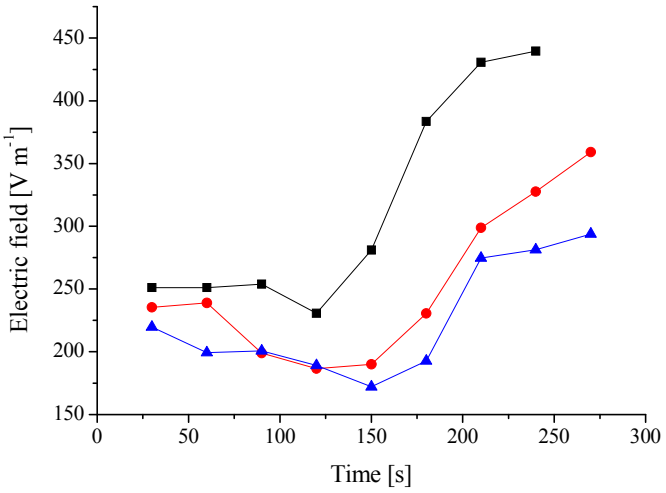


*Fig. 43: Measured velocities of λ-DNA reveal the electric field via the relationship $u=\mu_e / E^{ext}$ as a function of time for different applied potentials: 14 V (▲), 15 V (●) and 16 V (■). The electric field at 30 s is set to $E^{ext}$ measured according to Chapter 6.2.*

*Tab. 5: Time of desorption of λ-DNA from the boundary using different applied potentials. The data corresponds to the experiment in Fig. 43.*

| Applied potential [V] | Time of desorption [s] |
|---|---|
| 14 | 190 |
| 15 | 180 |
| 16 | 165 |

Moreover, the increase in the electric field is also observed in the PEG phase (Fig. 44). In such experiments λ-DNA is additionally added into the PEG phase and the velocity is measured in the middle of a PEG phase to have sufficient molecules present over time. In such experiments the interface cannot be observed simultaneously as the view field is chosen ≈ 1 - 2 mm away from the interface. Here the electrophoretic motion of DNA yields towards the anode and the molecules migrate away from the liquid-liquid interface. However, the results clarify the appearance of increased electric fields in both phases over time.

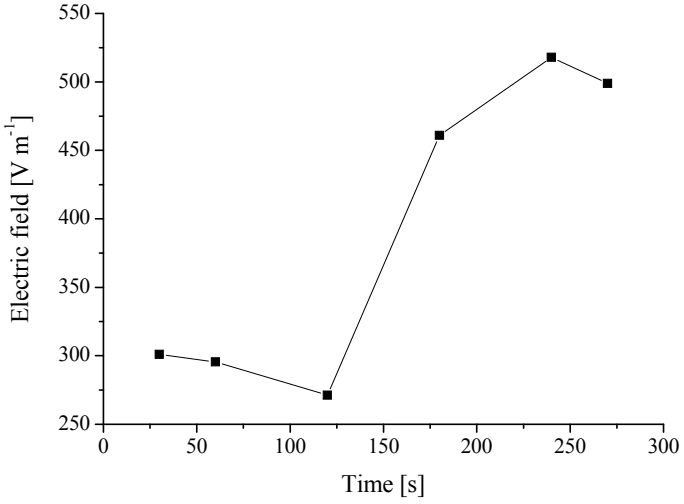


*Fig. 44: The electric field is calculated from the measured velocity of λ-DNA in the PEG phase at a constant applied potential (20 V corresponds to 301 V $m^{-1}$). λ-DNA has been additionally dissolved in the PEG phase.*

In the following investigations concerning the relevance of the DNA concentration in the adsorption process have been motivated. Fig. 45 indicates a correlation of DNA concentration and the stability of the adsorption process. Smaller DNA concentrations result in a faster increase in the electric field (Fig. 45) and a faster instability of the adsorption process, previously shown in the time of desorption. DNA initially used in concentrations to 4.2 pg $\mu l^{-1}$ show a faster destabilisation of the adsorption than larger DNA concentrations (Fig. 45). This has been reproduced for all applied potentials between 14-16 V.

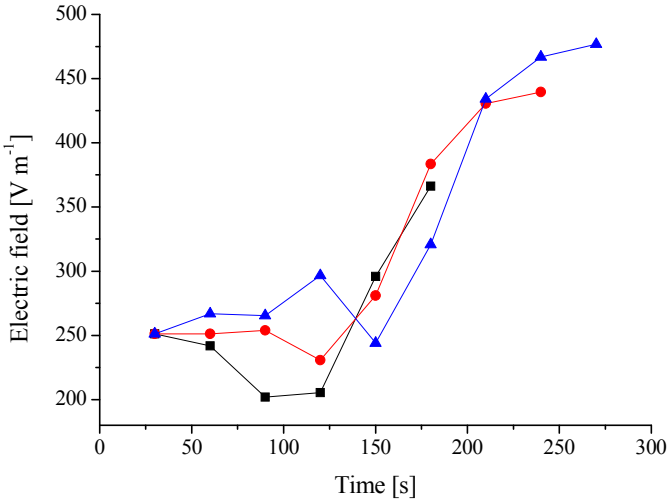


*Fig. 45: Electric field strength at constant 16 V ($E^{ext}$=250 V $m^{-1}$) using different concentration of λ-DNA (4.2 (■), 8.4 (●) and 16.8 (▲) pg $\mu l^{-1}$).*

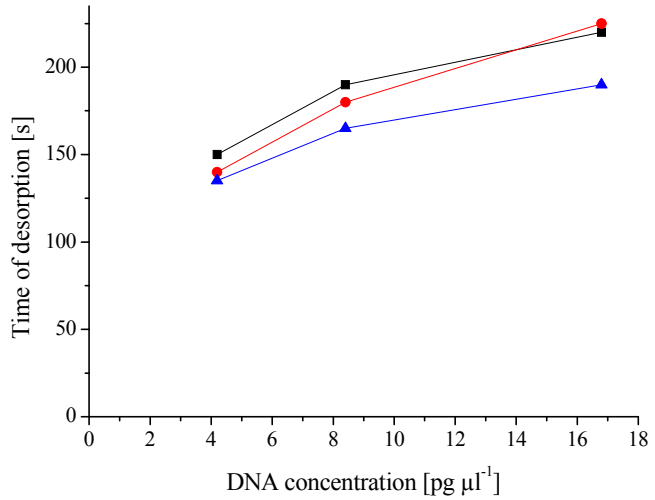


*Fig. 46: The time of desorption for different applied electric fields and λ-DNA concentrations within the dextran phase ($E^{ext}$=220 (■), 235 (●) and 251 (▲) V $m^{-1}$).*

Fig. 46 illustrates the measured time-induced desorption of λ-DNA for the different applied electric fields. It is evident that the DNA concentration changes the total interfacial energy well or barrier. More DNA adsorbed at the interface stabilises the entire adsorption process.

## 7.6 The dextran lamellae width contributes to the escape rate

**The escape time is dependent on the dextran lamellae width**

Remarkably, the stability of the adsorption process concerning the magnitude of the applied potential/electric field is observed to be dependent on the width of the lamellae of each phase introduced into the microchip.

A dextran phase is sandwiched between two PEG lamellae while the flow rate of the dextran phase is varied to adjust the width of the phase. The flow is stopped, as in all experiments above, and a potential of 10 V ($E^{ext}$ = 150 V m$^{-1}$) is applied for 100 s to accumulate a YOYO-1 stained 100 bp DNA fragment ($c$ = 8 pg µl$^{-1}$) at the liquid-liquid interface. Subsequent to the accumulation, the potential is increased to 30 V ($E^{ext}$ = 450 V m$^{-1}$) and the potential induced desorption process is initiated.

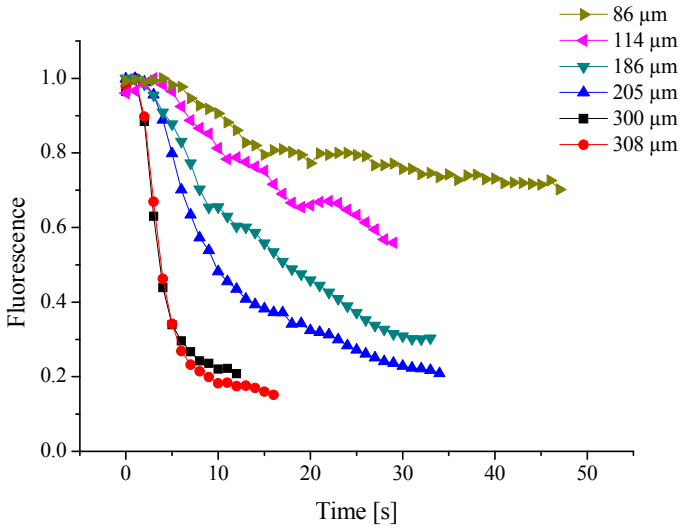


*Fig. 47: Potential induced desorption of a 100 bp DNA fragment while the width of the dextran lamellae surrounded by two PEG phases is varied between 86 - 308 µm. Smaller widths of the dextran phase increase the stability of DNA adsorption.*

The potential triggering desorption is shown for different width of a dextran phase by the interfacial fluorescence (Fig. 47) in respect to time. The time at $t$ = 0 corresponds to the potential increase after a preconcentration. The 100 bp DNA fragment desorbs

rapidly at a dextran lamellae width of 300 µm (PEG entirely 7700 µm) within 10 s, whereas using narrow dextran phases (86 µm) the 100 bp fragment desorbs more slowly. The exponential decay of Fig. 47 reveals the escape time $\tau_w$ (Fig. 48) that is a function of the dextran lamella width. The exponential fit of Fig. 48 follows the equation with width $x$ in µm and confidence $R^2 = 0.997$

$$\tau_w(x) = 39.34 \exp\left(-\frac{x}{168.14}\right) - 4.69 \qquad 8.6.1$$

The function crosses the abscissa at 360 µm. Further, a dextran lamella width larger than 600 µm does not have a significant effect anymore.

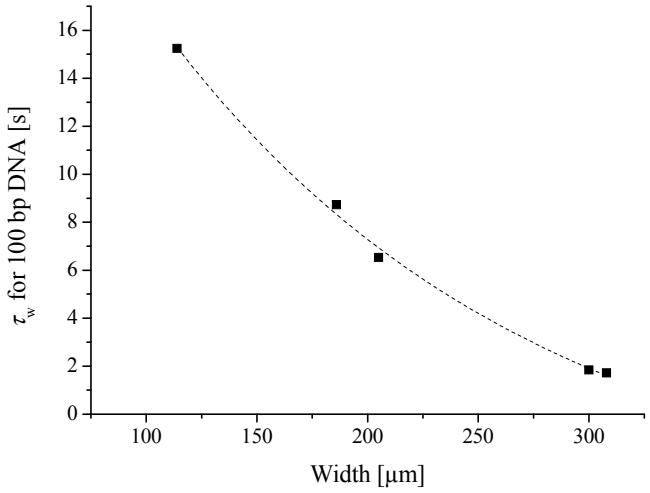


*Fig. 48: Escape time $\tau_w$ for different lamellae width of a dextran phase sandwiched between two PEG phases in the compartment. A 100 bp DNA fragment is used.*

**The escape time ($\tau_b$) for different lamellae width at different potentials**

In order to reproduce the dependence of the dextran lamellae width on the escape time and compare the data with the interfacial desorption measurements of Chapter 7.4 where a 150 bp DNA fragment desorbs by increasing the electric field, it has been motivated to measure the escape time ($\tau_b$) for a 150 bp fragment for a narrow dextran lamellae sandwiched between two PEG phases in the same manner. Again the DNA

fragment is accumulated for 120 s at the boundary and the experiments have been performed following the same procedure.

Fig. 49 illustrates the differences in the escape time when the width of the dextran lamellae is varied. The data confirms the dependence of the interfacial energy well or barrier on the lamella width.

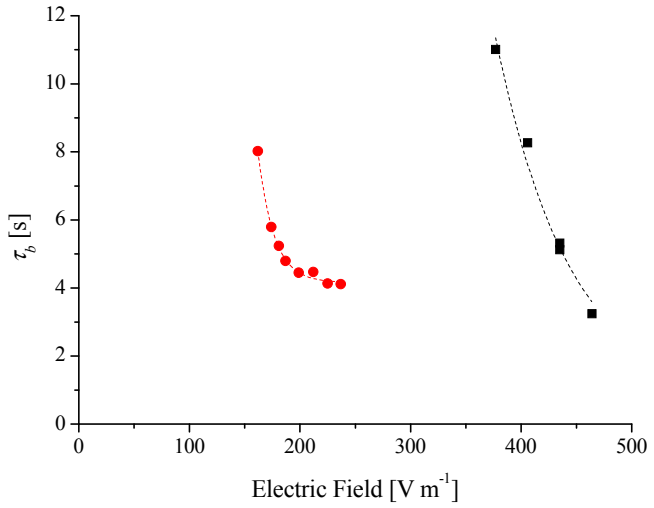


*Fig. 49: The escape time in respect to the expected electric field from measurements described in Chapter 7.4 using a dextran lamellae of 300 µm width (■) and about 1000 µm width (●) for a 150 bp DNA fragment. The dashed lines are the corresponding exponential fits. The real electric field close to the interface can be different if ions are accumulated within a dextran lamella.*

# Chapter 8: Size separation of DNA across a liquid-liquid interface of an ATPS

## 8.1 Summary

Previous chapters have elucidated that increased electric fields induce desorption of DNA, which is electrophoretically adsorbed at the interface. It has been motivated to reveal a DNA size dependent desorption process. Using different sized DNA fragments labelled with different dyes, it is evidently shown that the interfacial energy contributions to the potential energy barrier are size dependent in the system and a separation of various DNA fragments is feasible. Noteworthy, smaller DNA fragments desorb at low applied potentials while larger fragments desorb at higher potentials.

## 8.2 Simultaneous separation of two DNA fragments

### Simultaneous separation of 75 and 300 bp by a gradually increasing potential technique

Using a background electrolyte of 5 mM Tris/borate pH 8.0 in a standard ATPS consisting of PEG and dextran, separation of different sized DNA fragments of 75 bp and 300 bp DNA across a liquid-liquid interface is achieved. The liquid-liquid interface is generated by two flows, a PEG phase and a dextran phase containing the sample. Both phases occupy half of the compartment width (2 × 4 mm). By utilising PCR techniques as described in Chapter 5 the 75 bp and 300 bp DNA fragments are labelled with fluorescein or Cy3, respectively. Both dyes can be distinguished with standard filter sets and two laser excitation. This allows a specific observation of one DNA fragment in an experiment where two DNA fragments are present.

Both DNA fragments are simultaneously adsorbed at the liquid-liquid interface using a low applied potential of 10 V ($E^{ext} \approx 80$ V m$^{-1}$). The adsorption process proceeds for 240 s. Subsequently, the electric field is gradually increased by 16 V m$^{-1}$ each 20 s. The fluorescein labelled 75 bp DNA fragment desorbs at 270 s from the boundary ($E^{ext} = 128$). The 300 bp DNA fragment, labelled with Cy3 fluorophore, desorbs at 350 s when an electric field of 176 V m$^{-1}$ resides in the compartment (Fig. 50).

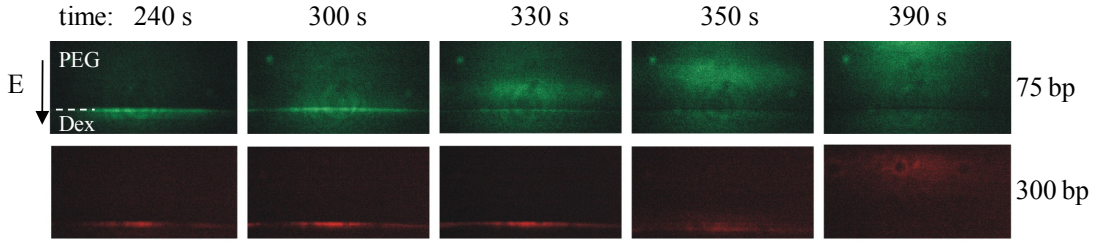


*Fig. 50: Size separation of 300 bp DNA labelled with Cy3 and 75 bp DNA labelled with fluorescein. The DNA has been accumulated at the boundary for 240 s using 80 V m$^{-1}$. Subsequently the electric field is gradually increased by 16 V m$^{-1}$ each 20 s. The fragment of 75 bp desorbs at 270 s while the 300 bp DNA desorbs at > 350 s.*

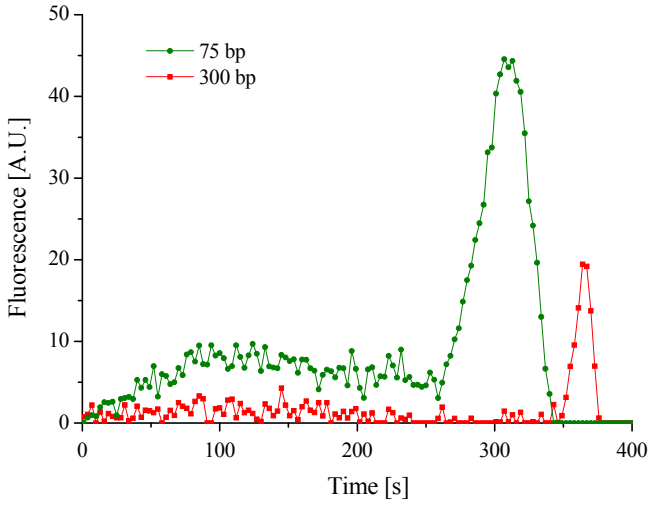


*Fig. 51: Electropherogram according to the separation of two DNA fragments. Measured has been the fluorescence in the PEG phase in a defined narrow window adjacent to the interface.*

In order to obtain more fluorescence data, the latter experiment has been repeated where only one dye is measured, but still both DNA fragments reside in the dextran phase. A narrow window is confined in the PEG phase adjacent to the liquid-liquid interface and the time evolution of the fluorescence intensity is measured. The obtained electropherograms (Fig. 51) from various experiments coincide with the previous

fluorescence observations of Fig. 50. The intensity measured in the PEG phase adjacent to the liquid-liquid interface illustrates a different desorption time for both DNA fragments. It also shows a complete separation of both DNA fragments.

**Estimation of the escape time for 100 and 150 bp DNA**

The previous experiment revealed a DNA size dependent desorption from the boundary in an optical manner, because smaller DNA fragments desorb at lower electric fields and larger ones at higher fields. Now it is interesting to pay attention to the different escape times ($\tau_b$) for two DNA fragments. Firstly, considering the parameters influencing the desorption process that have been evaluated in Chapter 7, it is required to define certain experimental parameters to acquire the data. Two DNA fragments (100, 150 bp) stained with YOYO-1 are used in concentration of 8 pg $\mu l^{-1}$. The dextran phase contains either 100 or 150 bp DNA and is introduced to form a lamella of 300 µm width being sandwiched between two PEG phases. The DNA is adsorbed at the boundary in individual experiments for 100 s at 10 V ($E^{ext}$ = 150 V $m^{-1}$). Subsequently the electric field is increased and the interfacial fluorescence is recorded as proceeded in Chapter 7.4.

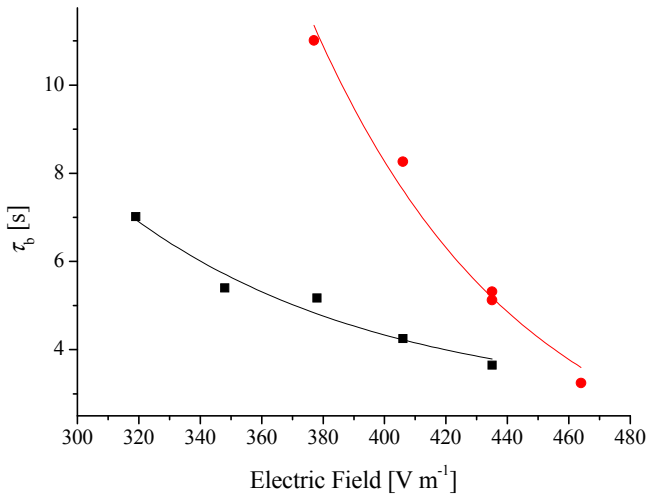


*Fig. 52: Determination of the escape time of a 100 bp (■) and 150 bp (●) DNA fragment.*

The previously observed size separation of DNA is also achieved for the 100 and 150 bp DNA fragment. This is illustrated in Fig. 52 by comparing the escape times obtained from fits of the decay in interfacial fluorescence. The best separation effectivity is achieved at an electric field strength that is just enough to release 100 bp DNA, but not 150 bp DNA. This is accomplished at 320 V $m^{-1}$ when the two curves are diverging.

## 8.3 Separation of various DNA fragments

**DNA separation by a gradually increasing potential technique**

The simultaneous separation of two different sized fragments has evidently proven the possibility of DNA separation using the mass transfer resistance of a liquid-liquid interface. To apply this separation technique to a multitude of DNA fragments more fragments have been isolated from a base pair ladder as described in Chapter 6. The DNA fragments of 190 to 2176 bp are stained with an intercalating dye (YOYO-1) and tested separately in single experiments. It is stressed that each fragment is used in concentrations between 4 - 8 pg $\mu l^{-1}$. The DNA fragments are dissolved in the dextran phase and introduced in a two-lamellae configuration, where each phase occupies one half of the compartment. Due to reasons of increased resolution the potential has been gradually increased by 1 V / 15 s in the separation mode, which corresponds to 9.6 V $m^{-1}$ 15 $s^{-1}$. Beforehand, DNA is accumulated by applying 96 V $m^{-1}$ for 60 s.

The fluorescence intensity of the PEG phase adjacent to the interface is recorded. Instead of plotting the fluorescence intensity versus time, the electric field is indicated on the abscissa by interpolating the increase of 9.6 V $m^{-1}$ over the entire 15 seconds (Fig. 53). This enables to allocate a specific electric field of desorption to each DNA fragment.

The resolution of the separation using fragments < 500 bp is larger than for fragments > 500 bp. This concurs with the tertiary structure of DNA. The radius of gyration increases only slowly for fragments > 500 bp as the molecule enters from a rod-like into

a coiled conformation. Under the respective electrolyte conditions a persistence length of about 50 nm is expected [95, 96], which corresponds to 150 bp taking a 0.34 nm rise per base pair into account. Molecules of a few persistence lengths can be separated by the mass transfer resistance of the liquid-liquid interface (Fig. 53). Some molecules, as observed for the 653 bp DNA fragment, desorb later than larger fragments as the 1230 bp fragment.

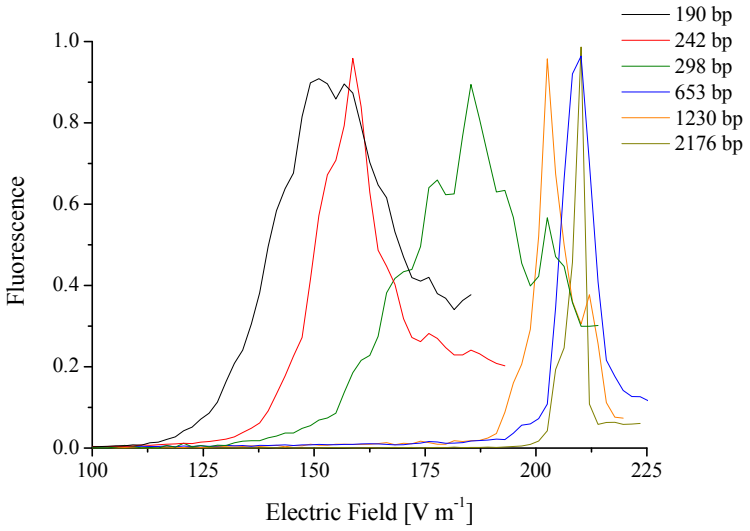


*Fig. 53: Separation of selected DNA fragments with sizes between 190-2176 bp. The fluorescence is measured in the PEG phase adjacent to the interface and normalised to the maximum. Peaks indicate desorption of molecules.*

In the following, the separation of chromosomal DNA has been examined in detail. For such experiments human male chromosomal DNA has been stained with the intercalating dye YOYO-1 and the experiment is repeated as described in this section. Although the chromosomal DNA is far larger than the DNA fragments of Fig. 53, the chromosomes desorb at similar electric field strengths. The separation of large DNA fragments is rather difficult with the given protocol.

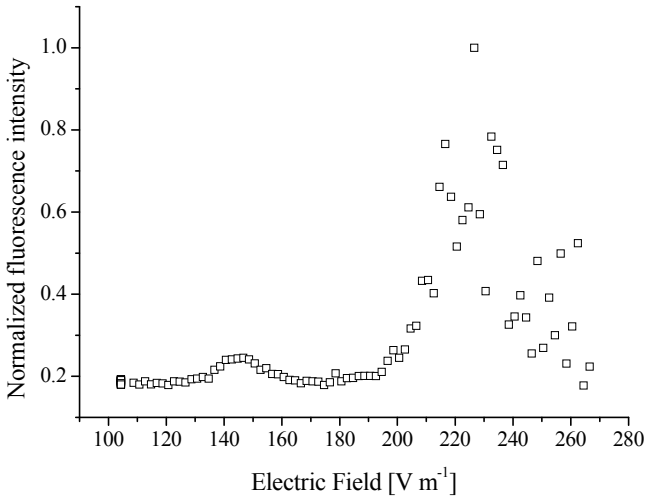


*Fig. 54: One respective experiment of chromosomal DNA separation. The fluorescence is measured in the PEG phase adjacent to the interface indicating desorption of molecules.*

# Chapter 9: Electrophoretic stretching of DNA at liquid-liquid interfaces

## 9.1 Summary

λ-DNA of 48 kbp if extended, is about 17 µm long. Human chromosomes, generally of the order of 100 Mbp (mega base pairs), are even longer and with a sophisticated microscope setup single molecules can be observed in the ATPS. After a short analysis of the DNA structure in the polymer phases, this chapter presents investigations of the liquid-liquid interface employing large magnifications. Fluorescently stained chromosomes elucidate an extension of some molecules in the direction of the applied electric field. Such an interesting behaviour could improve the understanding of the adsorption process itself and moreover, it could provide a microfluidic tool for linear direct analysis of chromosomes or chromosome mapping.

## 9.2 λ-DNA structure in the PEG phase and dextran phase

The characterisation of DNA conformations in a PEG phase and a dextran phase of a standard ATPS in 5 mM Tris/borate pH 8.0 reveals similarities (Fig. 55). Both types, the globular and the coiled conformation of λ-DNA, occur. The coils exhibit intramolecular Brownian motion. The globules remain in their conformation.

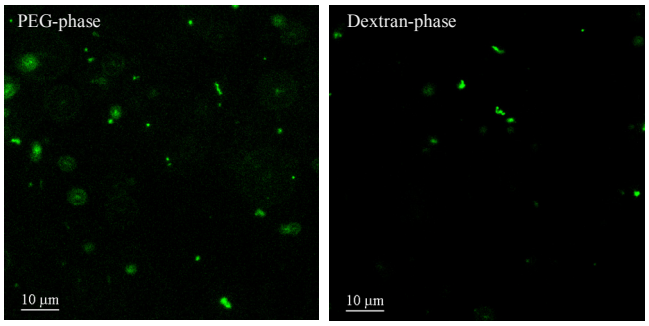


*Fig. 55: λ-DNA in a PEG and dextran phase of a standard ATPS occurs mainly in a globular structure with some extended coils. The coils show intramolecular Brownian motion.*

## 9.3 Interfacial DNA stretching

The ability to position and stretch chromosomal DNA in a microfluidic platform is important for gene mapping technologies such as Linear Direct Analysis (LDA). Current devices use mainly a hydrodynamic flow to stretch DNA [287]. This requires them to be covalently attached to a solid support, which necessitates the chemical modification of the nucleic acid chain with e.g. biotin to attach the molecule to a functionalised substrate. Molecules can be stretched in a hydrodynamic flow while the molecules pass sections of micro obstacles [288]. Krishnan et al. have also shown the stretching ability of DNA in nano slits [289], which is a result of an electrostatic self-assembly of such macromolecules in narrow confined regions [290]. Moreover a multitude of experimental data presents dielectrophoretic stretching of DNA [291, 292].

Herein a technique is presented that does not require a modification of large DNA molecules to stretch them at a liquid-liquid interface. A sample containing human chromosomal DNA has been used in the dextran phase to adsorb electrophoretically at the liquid-liquid interface of a standard ATPS in 5 mM Tris/borate pH 8.0.

While the potential is increased close to the critical value of desorption, some DNA strands stretch into the PEG phase (Fig. 56). Although not all molecules extend at the interface, a sufficient amount of stretched molecules of about 30% can be achieved (Fig. 57A). The life time of the stretched conformation is of the order of a few minutes. Then, the molecules desorb into the PEG phase expected due to the previously discussed time dependent changes of the interfacial energy barrier.

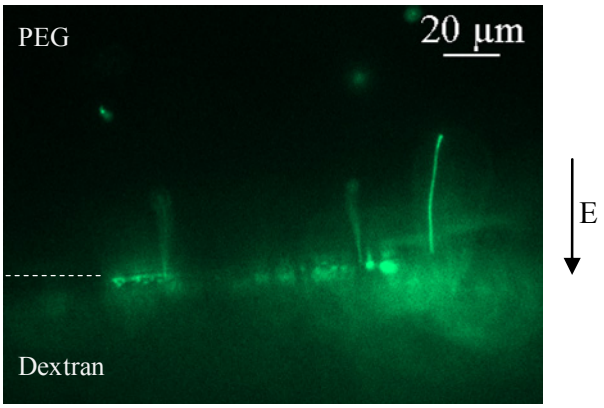


*Fig. 56: Stretched and non-stretched chromosomal DNA at a liquid-liquid interface.*

The typical electric field necessary for stretching molecules at a liquid-liquid interface of a standard ATPS is about 200 V $m^{-1}$ in a bilaminar configuration with equal width for both polymer phases, which is similar to previous applications where DNA has been stretched within nanochannels [293]. The electric field of 200 V $m^{-1}$ is not sufficient to extend the stretching conformation to its full length. In respect to this, more than 5 kV $m^{-1}$ [294, 295] would be required exceeding the trapping forces at the boundary. If the electric field is switched off, DNA molecules switch back into a coiled conformation due to entropic forces and slowly migrate into the dextran phase.

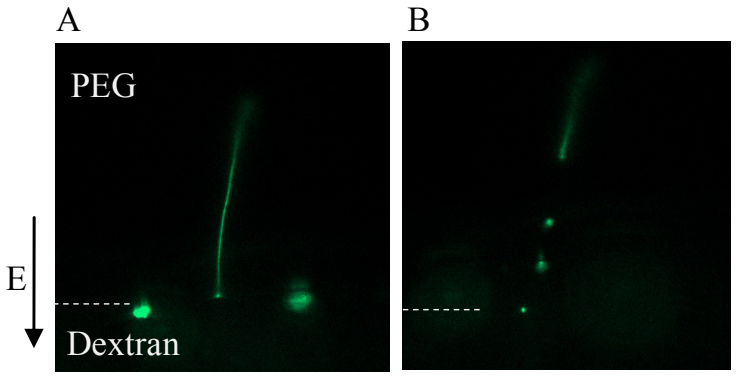


*Fig. 57: A: Three chromosomal DNA fragments with different alignments at the interface. While two molecules remain trapped in a globular conformation, one molecule is in a stretched conformation and touches the interface. B: Laser induced photocleavage of the chromosome at a liquid-liquid interface creates four DNA pieces. Three fragments enter the PEG phase, while one piece remains at the interface.*

Another phenomenon that deserves attention is the laser-induced photocleavage of entire chromosomes. The experiments of Fig. 57 are carried out with a laser power of 10 mW (488 nm, argon). The 100x objective focuses the laser beam and causes a large excitation power per area. It has been repeatedly observed that such large excitation power results in chromosomal breakage of YOYO-1 stained DNA. The pattern of this breakage as shown in Fig. 57B has been reproduced in various experiments. Typically, the chromosome is cut into four parts. The first part is always the longest migrating into the PEG phase. The long part is followed by two small DNA pieces. A fourth DNA piece remains at the interface.

The photocleavage is ascribed to YOYO-1 [296]. This cyanine dye cleaves single-strands in dsDNA at large excitation intensities. Normally, dsDNA would not completely break as shown in Fig. 57B. But stretching of DNA induces thermal melting

and two single-strand breaks in proximity reduce the entire stability of the double-strand helix [252, 296].

# Chapter 10: Discussing DNA adsorption at liquid-liquid interfaces

## 10.1 Summary

Chapters 6-9 present a multitude of cumulative results that solely do not conspicuously delineate the interfacial phenomena of two aqueous polymer solutions. A review onto the entire data is approached to find fundamental principles occurring at a liquid-liquid interface of an ATPS prepared of PEG and dextran. Thus, it is required to summarise the results and put them into a concept that interconnects the data. It is emphasised that the theoretical consideration herein proposed does not fulfil a complete theory. Nevertheless, a well defined discussion is necessary to summarise the results in a manner that encourages investigations in certain directions.

## 10.2 Theoretical considerations

**Potential energy well**

In Chapter 7.4 the potential induced desorption of a 150 bp DNA fragment is investigated. The DNA fragment is adsorbed at the liquid-liquid interface of the ATPS applying a moderate electric field. After some time the electric field is increased to larger values to trigger desorption of DNA into the non-preferred PEG phase. The decay in interfacial fluorescence, and therefore the desorption process, follows an exponential escape indicating a thermally activated process where molecules escape from a metastable state. The depth and possibly width of the energy well alters with the value of the applied electric field. A significant reduction of the energy well induces a thermally activated escape of the molecules into the non-preferred PEG phase in a 5 mM Tris/borate standard ATPS of PEG and dextran.

The time dependent decay in interfacial fluorescence follows

$$f(t) = A\exp\left(-\frac{t}{\tau_b}\right) \qquad 10.2.1$$

where the escape time $\tau_b$ is

$$\tau_b \propto \exp\left(\frac{\Delta F}{k_B T}\right) \qquad 10.2.2$$

In the following it worth to discuss the contributions to a potential energy well depicted as $\Delta F$. In general $\Delta F$ is difficult to determine as it depends not solely on the height, but also on the width of the energetic minimum. Moreover, it is possible that more than one energy minimum exists at the interface. In the following, the possible energy contributions are discussed to evaluate their role in the adsorption process only qualitatively.

**The source of an energy barrier to adsorb DNA**

A major contribution to the adsorption process has been initially thought to be derived from the difference in solvation or better denoted as Gibbs free energy of transfer while the molecule is transported from phase 1 to phase 2. Double stranded DNA prefers the dextran phase at 5 mM ionic strength and partitions practically entirely into this phase. The ability of λ-DNA to adsorb electrophoretically at the interface concurs with a large partition. Increasing the ionic strength reduces the partition difference and dsDNA prefers the PEG phase at > 30 mM and does not adsorb while electrophoretically transported from dextran towards PEG. Remarkably, in ATPSs of 50 mM ionic strength DNA strongly partitions into the PEG phase, but interfacial electrophoretic DNA adsorption is not possible while transferred from PEG towards dextran. Hence, the Gibbs free energy of transfer is not the driving force to enable DNA adsorption.

Surface tension is also not driving an interfacial DNA adsorption. Experimentally it has been found that DNA does not remain at the interface in absence of an externally applied electric field. In addition, DNA repells from the interface if the external electric field is switched off.

It has been found that DNA adsorbs only at the liquid-liquid interface if the ionic strength in the ATPS is below 32 mM, which provides a back-to-back double layer of at least 2 × 1.7 nm. Interestingly, this scale is approximately the thickness of a DNA strand. The diameter of the double helix is about 2.0 nm, and via counterion condensation an effective diameter of about 3.4 nm is assumed. The data indicates, DNA experiences the interfacial electric field as an energy barrier and adsorbs only if the interfacial electric field exerts a monopole force on the molecule. Hence, the interfacial electric field opposes the direction of the applied electric field.

**The size dependent escape**

The applied electric field changes the energy barrier linearly and DNA escapes from the trapped state. It is emphasised that the external electric field could change the width and the height of such an energy barrier and/or well. Eventually, the escape is a process that is determined by Brownian motion and dependent on the translational diffusion coefficient of a DNA molecule (Fig. 58).

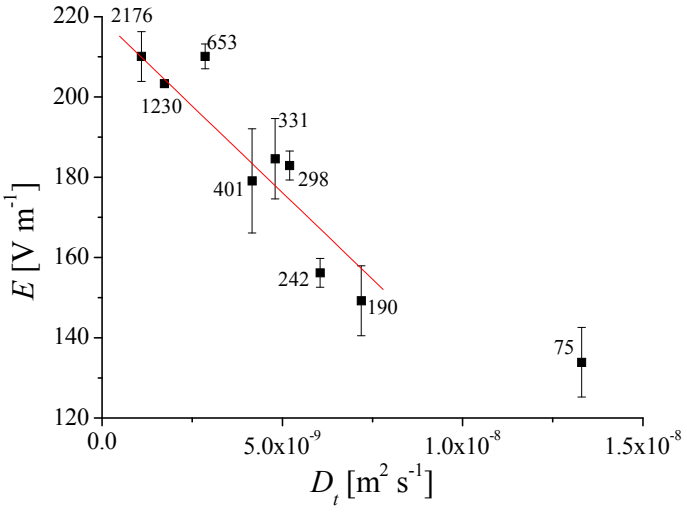


*Fig. 58: The electric field that triggers the maximal desorption shows a linear dependence on the translational diffusion coefficient of DNA between 190 and 2176 bp. The translational diffusion coefficent is estimated using Eq. 3.2.3. The numbers at the data point reflect the DNA size in bp. Error bars represent the deviation for n ≥ 3 experiments of Chapter 8.*

## Conclusion

DNA can be adsorbed at the liquid-liquid interface applying an electric field perpendicular to the interface. The energy barrier to adsorb DNA is suggested to be provided by an interfacial electric field that opposes the direction of the applied electric field. In contrast, if the applied electric field is increased, DNA desorbs from the interface. Desorption is a thermally activated escape that is dependent on the diffusion coefficient, which varies for different sized DNA fragments.

## Outlook

The experiments of this documentation indicate the presence of an interfacial electric field that is directed from the dextran towards the PEG phase. Such an electric field is suggested to provide the energy barrier to adsorb DNA at the liquid-liquid interface applying an external electric field of opposite direction. Although the literature reports Galvani potentials and identifies the dextran phase as negatively charged compared to the PEG phase [192-195, 197], it is not known why the interfacial electric field is reversed. Therefore it requires re-evaluating Galvani potentials in ATPSs or finding theoretical explanations for a polarized liquid-liquid interface.

# Chapter 11: Fabrication of a PMMA device for DNA preconcentration and size separation

## 11.1 Summary

In Chapter 8.3 a new technique of DNA separation has been presented exploiting the mass transfer resistance of a liquid-liquid interface. The reader might ask for the purpose of developing new DNA separation techniques or improving the present options available in lab-on-a-chip technologies. One concern since the introduction of μTAS is the automation of processes. DNA electrophoresis has been widely implemented in microchips or capillary electrophoresis systems for analytical purposes. But biological or clinical oriented laboratories still require time and staff to separate DNA for preparative purposes.

This chapter summarises utilised fabrication techniques and characterises a novel microfluidic setup to investigate the electrophoretic transport of nucleic acids in a PMMA microsystem, where several electrokinetic transport phenomena of DNA are studied. Techniques such as field-amplified sample stacking, isotachophoresis and size separation employing a sieving matrix can be used in this microsystem to separate DNA for preparative purposes. The microchip is inexpensive and applicable as a disposable item. It seems possible to economically apply the developed microchip for the isolation of cell-free fetal DNA from blood of pregnant women for non-invasive prenatal diagnosis. This is the first micro device that exploits a preparative isolation of DNA in a half-automated manner [20].

## 11.2 PMMA micro device for DNA preconcentration and size separation

### Fabrication

A PMMA 7N template of 64 × 43 × 2 mm has been used to micromachine structures on both sides of the material. Microstructuring has been done using a milling machine of type 3-axis model and a software to program the machine. The two-side structured PMMA micro chip is cleaned in isopropanol for 2 - 3 min applying ultrasound and 0.5 M sodium hydroxide, respectively. The chip is extensively rinsed with deionised water and dried under an air flow. A poly(ethylene terephtalate) membrane (Sterlitech, WA) is incorporated using a dedicated welding device applying 160°C for 1 - 2 seconds. The micro device is bonded with self-adhesive poly(propylene) foil (3M).

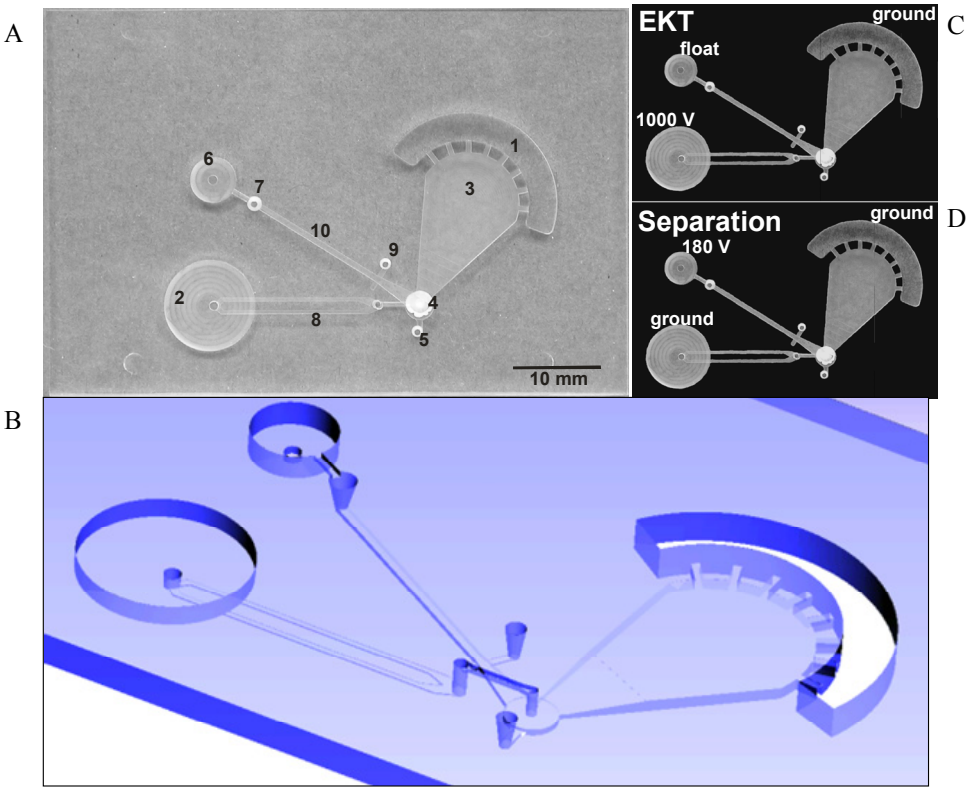


*Fig. 59: PMMA microchip view from underside for size separation of DNA showing cathode reservoir [1], anode reservoir I [2], sample reservoir [3], membrane chamber [4], sample inlet [5], anode reservoir II [6], recovery outlet [7], anode channels [8], a T-crossing valve [9] and a separation channel [10] (A). 3D-model of the upperside (B). The scheme shows a potential application for EKT (C) and transient ITP to perform a preparative size separation of DNA (D).*

Next a solution of either 7% or 9% (w/w) acrylamide containing N,N-methylenebisacrylamide (ratio 60:1) has been prepared in leading electrolyte with a final molarity of 50 mM Tris/HCl pH 8.5 and injected into the separation channel (Fig. 59A, [10]) until the T-crossing (Fig. 59A, [9]). The polymerisation of the acrylamide is ascribed to the addition of TEMED and ammonium persulfate (<0.1%, w/v). The T-crossing serves as a valve to physically separate the fluids from the preconcentration process at the membrane and the separation matrix. Once the anode channels (Fig. 59A, [8]) are filled with terminating electrolyte (5 mM Tris/glycine pH 8.5) a sample solution of DNA in deionised water has been introduced into the sample reservoir (Fig. 60). Eventually anode reservoir I and cathode reservoir are filled with terminating electrolyte and anode reservoir II is filled with leading electrolyte.

Following the preparation of the setup the platinum electrodes are placed into the reservoirs and a software controlled ISEG HV unit serves for an applied potential according to Fig. 59. 30 s before the preconcentration at the membrane is finalised the valve at the T-crossing is opened by cutting the foil in the cross channels, which connects the fluid of the sample chamber with the separation matrix by capillary forces. Subsequently the power supply switches to the ITP mode and applies 180 V at the anode reservoir II and ground to all other electrodes. The electric field guides the DNA into the separation channel to stack using ITP. A transition is made at 350 s when all electrodes are floating and the terminating electrolyte of the cathode reservoir and anode reservoir I is replaced by leading electrolyte. At this point the ITP process stops. The DNA is stacked within the acrylamide matrix and not affected by the electrolyte exchange. Eventually a potential is applied to start the separation process through the acrylamide matrix. The combination of isotachophoresis and separation is called transient isotachophoresis [107].

*Tab. 6: Summary of step by step performance for preconcentration and separation of DNA*

| Processing time | Applied method ($\varphi$) | Note |
|---|---|---|
| 0-300 s | EKT (1000 V) | Preconcentration in front of the membrane |
| 301-350 s | ITP (180 V) | DNA enters the matrix whilst it is stacked via ITP |
| 351-360 s | Break | All electrodes are floating to exchange TE with LE |
| 361- 870 s | Separation (180 V) | Size separation and DNA recovery |

In time intervals of 30 s a recovered sample of 2 µl is collected from the recovery outlet during the separation process. While doing so, fluid from the anode reservoir II refills the recovery outlet automatically ascribed to the back pressure of the filled anode reservoir II. Accordingly the DNA fragments are recouped in different fractions while small DNA fragments are expected in the earlier fractions and larger DNA fragments in the later fractions.

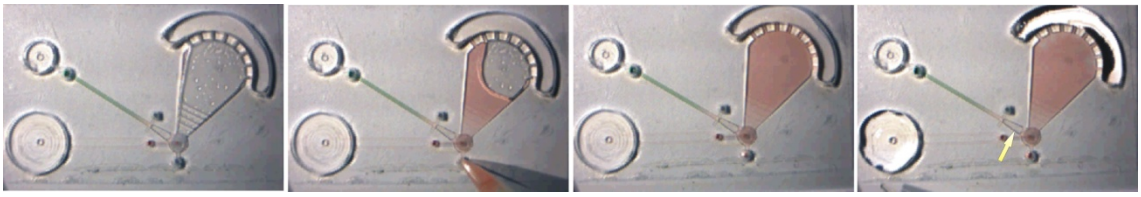

*Fig. 60: Time sequence of filling the microchip with polyacrylamide (green) in leading electrolyte and the sample in deionised water (red). The yellow arrow highlights the air plug at the T-crossing.*

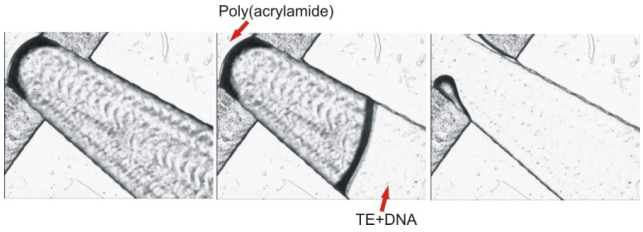


*Fig. 61: Valve at the T-crossing for connecting terminating electrolyte with acrylamide matrix at different time steps. The electroosmotic flow of the anode channels causes a back pressure in the cathodic compartment and additionally, capillary forces drive the fluid to connect with the polyacrylamide matrix.*

The valve (Fig. 61) has not been an absolute requirement to avoid mixing of LE and TE as diffusive transport in the matrix is considerably slow. However, the valve makes the fabrication process easier to prevent the contact of acrylamide solution with the PET-membrane. Certainly when PEG is used as a matrix, the valve hinders PEG to enter the membrane chamber. Both polymers are known to change the zeta potential of the membrane and disable the preconcentration process if they contact the membrane.

**DNA recovery and quantification**

Fractions of 2 µl are manually recovered every 30 seconds in the separation process from the LE-containing and matrix-free recovery outlet (Fig. 59, [7]). Fluid from anode reservoir II refills the outlet due to a higher back pressure and wetting forces subsequent

to any recovery. It is important to hold the pipette with an angle of 90° and touching carefully the ground of the recovery outlet to avoid shifts in the appearance of the fragments. For quantification, the fractions are loaded on a 2% agarose gel stained with GelStar (Lonza). Images of slab gels are saved as 16 bit files. Nucleic acids on slab gels are quantified using ImageJ by integration of peak area while compared to the untreated sample. For a reliable calibration curve 3 different volumes (2, 4 and 6 µl) of the original sample are loaded on a slab gel together with the recovered fractions. Intensity of the bands in the recovered fractions and certain bands were related to the original sample to determine concentration factors. The progression of the calibration curve is linear at the used DNA concentration, which enables a reliable determination of concentration factors.

## 11.3 Experimental setup

**Setup for optical tracking of DNA in a PMMA microsystem for preconcentration and separation of DNA**

The setup to preconcentrate and separate DNA in a microfluidic PMMA chip in general consists of a detection unit, a power supply and the microfluidic device with fluidic connectors. The power supply and a camera of the detection unit are controlled via software. Fig. 62 presents the setup once the microfluidic device is prepared and the platinum electrodes are connected.

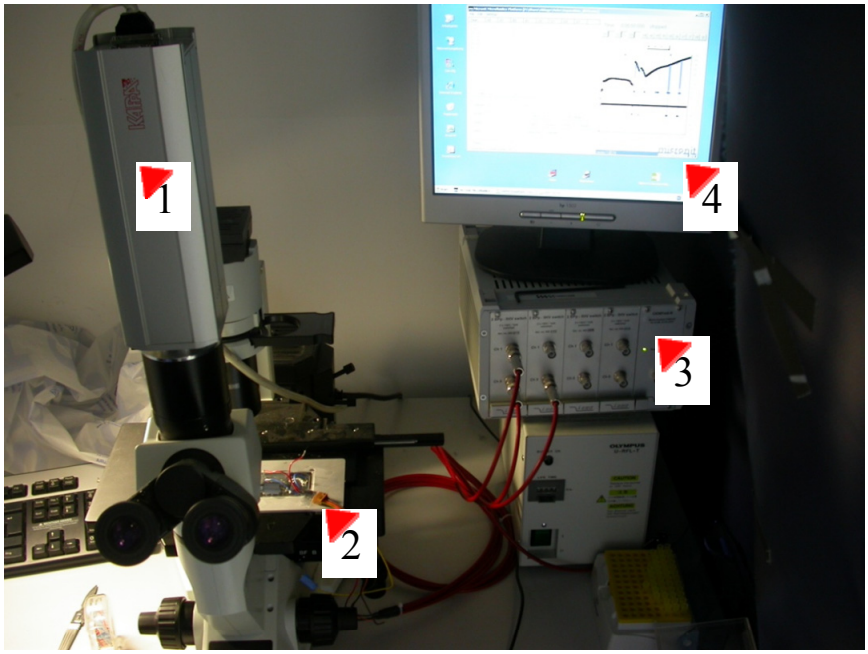


*Fig. 62: The microfluidic chip (2) is placed on the stage of an Olympus microscope eqipped with a camera (1). A computer-controlled (4) ISEG HV power supply (3) provides the direct current.*

Experiments for quantification of the trapping efficiency, either in electrokinetic trapping or isotachophoresis, are performed using a detection unit - an inverse fluorescence microscope (CKX 41, Olympus, Germany) equipped with a fluorescence mirror unit (U-MNB2), excitation band pass filter (470 - 490 nm), emission high pass filter (520 nm) and a camera (DX30, Kappa optoelectronics GmbH) focussing the membrane chamber or the separation channel. Fluorescence images of the DNA are taken at various time intervals, exposed for 192 ms and the signal was amplified 50 fold for electrokinetic trapping experiments. Later, separation experiments are performed without any optical detection during the experiment. Recovered fractions are either stained with GelStar previous to analyse the fractions in an agarose gel for quantification or when real samples from pregnant women are separated the DNA has been directly subjected to a real-time PCR analysis.

# Chapter 12: Preconcentration of nucleic acids

## 12.1 Summary of available preconcentration methods for DNA

DNA preconcentration is required in laboratory praxis of clinical diagnostics or biological analysis and important for commercial use. In particular, microfluidics cope with low sample volumes and a preconcentration is required to obtain a sufficient amount of sample to obey the μTAS concept. A multitude of methods based on various principles are summarised in Tab. 7.

*Tab. 7: Summary of some methods for preconcentration of DNA in microfluidics.*

| Solid-phase extraction | Electrokinetic trapping | Discontinuous electric fields | Liquid-liquid interfaces |
|---|---|---|---|
| Non-covalent | At charged membranes | Field-amplified sample stacking [124] | Aqueous two-phase systems |
| Negatively charged surfaces [297, 298] | At gels [299, 300] | Istotachophoresis [108, 109, 301] | |
| Positively charged surfaces [302, 303] | At nano slits/nanochannels [304, 305] | Field-amplified isotachophoresis [121, 306] | |

Solid-phase extractions of DNA are mainly based on the electrostatic binding of DNA on negatively charged (mostly silica) surfaces using chaotropic agents as bridge ions provoking the interactions. The sample can be eluted from the solid material in solutions of low ionic strength and in a smaller volume resulting in preconcentration [297, 298]. Further attempts have been made to bind DNA onto positively charged surfaces for solid-phase extractions [302, 303, 307]. Another technique is DNA fishing.

SsDNA probes are covalently attached to a material and a complementary ssDNA of a specific sequence anneals at the probes at elaborated temperature conditions [308].

Eventually, electrokinetic trapping appeared as a new technique that evolved from the miniaturisation and the μTAS concept itself. Charged nanopores of a solid material provide an electrostatic barrier for co-charged ion species and can be trapped efficiently applying an electric field across such barriers [121, 309-314]. Besides, a multitude of fundamental research on that topic has appeared [305, 315-322].

Discontinuous electric field preconcentration methods either exploit gradients in the electric field in a microfluidic channel to accelerate a sample ion in a zone of higher field strength to stack in front of a zone of lower field strength, or exploit an isotachophoretic process where sample ions selectively preconcentrate in a zone of a specific electrophoretic mobility. Concerning the former approach, gradients in the electric field can be achieved by altering the electrolyte concentration in the compartments of a microchannel [108, 121, 124, 323-326]. The method is also denoted as field-amplified sample stacking. The latter approach concerning an isotachophoretic preconcentration is achieved by employing two different electrolytes containing sample co-ions of either lower electrophoretic mobility in a trailing (terminating) electrolyte or larger electrophoretic mobility in a leading electrolyte [109, 112, 116, 117, 301, 327].

A new approach for preconcentration of DNA is introduced with this thesis, which relies on the utilisation of a liquid-liquid interface of an ATPS prepared of PEG and dextran. The adsorption or accumulation of DNA at such interfaces has been extensively illustrated in Chapter 8.

This chapter focuses on the combination of several electrophoretic methods and firstly shows a combination of field-amplified sample stacking, electrokinetic trapping at a charged material and an isotachophoresis. An explanation for the physical processes underlying the preconcentration is given and accomplished with a general theory covering electrokinetic trapping in the presented PMMA microsystem.

## 12.2 Electrokinetic trapping – an introduction

The basic understanding of the phenomena nowadays called electrokinetic trapping has been first given by Rubinstein and Shtilman, with their ground-breaking work about current-voltage curves in electrolytes with an incorporated cation exchange membrane [328]. It is described that at higher potentials, which are applied between such permselective nanopores, the current-voltage curve leaves the ohmic regime to establish a 'limiting current' plateau. At even larger potentials the current leaves this plateau and forms a so-called 'over-limiting' regime, which has been found to be required for the establishment of a charge depletion zone on one side of a nanopore and a concentration of charges on the other side [305]. This phenomenon has been called concentration polarization of ions in most of the recent works [316, 317, 329]. Usually concentration polarization is only observed in devices incorporating highly charged nanopores with low ionic strength electrolyte ($c < 0.1$ mM) to obey the condition of larger Debye lengths than the pore radii. Nevertheless some researchers observed trapping of charged species in front of nanopores also in higher ionic strength electrolyte [121, 309, 330]. Presumably, under higher ionic strength (> 1 mM) these nanopores do not provide overlapping Debye lengths and one cannot claim that an electrostatic effect is the only parameter responsible for trapping. In the following it is explained why trapping is still possible.

Certainly, nanochannels imbedded into a microchannel such as in Ref. [331] provide an electroosmotic flow at the microchannel acting hydrodynamically within the adjacent nanopores. Electrokinetic trapping under non-overlapping Debye length conditions using poly(ethylene terephtalate) membranes has been also reported by Zhou et al. [330] and is herein examined in detail. In the following, the latest results for electrokinetic trapping under non-overlapping Debye lengths are summarised by presenting experimental data and a theoretical approach describing the support of a hydrodynamic fluidic counterflow to the trapping process.

## 12.3 Electrokinetic trapping realised with support of a fluidic counterflow and a field-amplification

### Summary

Electrokinetic trapping has been proposed to enrich charged molecules in microfluidics in front of nano structures by charge exclusion. In pores or nanochannels of 10 - 50 nm width the Debye length overlap does not allow charged species to enter the pores being trapped efficiently in front of these nanopores, which carry a surface charge of same sign as the trapped ion. When larger pores of 50 - 200 nm are used, predominantly Debye overlap is not taking place anymore in ionic strength conditions above 1 mM. But under certain conditions, trapping can be achieved at non-overlapping Debye lengths utilising a fluidic counterflow passing the pore. This hydrodynamic flow in a nanopore is produced by an electroosmotic flow in a microchannel adjacent to the nanopore. The investigations of this section give account of the hydrodynamic counterflow to electrokinetic trapping being published in Ref. [121].

### Theory

The so called permselectivity of a membrane initiates a concentration polarization near the nanochannel while an external electric field is applied between an anodic compartment defined as the compartment connecting the membrane with the anode reservoir, and vice versa for the cathodic compartment, connecting membrane with the cathode reservoir. Anions are trapped in the cathodic compartment of the membrane, e.g. DNA, when overlapping Debye layers in the nanopore do not allow DNA to pass the pore. Anions of the electrolyte also experience charge exclusion. The latter event increases the ionic strength in the cathodic compartment and also cations decelerate due to the lower electric field in proximity to the membrane. In the anodic compartment in proximity to the negatively charged nanopores, the ionic strength decreases when fewer anions pass the membrane. Both facts consequently increase the local electric field in

this region. For perfect permselective nanopores, a charge depletion zone, also called space charge, will form on the anodic side of the nanochannel [300, 305, 317, 332].

In a very general approach considering the continuity of this system, the ion flux is described with the Nernst-Planck equation, [121]

$$\frac{\partial c_i}{\partial t} = \nabla c_i \vec{u}_{hydr} - D_i \nabla^2 c_i - \nabla^2 \left( \frac{c_i z_i e D_i \varphi}{k_B T} \right), \qquad 12.3.1$$

at which the potential is described by the Poisson equation,

$$\nabla^2 \varphi = -\frac{\sigma_s}{\varepsilon_0 \varepsilon_r} - \frac{\sigma_f}{\varepsilon_0 \varepsilon_r} = -\frac{\sigma_s}{\varepsilon_0 \varepsilon_r} - \frac{F}{\varepsilon_0 \varepsilon_r} \sum_i z_i c_i \,, \qquad 12.3.2$$

The hydrodynamic flow ($\vec{u}_{hydr}$) is controlled by the electroosmotic flow in the anode channels of the PMMA material according to Eq. 2.5.1. Although the electroosmotic slip at the surface of the substrate remains the same for all channel dimensions, the entire flow experiences a larger backpressure if the anode channels are of larger width or height. Equation 2.5.2 states the velocity of the hydrodynamic flow due to the backpressure that counteracts to the electroosmotic flow in the anode channels. Thus, $\vec{u}_{hydr}$ is the velocity of the net transport of fluid.

**Experimental investigations to EKT**

Firstly, the goal of the work presented in this chapter is ascribed to the understanding of the mechanism of electrokinetic trapping of DNA in front of a negatively charged poly(ethylene terephtalate) membrane in the presented microsystem. Secondly, to obey the requirement to trap DNA from a large volume of 80 µl concerning an application described in Chapter 15, the sample needs to undergo a volume reduction in a preconcentration process.

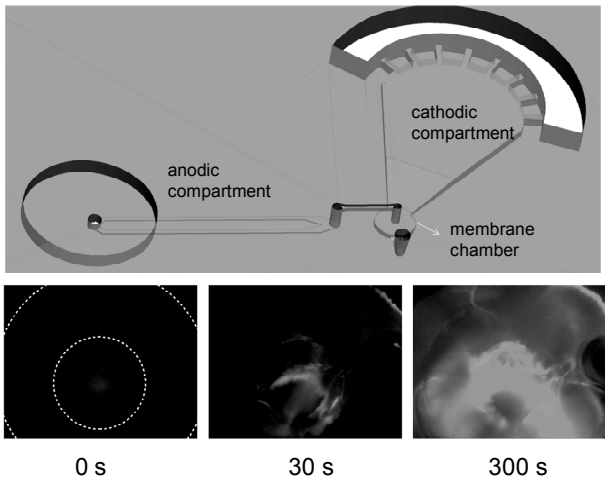


*Fig. 63: Representative fluorescence photos of a 230 bp DNA fragment focusing the membrane chamber bottom-up of a microchip type illustrated on the top. The nucleic acids are certainly distributed over the inner membrane layer that is connected to the perforation (diameter = 600 µm, inner circle) and preconcentrate over time (seconds, s). The perforation connects the membrane chamber and the anode channels on the other side of the microchip.*

The microchip used for electrokinetic trapping is of identical type as the microchip set-up presented in Chapter 12 (Fig. 59) omitting a separation channel (Fig. 63). The preparation process has been identical. To understand the hydrodynamic contribution to the trapping process, three different microchips have been micromachined with different heights in the anode channels connecting the anodic compartment of the membrane with the anode reservoir I.

An electroosmotic slip at the surface of the anode channels produces a fluidic counterflow, if an external potential is applied. This electroosmotic transport suffers from a backpressure due to the fluid in the reservoirs. Thus, different channel heights cause a different hydrodynamic net flow from the anodic to the cathodic compartment with negative zeta potentials for PMMA. This hydrodynamic flow counteracts the electrophoretic transport of DNA, which migrates from the cathodic to the anodic compartment. It is further noted that a different channel height alters the ratio of the electric fields in the compartments. The electric field in the anodic compartment increases if the channel dimensions are reduced compared to the cathodic compartment. The EOF velocity is consequently higher in narrow anode channels.

In order to identify experimentally the most efficient hydrodynamic flow to achieve trapping, anode channels of dimensions (width × height) 350 × 60 µm$^2$, 350 × 100 µm$^2$

and 350 × 200 µm$^2$ have been designed and fluorescence intensities in the membrane chamber indicating preconcentration are compared, as illustrated in Fig. 63. Therefore 200 ng of SYBR Green I fluorescently stained 230 bp DNA has been used in 80 µl 20 mM Tris/borate electrolyte pH 8.5 of homogenous ionic strength in all compartments.

*Tab. 8: The measured hydrodynamic flow concerning the dimensions of the anode channels in homogenous 20 mM Tris/glycine pH 8.5 electrolyte and applied 600 V.*

| Anode channel size (µm × µm) | Hydrodynamic flow (mm s$^{-1}$) |
|---|---|
| 350 x 60 | 3.75 |
| 350 x 100 | 2.3 |
| 350 x 200 | 1.27 |

The different heights in the anode channel revealed a different hydrodynamic flow from the anodic compartment into the cathodic compartment. All anode channels have a width of 350 µm. For the 350 × 60 µm$^2$ channels, no fluorescence in the membrane chamber is observed showing no preconcentration. The hydrodynamic flow is too large and the hydrodynamic velocity exceeds the electrophoretic velocity of DNA in the sample chamber. For anode channels of 350 × 100 µm$^2$ the most efficient preconcentration concerning channel dimensions has been achieved. This is observed comparing the fluorescence intensities occurring in the membrane chamber when an electric field is applied (Fig. 64). In the following, only microchips with anode channels of dimensions 350 × 100 µm$^2$ have been used.

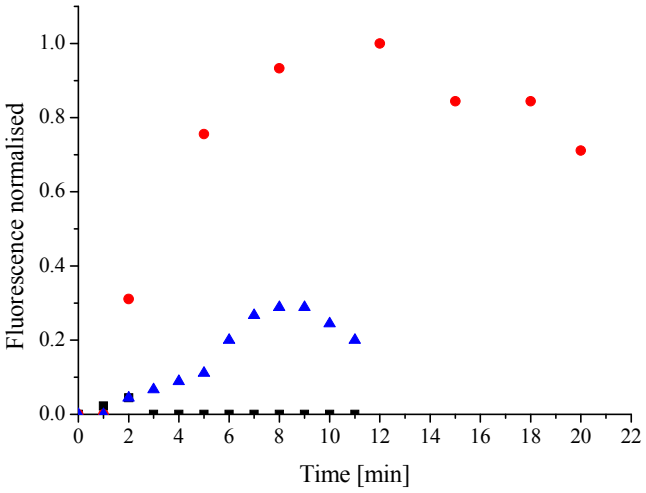


*Fig. 64: Different microchips with various heights of the anode channels reveal different fluorescence intensities in the membrane chamber due to preconcentration of DNA. The anode channels provide a different hydrodynamic flow; (■) 60 µm, (●) 100 µm and (▲) 200 µm. It is seen that anode channels with dimensions of 350×100 µm² provide best efficiency for trapping 230 bp DNA in front of the membrane.*

The hydrodynamic flow produced by the anode channels has been elucidated as an important parameter in the trapping process. However, for electrokinetic trapping a charged membrane has been required. In order to give evidence for a charge-dependent trapping process, a PET membrane of 100 nm pore size has been dynamically coated with poly(ethylene glycol) - a compound known for covering surfaces to eliminate surface charges [213]. In these experiments, the fluorescence remained constant at a low level and therefore, no preconcentration has been observed in the membrane chamber using such a membrane. The same has been observed using uncharged polypropylene membranes of 200 nm pore size. Eventually this shows that highly charged nanopores are required for electrokinetic trapping in the presented device.

Moreover, the use of a homogenous distributed 20 mM electrolyte clearly represents that overlapping Debye lengths are not required to achieve trapping. However, the trapping suffers from inefficiencies as not all DNA molecules of the previously introduced sample can be trapped. DNA passes the membrane before the preconcentration process is finalised. Therefore, a field-amplified approach has been chosen to increase the local electric field in the sample chamber. This is achieved by preparing the sample in deionised water while the surrounding electrolyte, which has been filled into the cathode reservoir and anode reservoir I, is of 5 mM Tris/glycine pH

8.5. A sample prepared in 5 mM electrolyte and surrounded by 20 mM electrolyte has given similar trapping efficiencies, but as discussed in a subsequent chapter a following separation is improved with lower ionic strength in the herein denoted terminating electrolyte.

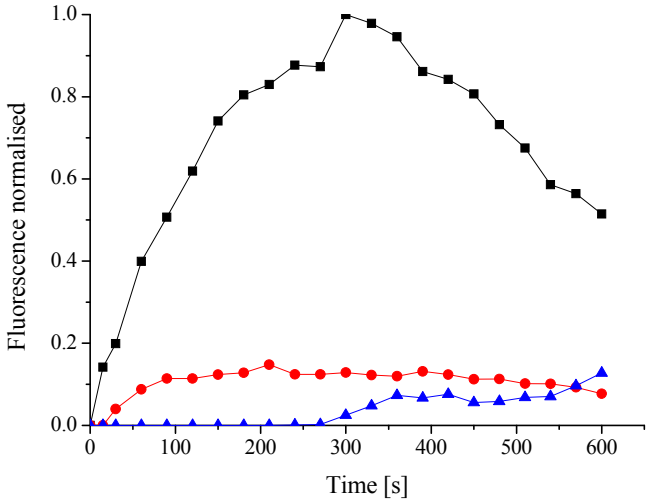


*Fig. 65: Fluorescence intensity of dsDNA in front of a PET membrane (100 nm pores) with field-amplified EKT [■], without field-amplification [●], and fluorescence intensity behind the membrane with a field amplification showing the loss [▲].*

A field-amplification in the sample chamber enables trapping of the entire sample in front of the membrane within about 250 - 300 s (Fig. 65). Later, the DNA passes the membrane expected due to an increased diffusion potential, a decreased hydrodynamic flow and decreased Debye length at the nanopore. The hydrodynamic flow decreases linear with the time ($t$) in the experiments by $u_{z,r}(t) = (7.19 \times 10^{-3}\, t + 17.15)$ in mm $s^{-1}$ within the first 600 s at applied 1000 V. The decrease of the hydrodynamic flow is explained in view of the field-amplified approach, when the conductivity in the anode channels increases with time and the velocity of an electroosmotic flow decreases due to a lower electric field in these channels.

## 12.4 Isotachophoresis

In the previous section, electrokinetic trapping of a large volume sample has been advanced to preconcentrate DNA in front of a membrane. In view of an application for a preparative size separation of DNA in microfluidics, the sample requires further stacking within a smaller microchannel. Isotachophoresis is shown to be a reasonable stacking technique that is fully compatible to the previous field-amplified electrokinetic trapping approach if electrokinetic trapping is done in a buffer with sample co-ions of lower electrophoretic mobility to fulfil the required properties of a terminating electrolyte. Moreover, if a transient isotachophoresis is used, the DNA undergoes a size separation after a stacking procedure induced by an exchange of terminating electrolyte with leading electrolyte. Therefore, a separation channel has been introduced connecting the membrane chamber with anode reservoir II (Fig. 59). By this means, the connection of the fluid within the membrane chamber and the matrix in the separation channel is accomplished. To establish a convenient coupled field-amplified electrokinetic trapping isotachophoresis polyacrylamide has been used as a sieving matrix within the separation channel.

Transient isotachophoresis requires a sieving matrix to separate DNA. In that case, isotachophoresis is used to stack the DNA at the first part of the separation channel. Afterwards, the potential is switched off and the terminating electrolyte of the cathodic compartment is exchanged with leading electrolyte to provide homogenous buffer conditions over all compartments. Eventually, a traditional microchip electrophoresis is designed that separates DNA fragments due to their size dependent retardation within a polyacrylamide gel.

Beside the nature of isotachophoresis to stack charged molecules of same electrophoretic mobility, it allows separation of molecules with different electrophoretic mobility. The small decay in the electrophoretic mobility for DNA less than 500 bp can be used to separate DNA of different size without employing a transient electrolyte exchange. In a short communication this is shown in the following section.

# Chapter 13: Size separation of DNA in a PMMA microsystem

## 13.1 Summary

The previous chapter described the fundamental principles of the preconcentration process used to stack DNA in a microchannel (denoted as separation channel). To obey the requirement of a preparative size separation the DNA sample is electrophoretically transported into the separation channel. Two setups are investigated. In a first approach, isotachophoresis is utilised to separate DNA fragments of 230 bp and 510 bp according to their different electrophoretic mobilities. The advantages and disadvantages are discussed. Later, a traditional approach based on capillary electrophoresis in a microchip is utilised to separate DNA from 100 to 1000 bp in a preparative manner.

## 13.2 Size separation of DNA < 500 bp using isotachophoresis

Remarkably, isotachophoresis can be used in microfluidics to separate small DNA fragments of sizes less than 500 bp. The theoretical approach for this phenomenon has been given already many years ago. Beside Nancy Stellwagen many researchers have contributed to the understanding of the size dependent electrophoretic mobility of DNA. Although the electrophoretic mobility remains constant for DNA fragments larger than 500 bp, it decreases slightly with decreased DNA length of fragments less than 500 bp [85]. In this work it has been exploited to separate DNA of small fragment lengths. In view of the microchip applicability to separate cell-free fetal DNA from maternal blood plasma, it is wished to isolate DNA of less than 300 bp from any larger ones. For illustration, a 230 bp fragment and a 510 bp fragment has been constructed by polymerase chain reaction (PCR) to elucidate the following results.

The microchip used for electrokinetic trapping has been advanced by a neighbouring separation channel elongating from the membrane chamber. Once all nucleic acids of the sample chamber are preconcentrated at the membrane, the potential is applied at the

end of the newly designed separation channel. For understanding the chip design of Fig. 59 in Chapter 12 is recalled in Fig. 66.

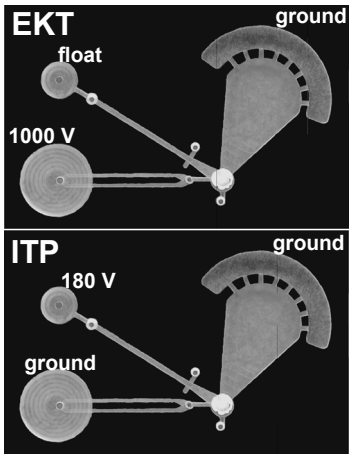


*Fig. 66: The microchip as previously presented is exploited for an isotachophoretic separation of DNA. The separation channel and anode reservoir II are filled with leading electrolyte containing 2% PEG (MW 6,000) while all other compartments are filled with terminating electrolyte.*

The leading electrolyte within the separation channel contains 2% poly(ethylene glycol) to increase the viscosity and reduce the band width of the DNA plug. Subsequent to an electrokinetic trapping, the potential is applied in the anode reservoir II while all other electrodes remain at ground.

A sharp band of stained DNA migrates along the separation channel and two fragments of 230 and 510 bp are detected (Fig. 67). The separation distance of the two fragments is expected to be zero, but impurities of ions may reside in the system. Analytically, the separation of several micro metres is sufficient to distinguish the DNA fragments, but a preparation is difficult to achieve and relies on unknown factors such as impurities.

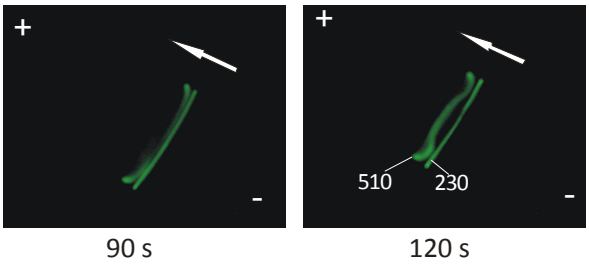


*Fig. 67: Isotachophoretic separation of two different DNA fragments with sizes of 230 bp and 510 bp. Terminating electrolyte is 20 mM Tris/glycine pH 8.3 and leading electrolyte 50 mM HCl in 2 % poly(ethylene glycol). The arrow indicates the direction of the electrophoretic transport.*

The system requires improvements of the separation process. The chosen electrolyte of Tris/glycine as the terminating electrolyte and Tris/HCl as the leading electrolyte offers respectively, smaller and larger electrophoretic mobilities than DNA, the preliminary requirement for isotachophoresis. The chloride ions exceed largely the DNA mobility. It is conceivable that a different combination of electrolytes could improve the separation process. For instance, if an additional anion with an electrophoretic mobility between two DNA fragments resides in the system, the separation distance could be improved.

Another experimental problem that occurs is the inconvenience of a PEG solution adjacent to a highly charged membrane. Although both compartments are separated with an air plug in between, the PEG solution gets easily in contact with the membrane. In consequence, the membrane surface charge is diminished and electrokinetic trapping fails. Therefore, it is more convenient to perform a transient isotachophoresis and employ a solidified sieving matrix such as polyacrylamide for size separation due to a sieving effect. The isotachophoretic stacking is still used to stack the sample within the separation channel. The separation process is carried out in the following section.

## 13.3 Conventional size separation of 100 - 1000 bp DNA utilising a transient isotachophoresis in a sieving matrix

**The experimental process of a conventional size separation**

Size separation of DNA, just by isotachophoresis by exploiting the size dependence in the electrophoretic mobility, is convenient for DNA fragments less than 500 bp, but the separation distance between a 230 bp and 510 bp DNA fragment is not sufficiently large to enable preparative size separation without optical detection. Thus, it has been motivated to perform conventional size separation employing capillary electrophoresis in a microchannel that has been previously filled with a sieving matrix. Such a conventional approach is combined with isotachophoresis.

The microfluidic setup and the process of sample preparation have been extensively described in Chapter 12. For reasons of comprehension, here the process is only summarised. After preparing the microchip with a polyacrylamide matrix in the separation channel, a potential is applied at the anode reservoir I to stack the DNA in front of the membrane by electrokinetic trapping. This step reduced the initial sample volume from 80 µl to 2 - 3 µl in the membrane chamber. The sample is initially dissolved in deionised water, while the reservoirs are filled with terminating electrolyte (5 mM Tris/glycine pH 8.3). This leads to a field-amplification in the sample chamber improving the stacking process as described previously. The electrolyte provides with glycine an anion with a lower electrophoretic mobility than DNA. Therefore, the subsequent application of a potential in anode reservoir II guides the DNA into the separation channel by an isotachophoretic process, as the anode reservoir II and matrix are filled with leading electrolyte. The leading electrolyte contains chloride as an anion with a larger electrophoretic mobility than DNA. The acrylamide matrix has been also prepared in leading electrolyte.

DNA accumulates at the beginning of the acrylamide matrix in the isotachophoretic process. Eventually, the potential is switched off for 20 s and all electrodes are grounded to allow an electrolyte exchange. The reservoirs are filled with the leading electrolyte to provide homogenous electrolyte conditions. The separation process is initiated by applying again a potential at the anode reservoir II. The entire process is controlled by the software of the power supply guaranteeing reproducibility in an automated manner. DNA fragments are recovered every 30 s from the recovery outlet in 2 µl fractions and quantified on an agarose gel using ImageJ software [333].

**DNA size separation of a 100 bp ladder**

The reliability of the microchip to separate DNA fragments mainly of sizes around hundreds of base pairs is investigated. The length of the separation channel and the matrix contribute mainly to the separation efficiency in microchip electrophoresis. In view of an application for a preparative DNA separation, a base pair ladder is used containing 11 fragments between 100 - 1000 bp.

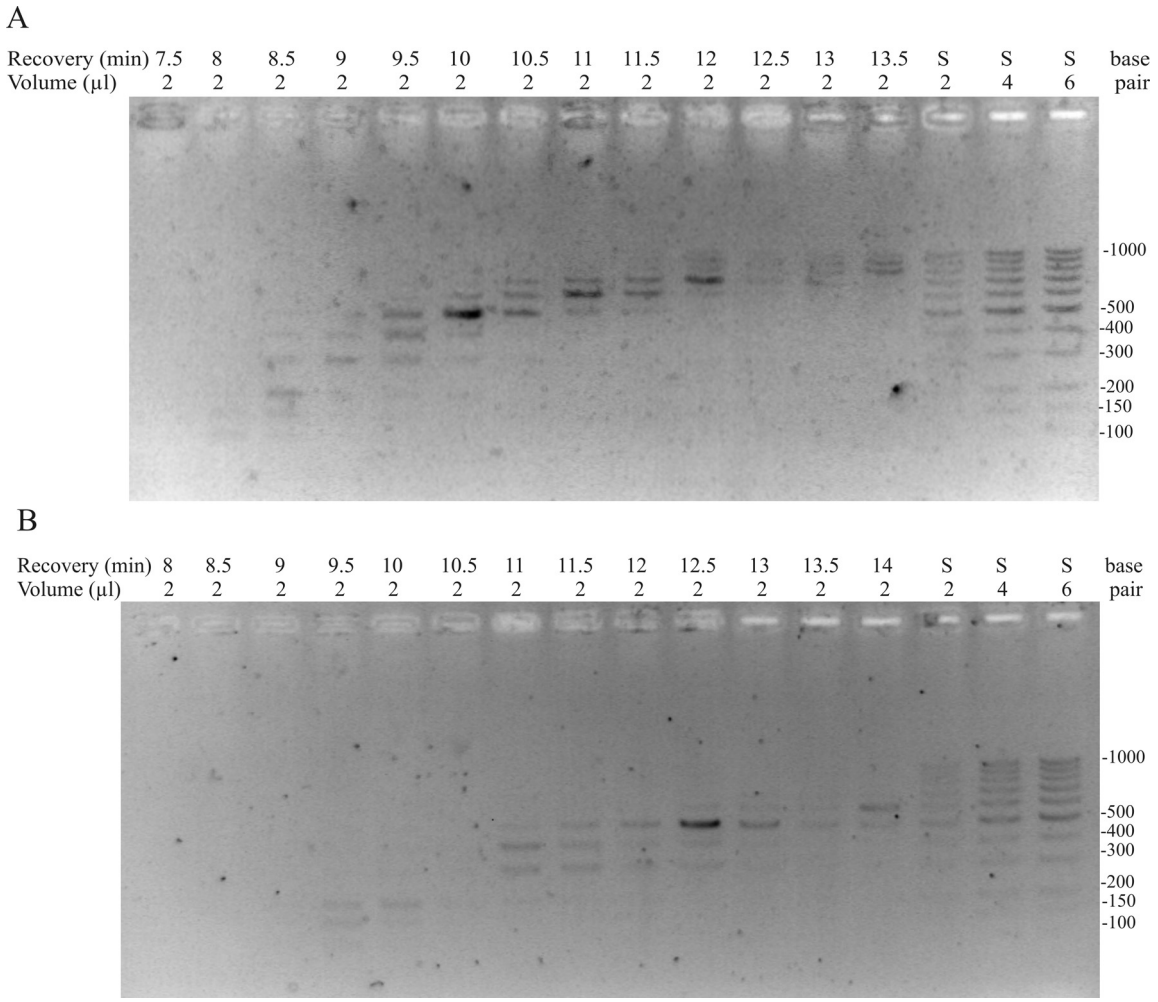


*Fig. 68: Original images from two gel separations in 7% polyacrylamide (A) and 9% polyacrylamide (B). The lanes denoted with 'S' are the untreated sample fractions in different concentrations (2-6 µl volume) to compare the obtained band intensities of the recovery fractions (7.5-14 min) with the original sample. The right hand side annotations reflect the fragments size in base pairs (100-1000 bp).*

The recovery fractions of 2 µl volume are transferred to an agarose gel to detect the separated DNA fragments from 7.5 min experimental time. The intensity of the DNA bands that have been recovered and separated again in a conventional agarose slab gel can be directly correlated to the DNA concentration. The slab gels enable the comparison of the recovered fractions with the sample fractions (S) that have been co-separated (Fig. 68, right lanes).

The concentration of the polymerised acrylamide determines the separation specificity. Acrylamide in concentrations of 7% (wt) allows a separation of a fragment range between 100 - 1000 bp DNA (Fig. 68A). In order to improve the specificity to separate

DNA fragments between 100 - 500 bp the acrylamide content has been increased to 9% (wt). The denser matrix improved the separation for smaller DNA fragments (Fig. 68B). For better visibility the recovery fractions from a separation in 7% (wt) acrylamide (Fig. 68A) is plotted in an electropherogram in Fig. 69 and for a separation corresponding to 9% (wt) acrylamide (Fig. 68B) in Fig. 70. The electropherograms depict the concentration factors of various fragments achieved in the entire microfluidic process.

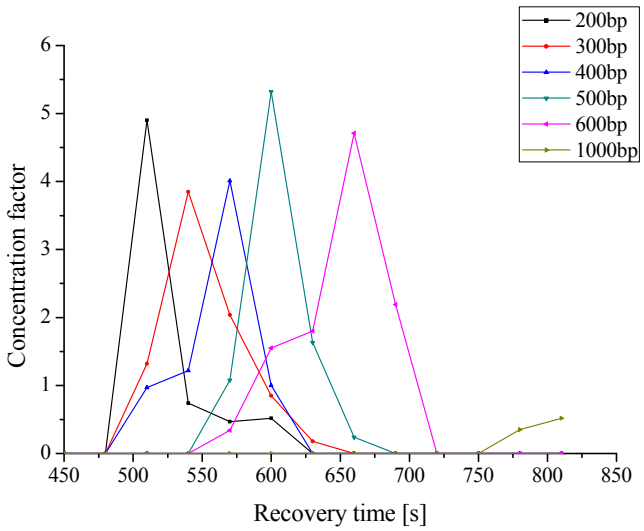


*Fig. 69: Electropherogram of preparative isolation of DNA fragments in 7% polyacrylamide.*

The reproducibility has been tested by separating the 100 bp ladder in different microchips of the same kind. The average fraction content of 8 experiments is plotted in Fig. 71. The fractions at 9 to 10.5 min experimental time are the most interesting ones to isolate DNA fragments between 150 - 300 bp. In the following chapter the relevance for these DNA size is illustrated in view of an application to isolate cell-free fetal DNA from maternal blood of pregnant women.

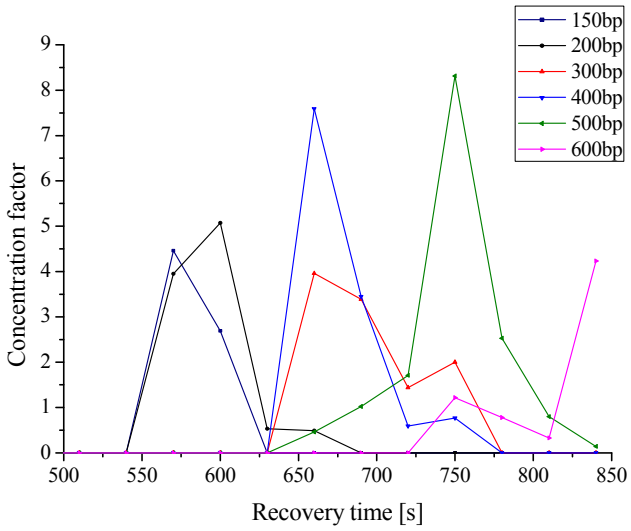


*Fig. 70: Electropherogram of preparative isolation of DNA fragments in 9% polyacrylamide. The 150 and 200 bp DNA fragments are fully separated from DNA > 300 bp.*

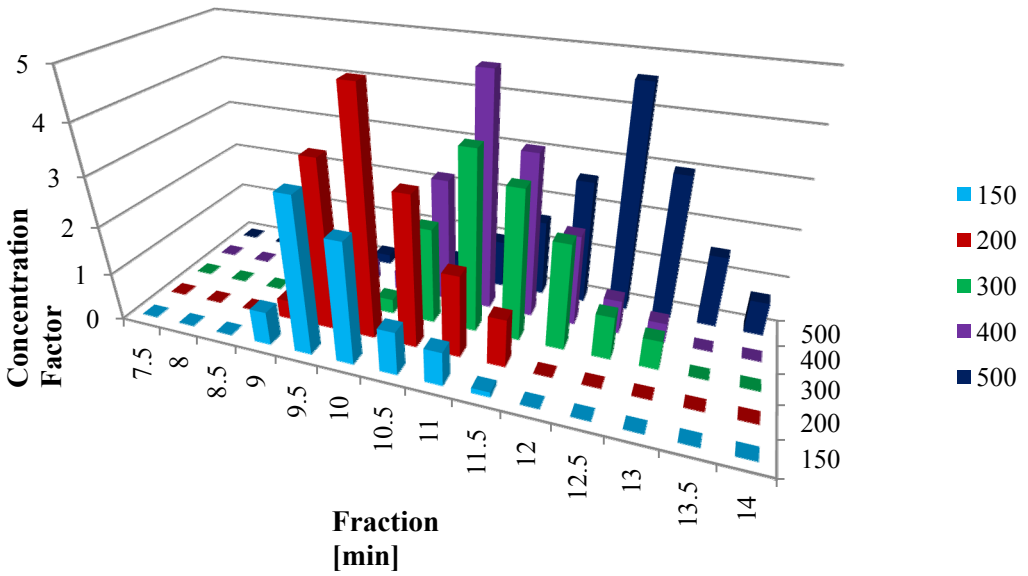


*Fig. 71: Electropherogram of 8 averaged separations in a 9% acrylamide matrix of DNA fragments between 150 and 500 bp (right scale in the figure).*

# Chapter 14: Applications for DNA size separation in microfluidics

## 14.1 Summary

It is known that cell-free fetal DNA circulates in maternal blood of pregnant women and can be used to perform non-invasive prenatal diagnosis. Cell-free fetal DNA in maternal plasma is mainly less than 300 bp and can be separated from the maternal DNA that is mainly larger than 500 bp [18, 19, 334]. Although the size difference of maternal and fetal DNA is known for several years, clinical laboratories have not accomplished protocols that enable a convenient preparation procedure for a manual practice. A manual gel separation is time consuming and not affordable on a large number of samples. Eventually, the idea is grown to transfer the preparative size separation of DNA onto a micro total analysis system. Hence, the microchip described in Chapter 12 is consulted for an isolation of fetal DNA. The successful applicability to separate DNA from an artificial base pair ladder has been already shown in Chapter 14. The developed protocol has been specifically designed to isolate DNA fragments of 150-300 bp. The DNA fragments are recovered in several fractions being available for further analytical purposes.

Eventually, to evidently prove the isolation of free fetal DNA, the recovery fractions are used for real-time polymerase chain reaction (PCR) analysis [335]. Here a fragment of the Leptin (*LEP*) gene is amplified to show the overall presence of DNA in the recovery fractions. The PCR technique solely amplifies a fragment being present in the sample and gives consequently a fluorescence signal. The maternal DNA and fetal DNA contain the *LEP* gene. This gene is expected in all recovery fractions. The presence of fetal DNA in a fraction is proven by real-time PCR amplification of a fragment of the sex determining region Y (*SRY*). Only the male fetus is carrier of a Y-chromosome and by amplifying *SRY*, a fluorescence signal proves the presence of fetal DNA in the fraction.

## 14.2 Isolation of cell-free fetal DNA from maternal plasma by preparative size separation

**Experimental procedures to prepare the plasma sample and to perform real-time PCR**

Maternal plasma of pregnant women with a male fetus in the 3rd trimester has been kindly provided by Aicha at Soussan and Ellen van der Shoot (Sanquin, Amsterdam) The manual Chemagic Viral RNA/DNA Kit (Chemagen, Germany) has been used for total DNA extraction from maternal plasma. The supplier's protocol is followed and performed 5 times, with 200 µl plasma extractions, eluting the DNA in 5 x 60 µl deionised water in 1.5 ml reaction tubes. Following total DNA extraction from the maternal plasma, the preconcentration and separation process is executed in an automated fashion on the developed microsystem. Three eluates from DNA extractions are sufficient to perform three separation experiments, for each fragment of the same plasma sample for *LEP* or *SRY* directly after extraction. A thorough rinsing of the microchip with deionised water is required to completely remove remaining salts that could affect the preconcentration at the membrane.

The following recovery fractions of a separation experiment are combined to obtain 6 µl volume per fraction: 9, 9.5 and 10 min (fraction 1); 10.5, 11 and 11.5 min (fraction 2); 12, 12.5 and 13 min (fraction 3); 13.5, 14 and 14.5 min (fraction 4). Combining three fractions ensures a sufficient amount of molecules available for the real time PCR analysis. In order to obtain a negative control at the beginning of an experiment, a 6 µl sample is taken from the anode reservoir II (fraction NC).

A Biorad Q5 thermocycler is used for the real-time PCR analysis using SYBR Green I in combination with a melting curve analysis. Primer sequences for a 105 bp leptin fragment and a 107 bp SRY fragment are used. Leptin is amplified with the forward primer 5'-CAGTCTCCTCCAAACAGAAAGTCA-3' and the reverse primer 5'-GTCCATCTTGGATAAGGTCAGGA-3' while for SRY the forward primer 5'-AAAGGCAACGTCCAGGATAGAG-3' and the reverse primer

5'-TGAGTTTCGCATTCTGGGATT-3' is used. Real-time PCR protocols are performed as followed. Denaturation of DNA is done at 95°C, 30 s, annealing at 55°C for 30 s, elongation at 72°C for 30 s. To amplify *SRY* 50 PCR cycles are used, and for *LEP* 40 cycles are sufficient. For each PCR experiment 6 µl of template (fraction 1-4 and fraction NC) is used in a 15 µl total volume.

**Isolation of fetal DNA from maternal blood and *SRY* detection**

Maternal plasma of pregnant women contains cell-free fetal DNA, and if the fetus is male, the plasma presumably contains all genes from the Y-chromosome, the mother is not a carrier of. Therefore, DNA amplification by polymerase chain reaction (PCR) of *SRY*, which is located on the Y-chromosome, is only successful if a sufficient amount of fetal DNA is present in the sample. It has been mentioned that cell-free fetal DNA circulating in maternal plasma of pregnant women is mainly less than 300 bp. [17-19] Thus, the entire DNA content that has been isolated from such maternal plasma is introduced into the microchip and the established separation protocol of Chapter 14 is followed. The separation of an artificial base pair ladder has shown that the fraction around 9-10.5 min contains DNA of the size 150 - 300 bp being herein proposed to be fetal derived. In the following the recovered fractions of a preparative microchip-promoted size separation are used to detect a fragment of the *LEP* gene and *SRY*. *LEP* is a housekeeping gene that the mother and the fetus is a carrier of. It serves as a positive control showing that DNA is present in the recovery fraction. *SRY* is loacted on the Y-chromosome and serves as a fetal DNA signal. The presence of *SRY* and *LEP* in the same fraction shows that DNA of the fetus is present. It cannot be excluded that maternal DNA is completely absent, but shown to be reduced for DNA < 300 bp. [18, 19] A detection of *LEP*, but no *SRY*, is a signal for the absence of fetal DNA, but presence of maternal DNA in the recovery fraction.

The real-time PCR is followed by the detection of a fluorophore (SYBRGreen, Invitrogen) that intercalates into dsDNA and provokes fluorescence excitation. The amount of fluorescence is consequently a signal for the amount of product synthesised. However, a quantitative estimation can be only done while comparing $C_t$-values of the

real-time PCR amplification. In general, the $C_t$-value is determined from the threshold of fluorescence above the background. In this examination only qualitative evidence is given as the number of samples proceeded do not allow an estimation of the $C_t$-value.

In Fig. 72 the fraction at 0 min serves as a negative control. It is expected that the recovered fraction at the beginning of the experiment does not contain any contamination of DNA and do not show any fluorescence apart from a background. The *LEP* gene is detected in almost all fractions between 9 - 13.5 min. *SRY* is only present in fraction between 9 - 10.5 min. The experiment as a prove of principle shows that cell-free fetal DNA circulating in maternal blood is indeed of shorter size and can be isolated with the proposed microchip. However, the complexity of the system brings difficulties in the reproducibility whilst coping with real samples in a half-automated manner. Further, not sufficient data is available to confirm a preconcentration of DNA, if real samples are processed.

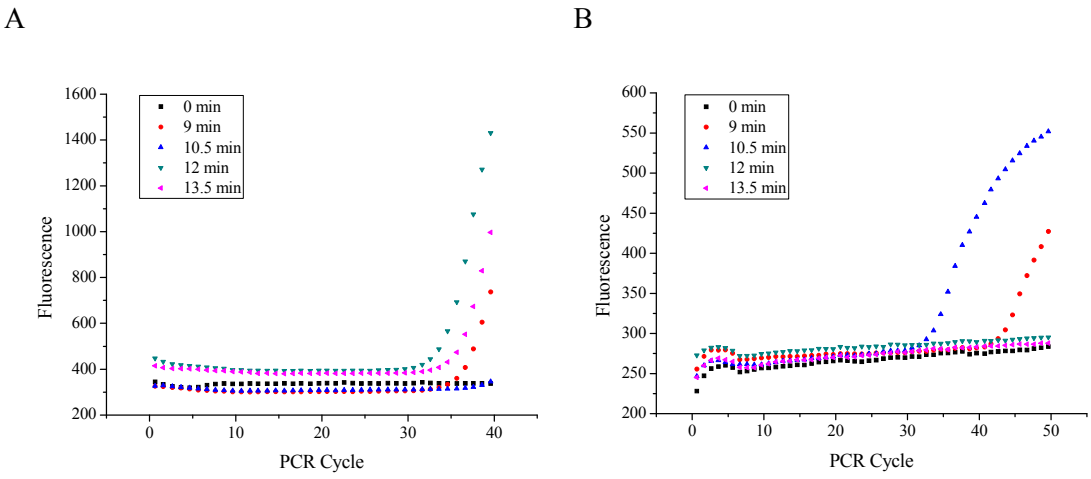


*Fig. 72: Real-time PCR of LEP (A) and SRY (B) from different recovery fractions show the presence of fetal DNA in 9-10.5 min fractions. The sample at 0 min represents the negative control showing no contaminations during the fabrication process. Fluorescence intensities are given in arbitrary units (A.U.).*

## References


1. Manz A, Graber N, & Widmer HM (1990) Miniaturized total chemical analysis systems: A novel concept for chemical sensing. *Sensor Actuator B Chem* 1(1-6):244-248.
2. Lin YW, Huang MF, & Chang HT (2005) Nanomaterials and chip-based nanostructures for capillary electrophoretic separations of DNA. *Electrophoresis* 26(2):320-330.
3. Fetzer R, Rauscher M, Munch A, Wagner BA, & Jacobs K (2006) Slip-controlled thin-film dynamics. *Europhys Lett* 75(4):638-644.
4. Baumann M, Baxendale IR, & Ley SV (2008) The use of diethylaminosulfur trifluoride (DAST) for fluorination in a continuous-flow microreactor. *Synlett* (14):2111-2114.
5. Baumann M, Baxendale IR, Martin LJ, & Ley SV (2009) Development of fluorination methods using continuous-flow microreactors. *Tetrahedron* 65(33):6611-6625.
6. Hessel V (2009) Novel Process Windows - Gates to Maximizing Process Intensification via Flow Chemistry. *Chem Eng Technol* 32(11):1641-1641.
7. Hovorka R (2006) Continuous glucose monitoring and closed-loop systems. *Diabet Med* 23(1):1-12.
8. Santini JT, Cima MJ, & Langer R (1999) A controlled-release microchip. *Nature* 397(6717):335-338.
9. Santini JT, Richards AC, Scheidt R, Cima MJ, & Langer R (2000) Microchips as controlled drug-delivery devices. *Angew Chem Int Ed Engl* 39(14):2397-2407.
10. Sinville R*, et al.* (2008) Ligase detection reaction for the analysis of point mutations using free-solution conjugate electrophoresis in a polymer microfluidic device. *Electrophoresis* 29(23):4751-4760.
11. Schouten JP*, et al.* (2002) Relative quantification of 40 nucleic acid sequences by multiplex ligation-dependent probe amplification. *Nucleic Acids Res* 30(12):e57.
12. Ashton R, Padala C, & Kane RS (2003) Microfluidic separation of DNA. *Curr Opin Biotechnol* 14(5):497-504.
13. Dolnik V, Liu S, & Jovanovich S (2000) Capillary electrophoresis on microchip. *Electrophoresis* 21(1):41-54.
14. Guijt RM, Evenhuis CJ, Macka M, & Haddad PR (2004) Conductivity detection for conventional and miniaturised capillary electrophoresis systems. *Electrophoresis* 25(23-24):4032-4057.
15. Lacher NA, Garrison KE, Martin RS, & Lunte SM (2001) Microchip capillary electrophoresis/electrochemistry. *Electrophoresis* 22(12):2526-2536.
16. Mitnik L*, et al.* (2001) Recent advances in DNA sequencing by capillary and microdevice electrophoresis. *Electrophoresis* 22(19):4104-4117.

17. Bianchi DW (2004) Circulating fetal DNA: its origin and diagnostic potential - a review. *Placenta* 18:S93-S101.
18. Chan KC*, et al.* (2004) Size distributions of maternal and fetal DNA in maternal plasma. *Clin Chem* 50(1):88-92.
19. Li Y*, et al.* (2004) Size separation of circulatory DNA in maternal plasma permits ready detection of fetal DNA polymorphisms. *Clin Chem* 50(6):1002-1011.
20. O`Sullivan CK, Hahn T, & Drese KS (2010) [DE] IfMM & [ES] URiV WO2010026222 (A1).
21. Bard AJ & Faulkner LR (2001) *Electrochemical methods: Fundamentals and applications* (John Wiley & Sons) 2nd Ed.
22. Masliyah JH & Bhattacharjee S (2006) *Electrokinetic and colloid transport phenomena* (John Wiley & Sons, New Jersey).
23. Israelachvili J (1992) *Intermolecular & surface forces* (Academic Press, Limited, London) 2nd edition Ed.
24. Debye P & Hückel E (1923) The theory of electrolytes. I. Lowering of freezing point and related phenomena. *Physikalische Zeitschrift* 24:185-206.
25. Onsager L (1969) The motions of ions: Principles and concepts. *Science* 166(3911):1359-1364.
26. Booth F (1951) The dielectric constant of water and the saturation effect. *J Chem Phys* 19(4):391-394.
27. Lamm G & Pack GR (1997) Calculation of dielectric constants near polyelectrolytes in solution. *J Phys Chem B* 101(6):959-965.
28. Frank S & Schmickler W (2000) A lattice-gas model for ion pairing at liquid vertical bar liquid interfaces. *J Electroanal Chem* 483(1-2):18-21.
29. Pereira CM, Schmickler W, Silva F, & Sousa MJ (1997) Ion association at liquid-liquid interfaces. *J Electroanal Chem* 436:9-15.
30. Schweighofer K & Benjamin I (1999) Transfer of a tetramethylammonium ion across the water-nitrobenzene interface: Potential of mean force and nonequilibrium dynamics. *J Phys Chem A* 103(49):10274-10279.
31. Jones TB (1995) *Electromechanics of particles* (Cambridge University press, New York) p 263.
32. Meschede D (2003) *Gerthsen Physik* (Springer, Berlin, Heidelberg, New York).
33. Israelachvili J & Pashley R (1982) The hydrophobic interaction is long range, decaying exponentially with distance. *Nature* 300(5890):341-342.
34. Helmholtz H (1853) *Pogg. Ann.* LXXXIX:211.
35. Helmholtz H (1868) Über discontinuierliche Flüssigkeitsbewegungen. *Phil. Mag.* 36:337-346.
36. Chapman DL (1913) Mean-field approaches. Experimentally, both membrane. *Phil. Mag.* 6(25):475.
37. Gouy LG (1910) Sur la compression de la charge electrique a la surface d'un electrolyte. *J. Phys.* 9:457-468.

38. Stern O (1924) Zuer Theorie der electrolytischen Doppelschicht. *Z Electrochem* 30:508.
39. Squires TM & Quake S (2005) Microfluidics: Fluid physics at the nanoliter scale. *Rev Mod Phys* 7(3):977-1026.
40. Attard P (1995) Ion Condensation in the Electric Double Layer and the Corresponding Poisson-Boltzmann Effective Surface Charge. *J Phys Chem* 99:14174-14181.
41. Atkins P & de Paula J (2006) *Physical Chemistry* (Oxford University Press, Oxford).
42. Jin R & Breslauer KJ (1988) Characterization of the minor groove environment in a drug-DNA complex: bisbenzimide bound to the poly[d(AT)].poly[d(AT)]duplex. *Proc Natl Acad Sci U S A* 85(23):8939-8942.
43. Gavryushov S & Zielenkiewicz P (1998) Electrostatic potential of B-DNA: Effect of interionic correlations. *Biophys J* 75(6):2732-2742.
44. Petrov EP, Ohrt T, Winkler RG, & Schwille P (2006) Diffusion and segmental dynamics of double-stranded DNA. *Phys Rev Lett* 97(25):258101.
45. O`Brien RW (1983) The Solution of the Electrokinetic Equations for Colloidal Particles with Thin Double-Layers. *Journal of Colloid and Interface Science* 92(1):204-216.
46. O`Brien RW & Hunter RJ (1981) The electrophoretic mobility of large colloidal particles. *Can J Chem* 59:1878.
47. O`Brien RW & White LR (1978) Electrophoretic mobility of a spherical colloidal particle. *J Chem Soc Faraday Trans 2* 74:1607-1626.
48. Bazant MZ & Squires TM (2004) Induced-charge electrokinetic phenomena: theory and microfluidic applications. *Phys Rev Lett* 92(6):066101.
49. Seibel K, Schöler L, Schäfer H, & Böhm M (2008) A programmable planar electroosmotic micropump for lab-on-a-chip applications. *J Micromech Microeng* 18:1-7.
50. Brask A, Kutter JP, & Bruus H (2005) Long-term stable electroosmotic pump with ion exchange membranes. *Lab Chip* 5(7):730-738.
51. Brask A, Snakenborg D, Kutter JP, & Bruus H (2006) AC electroosmotic pump with bubble-free palladium electrodes and rectifying polymer membrane valves. *Lab Chip* 6(2):280-288.
52. Chen CF*, et al.* (2006) A microfluidic nanoliter mixer with optimized grooved structures driven by capillary pumping. *J. Micromech. Microeng.* 16:1358-1365.
53. Chou HP, Unger MA, & Quake SR (2001) A microfabricated rotary pump. *Biomedical Microdevices* 3(4):323-330.
54. Culbertson CT, Ramsey RS, & Ramsey JM (2000) Electroosmotically induced hydraulic pumping on microchips: differential ion transport. *Anal Chem* 72(10):2285-2291.
55. Darabi J, Ohadi MM, & DeVoe D (2001) An electrohydrodynamic polarization micropump for electronic cooling. *IEEE ASME J Microelectromech Syst* 10(1):98-106.

56. Debesset S, Hayden CJ, Dalton C, Eijkel JC, & Manz A (2004) An AC electroosmotic micropump for circular chromatographic applications. *Lab Chip* 4(4):396-400.
57. Dodge A, Fluri K, Verpoorte E, & de Rooij NF (2001) Electrokinetically driven microfluidic chips with surface-modified chambers for heterogeneous immunoassays. *Anal Chem* 73(14):3400-3409.
58. Gan W*, et al.* (2000) Mechanism of porous core electroosmotic pump flow injection system and its application to determination of chromium(VI) in waste-water. *Talanta* 51:667-675.
59. Laser DJ & Santiago JG (2004) A review of micropumps. *J. Micromech. Microeng.* 14:R35-R64.
60. McKnight TE, Culbertson CT, Jacobson SC, & Ramsey JM (2001) Electroosmotically induced hydraulic pumping with integrated electrodes on microfluidic devices. *Anal Chem* 73(16):4045-4049.
61. Mishchuk NA, Heldal T, Volden T, Auerswald J, & Knapp H (2009) Micropump based on electroosmosis of the second kind. *Electrophoresis* 30(20):3499-3506.
62. Richter A, Plettner A, Hofmann KA, & Sandmaier H (1991) Electrohydrodynamic pumping and flow measurement. *IEEE*, pp 271-276.
63. Zeng S, Chen C-H, Mikkelsen JC, & Santiago JG (2001) Fabrication and characterization of electroosmotic micropumps. *Sensor Actuator B Chem* 79:107-114.
64. Zheng S, Chen C-H, Mikkelsen JC, & Santiago JG (2001) Fabrication and characterization of electroosmotic micropumps. *Sensors and Actuators B* 79:107-114.
65. Chen CH & Santiago JG (2002) A planar electroosmotic micropump. *IEEE ASME J Microelectromech Syst* 11(6):672-683.
66. Takamura Y*, et al.* (2003) Low-voltage electroosmosis pump for stand-alone microfluidics devices. *Electrophoresis* 24:185-192.
67. Verpoorte E (2002) Microfluidic chips for clinical and forensic analysis. *Electrophoresis* 23(5):677-712.
68. Bowling DFJ (1969) Evidence for Electroosmosis Theory of Transport in Phloem. *Biochim Biophys Acta* 183(1):230-&.
69. Griffiths SK & Nilson RH (2005) The efficiency of electrokinetic pumping at a condition of maximum work. *Electrophoresis* 26(2):351-361.
70. Chein RY & Liao JC (2007) Analysis of electrokinetic pumping efficiency in capillary tubes. *Electrophoresis* 28(4):635-643.
71. Peterman MC, Noolandi J, Blumenkranz MS, & Fishman HA (2004) Localized chemical release from an artificial synapse chip. *Proc Natl Acad Sci U S A* 101(27):9951-9954.
72. Conlisk AT (2005) The Debye-Huckel approximation: Its use in describing electroosmotic flow in micro- and nanochannels. *Electrophoresis* 26(10):1896-1912.

73. Chun MS, Lee SY, & Yang SM (2003) Estimation of zeta potential by electrokinetic analysis of ionic fluid flows through a divergent microchannel. *J Colloid Interface Sci* 266(1):120-126.
74. Sternling CV & Scriven LE (1959) Interfacial turbulence : Hydrodynamic instability and the Marangoni effect. *AIChE* 5(4):514-523.
75. Lippmann MG (1875) Relations entre les phénomènes electriques et capillaires. *Ann Chim Phys* 5(11):494-549.
76. Yeo LY & Chang H-C (2005) Static and spontaneous electrowetting. *Mod Phys Lett B* 19(2):549-569.
77. Vallet M, Berge B, & Vovelle L (1996) Electrowetting of water and aqueous solutions on poly(ethylene terephthalate) insulating films. *Polymer* 37(12):2465-2470.
78. Cheng CC, Chang CA, & Yeh JA (2006) Variable focus dielectric liquid droplet lens. *Optics Express* 14(9):4101-4106.
79. Ferre-D'Amare AR (2004) The hairpin ribozyme. *Biopolymers* 73(1):71-78.
80. Kornyshev AA & Wynveena A (2009) The homology recognition well as an innate property of DNA structure. *Proc Natl Acad Sci U S A* 106(12):4683-4688.
81. Stevens MJ (2001) Simple simulations of DNA condensation. *Biophys J* 80(1):130-139.
82. Allison SA, Li Z, Reed D, & Stellwagen NC (2002) Modeling the gel electrophoresis of short duplex DNA by Brownian dynamics: cubic gel lattice with direct interaction. *Electrophoresis* 23(16):2678-2689.
83. Allison S, Chen C, & Stigter D (2001) The length dependence of translational diffusion, free solution electrophoretic mobility, and electrophoretic tether force of rigid rod-like model duplex DNA. *Biophys J* 81:2558-2568.
84. Allison SA & Tran VT (1995) Modeling the electrophoresis of rigid polyions: application to lysozyme. *Biophys J* 68(6):2261-2270.
85. Stellwagen NC, Gelfi C, & Righetti PG (1997) The free solution mobility of DNA. *Biopolymers* 42(6):687-703.
86. Ha SC, Lowenhaupt K, Rich A, Kim YG, & Kim KK (2005) Crystal structure of a junction between B-DNA and Z-DNA reveals two extruded bases. *Nature* 437(7062):1183-1186.
87. de Rosa M*, et al.* (2010) Crystal structure of a junction between two Z-DNA helices. *Proc Natl Acad Sci U S A* 107(20):9088-9092.
88. Mohanty U & Zhao YQ (1996) Polarization of counterions in polyelectrolytes. *Biopolymers* 38(3):377-388.
89. Washizu H & Kikuchi K (2002) Electrical polarizability of polyelectrolytes in salt-free aqueous solution. *J Phys Chem B* 106(43):11329-11342.
90. Washizu H & Kikuchi K (2006) Electric polarizability of DNA in aqueous salt solution. *J Phys Chem B* 110(6):2855-2861.
91. Regtmeier J, Duong TT, Eichhorn R, Anselmetti D, & Ros A (2007) Dielectrophoretic manipulation of DNA: Separation and polarizability. *Anal Chem* 79(10):3925-3932.

92. Tuukkanen S*, et al.* (2007) Trapping of 27 bp-8 kbp DNA and immobilization of thiol-modified DNA using dielectrophoresis. *Nanotechnology* 18(29):-.
93. Hershey AD & Burgi E (1965) Complementary Structure of Interacting Sites at the Ends of Lambda DNA Molecules. *Proc Natl Acad Sci U S A* 53:325-328.
94. Schildkraut CL, Marmur J, & Doty P (1962) Determination of the base composition of deoxyribonucleic acid from its buoyant density in CsCl. *J Mol Biol* 4:430-443.
95. Lu Y, Weers B, & Stellwagen NC (2001) DNA persistence length revisited. *Biopolymers* 61(4):261-275.
96. Hays JB, Magar ME, & Zimm BH (1969) Persistence Length of DNA. *Biopolymers* 8(4):531-&.
97. Garcia de la Torre J, Lopez-Martinez MC, & Tirado MM (1984) Dimensions of short, rodlike macromolecules from translational and rotational diffusion coefficients. Study of the gramicidin dimer. *Biopolymers* 23:611-615.
98. Lu Y & Stellwagen NC (2008) Monovalent cation binding by curved DNA molecules containing variable numbers of a-tracts. *Biophys J* 94(5):1719-1725.
99. Zimm BH (1956) Dynamics of Polymer Molecules in Dilute Solution - Viscoelasticity, Flow Birefringence and Dielectric Loss. *Journal of Chemical Physics* 24(2):269-278.
100. Zimm BH, Roe GM, & Epstein LF (1956) Solution of a Characteristic Value Problem from the Theory of Chain Molecules. *Journal of Chemical Physics* 24(2):279-280.
101. Zimm BH & Bragg JK (1959) Theory of the phase transition between helix and random coil in polypeptide chains. *J Chem Phys* 31:526-531.
102. Quake SR (1994) The Zimm model applied to extended single polymers. *J. Chem. Phys.* 101(5):4307-4311.
103. Quake SR, Babcock H, & Chu S (1997) The dynamics of partially extended singlemolecules of DNA. *Nature* 388:151-154.
104. Stellwagen E & Stellwagen NC (2002) Determining the electrophoretic mobility and translational diffusion coefficients of DNA molecules in free solution. *Electrophoresis* 23(16):2794-2803.
105. Stellwagen E, Lu Y, & Stellwagen NC (2005) Curved DNA molecules migrate anomalously slowly in free solution. *Nucleic Acids Res* 33(14):4425-4432.
106. Porschke D (2007) Unique Physical Signature of DNA Curvature and Its Implications for Structure and Dynamics. *J Phys Chem B* 111(41):12004-12011.
107. Timerbaev AR & Hirokawa T (2006) Recent advances of transient isotachophoresis-capillary electrophoresis in the analysis of small ions from high-conductivity matrices. *Electrophoresis* 27(1):323-340.
108. Wainright A, Nguyen UT, Bjornson T, & Boone TD (2003) Preconcentration and separation of double-stranded DNA fragments by electrophoresis in plastic microfluidic devices. *Electrophoresis* 24(21):3784-3794.
109. Wainright A*, et al.* (2002) Sample pre-concentration by isotachophoresis in microfluidic devices. *J Chromatogr A* 979:69-80.

110. Xu ZQ, Hirokawa T, Nishine T, & Arai A (2003) High-sensitivity capillary gel electrophoretic analysis of DNA fragments on an electrophoresis microchip using electrokinetic injection with transient isotachophoretic preconcentration. *J Chromatogr A* 990(1-2):53-61.

111. Walker PA, 3rd, Morris MD, Burns MA, & Johnson BN (1998) Isotachophoretic separations on a microchip. Normal Raman spectroscopy detection. *Anal Chem* 70(18):3766-3769.

112. Kondratova VN, Serd'uk OI, Shelepov VP, & Lichtenstein AV (2005) Concentration and isolation of DNA from biological fluids by agarose gel isotachophoresis. *Biotechniques* 39:695-699.

113. Hirokawa T, Okamoto H, & Gas B (2003) High-sensitive capillary zone electrophoresis analysis by electrokinetic injection with transient isotachophoretic preconcentration: electrokinetic supercharging. *Electrophoresis* 24(3):498-504.

114. Enlund AM, Schmidt S, & Westerlund D (1998) Detectability improvements in capillary zone electrophoresis by combining single capillary isotachophoretic preconcentration and frequency doubled argon ion laser-induced fluorescence detection. *Electrophoresis* 19(5):707-711.

115. Ma B*, et al.* (2006) Integrated isotachophoretic preconcentration with zone electrophoresis separation on a quartz microchip for UV detection of flavonoids. *Electrophoresis* 27(24):4904-4909.

116. Auriola S, Jääskelainen I, Regina M, & Urtii A (1996) Analysis of oligonucleotides by on-column transient capillary isotachophoresis and capillary electrophoresis in poly(ethylene glycol)-filled columns. *Anal Chem* 68:3907-3911.

117. Liu D*, et al.* (2006) Isotachophoresis preconcentration integrated microfluidic chip for highly sensitive genotyping of the hepatitis B virus. *J Chromatogr B Analyt Technol Biomed Life Sci* 844(1):32-38.

118. Busnel JM*, et al.* (2006) Transient isotachophoresis in carrier ampholyte-based capillary electrophoresis for protein analysis. *Electrophoresis* 27(18):3591-3598.

119. Jeong Y, Choi K, Kang MK, Chun K, & Chung DS (2005) Transient isotachophoresis of highly saline samples using a microchip. *Sensors and Actuators B: Chemical* 104:269-275.

120. Riaz A & Chung DS (2005) Transient isotachophoresis of highly saline trace metals under strong electroosmotic flow conditions. *Electrophoresis* 26(3):668-673.

121. Hahn T, O`Sullivan CK, & Drese KS (2009) Microsystem for field-amplified electrokinetic trapping preconcentration of DNA at poly(ethylene terephthalate) membranes. *Anal Chem* 81(8):2904-2911.

122. Pittman JL*, et al.* (2003) Experimental studies of electroosmotic flow dynamics during sample stacking for capillary electrophoresis. *Anal Chem* 75(14):3531-3538.

123. Zhang C-X & Thormann W (1996) Head-column field-amplified sample stacking in binary system capillary electrophoresis: A robust approach providing over 1000-fold sensitivity enhancement. *Anal Chem* 68:2523-2532.

124. Jung B, Bharadwaj R, & Santiago JG (2003) Thousandfold signal increase using field-amplified sample stacking for on-chip electrophoresis. *Electrophoresis* 24(19-20):3476-3483.
125. Liu S*, et al.* (2000) Automated parallel DNA sequencing on multiple channel microchips. *Proc Natl Acad Sci U S A* 97(10):5369-5374.
126. Hahn T, Drese KS, & O`Sullivan CK (2009) Microsystem for isolation of fetal DNA from maternal plasma by preparative size separation. *Clin Chem* 55:2144-2152.
127. Paegel BM, Emrich CA, Wedemayer GJ, Scherer JR, & Mathies RA (2002) High throughput DNA sequencing with a microfabricated 96-lane capillary array electrophoresis bioprocessor. *Proc Natl Acad Sci U S A* 99(2):574-579.
128. Aborn JH*, et al.* (2005) A 768-lane microfabricated system for high-throughput DNA sequencing. *Lab Chip* 5(6):669-674.
129. Schwartz DC & Cantor CR (1984) Separation of yeast chromosome-sized DNAs by pulsed field gradient gel-electrophoresis. *Cell* 37(1):67-75.
130. Inatomi K, Izuo S, Lee SS, Ohji H, & Shiono S (2003) Electrophoresis of DNA in micro-pillars fabricated in polydimethylsiloxane. *Microelectronic Engineering* 70(1):13-18.
131. Huang LR*, et al.* (2002) A DNA prism for high-speed continuous fractionation of large DNA molecules. *Nat Biotechnol* 20(10):1048-1051.
132. Duke TAJ & Austin RH (1998) Microfabricated sieve for the continuous sorting of macromolecules. *Phys Rev Lett* 80(7):1552-1555.
133. Bakajin O*, et al.* (2001) Separation of 100-kilobase DNA molecules in 10 seconds. *Anal Chem* 73(24):6053-6056.
134. Fu J, Schoch RB, Stevens AL, Tannenbaum SR, & Han J (2007) A patterned anisotropic nanofluidic sieving structure for continuous-flow separation of DNA and proteins. *Nature Nanotechnology* 2(2):121-128.
135. Choi S & Park JK (2007) Continuous hydrophoretic separation and sizing of microparticles using slanted obstacles in a microchannel. *Lab Chip* 7(7):890-897.
136. Han J & Craighead HG (2000) Separation of long DNA molecules in a microfabricated entropic trap array. *Science* 288(5468):1026-1029.
137. Spicer CW*, et al.* (1998) Unexpectedly high concentrations of molecular chlorine in coastal air. *Nature* 394(6691):353-356.
138. Oum KW, Lakin MJ, DeHaan DO, Brauers T, & Finlayson-Pitts BJ (1998) Formation of molecular chlorine from the photolysis of ozone and aqueous sea-salt particles. *Science* 279(5347):74-77.
139. Knipping EM*, et al.* (2000) Experiments and simulations of ion-enhanced interfacial chemistry on aqueous NaCl aerosols. *Science* 288(5464):301-306.
140. Born M (1920) Volumen und Hydratationswärme der Ionen. *Z Phys* 1:45-49.
141. Uhlig HH (1937) The solubilities of gases and surface tension. *J Phys Chem* 41:1215-1226.

142. Markin VS & Volkov AG (1989) The Gibbs free energy of ion transfer between two immiscible liquids. *Electrochimica Acta* 34(2):93-107.
143. Kornyshev AA & Volkov AG (1984) On the evaluation of standard Gibbs energies of ion transfer between two solvents. *J Electroanal Chem* 180:363-381.
144. Still WC, Tempczyk A, Hawley RC, & Hendrickson T (1990) Semianalytical Treatment of Solvation for Molecular Mechanics and Dynamics. *J. Am. Chem. Soc.* 112:6127-6129.
145. Tolman RC (1949) The effect of droplet size on surface tension. *J. Chem. Phys.* 17(3):333-337.
146. Osakai T & Ebina K (1998) Non-Bornian theory of the Gibbs energy of ion transfer between two immiscible liquids. *J Phys Chem B* 102(29):5691-5698.
147. Osakai T, Ogata A, & Ebina K (1997) Hydration of ions in organic solvent and its significance in the Gibbs energy of ion transfer between two immiscible liquids. *Journal of Physical Chemistry B* 101(41):8341-8348.
148. Verwey EJW & Niessen KF (1939) The electrical double layer at the interfaces of two liquids. *Phil Mag* 28(189):435-446.
149. d`Epenoux B, Seta P, Amblard G, & Gavach C (1979) The transfer mechanism of tetraalkylammonium ions across a water-nitrobenzene interface and the structure of the double layer. *J. Electroanal. Chem.* 99:77-84.
150. Gavach C, Seta P, & D`Epenoux B (1977) The double layer and ion adsorption at the interface between two non immiscible solutions Part I. Interfacial tension measurements for the water-nitrobenzene tetraalkylammonium bromide systems. *J Electroanal Chem* 83:225-235.
151. Gros M, Gromb S, & Gavach C (1978) The double layer and ion adsorption at the interfacebetween two non-immiscible solutions Part II. Electrocapillary behaviour of some water-nitrobenzene systems. *J. Electroanal. Chem.* 89:29-36.
152. Girault HH, Schiffrin DJ, & Smith BDV (1982) Drop Image-Processing for Surface and Interfacial-Tension Measurements. *Journal of Electroanalytical Chemistry* 137(2):207-217.
153. Samec Z, Lhotsky A, Janchenova H, & Marecek V (2000) Interfacial tension and impedance measurements of interfaces between two immiscible electrolyte solutions. *Journal of Electroanalytical Chemistry* 483(1-2):47-56.
154. Trojanek A, Lhotsky A, Marecek V, & Samec Z (2004) Limited agreement between the interfacial tension and differential capacity data for the polarised water vertical bar 1,2-dichloroethane interface. *Journal of Electroanalytical Chemistry* 565(2):243-250.
155. Huber T, Pecina O, & Schmickler W (1999) The influence of the ions on the capacity of liquid vertical bar liquid interfaces. *Journal of Electroanalytical Chemistry* 467(1-2):203-206.
156. Hajkova P, Homolka D, Marecek V, Volkov AG, & Samec Z (1985) Measurements of Electric Double-Layer Capacity at the Water Dichloroethane Interface in the Presence of Metal-Porphyrin Complexes. *Sov Electrochem+* 21(2):190-196.
157. Samec Z, Marecek V, & Homolka D (1981) The Double-Layer at the Interface between 2 Immiscible Electrolyte-Solutions .1. Capacity of the Water-

Nitrobenzene Interface. *Journal of Electroanalytical Chemistry* 126(1-3):121-129.

158. Daikhin LI & Urbakh M (2003) Double layer capacitance and a microscopic structure of electrified liquid–liquid interfaces. *J. Electroanal. Chem.* 560:59.
159. Walker DS, Brown MG, McFearin CL, & Richmond GL (2004) Evidence for a Diffuse Interfacial Region at the Dichloroethane/Water Interface. *J Phys Chem B* 108:2111-2114.
160. Luo G*, et al.* (2006) Ion Distributions near a Liquid-Liquid Interface. *Science* 311:216-219.
161. Weissenborn PK & Pugh RJ (1996) Surface tension of aqueous solutions of electrolytes: Relationship with ion hydration, oxygen solubility, and bubble coalescence. *Journal of Colloid and Interface Science* 184(2):550-563.
162. Manciu M & Ruckenstein E (2005) On the interactions of ions with the air/water interface. *Langmuir* 21(24):11312-11319.
163. Pereira CM, Silva F, Sousa MJ, Kontturi K, & Murtomaki L (2001) Capacitance and ionic association at the electrified oil-water interface: the effect of the oil phase composition. *J Electroanal Chem* 509:148-154.
164. Kakiuchi T, Nogushi J, Kotani M, & Senda M (1990) AC polarographic determination of the rate of ion transfer for a series of alkylammonium ions at the nitrobenzene/water interface. *J Electroanal Chem* 296:517-535.
165. Koryta J, Vanysek P, & Brezina M (1977) Electrolysis with Electrolyte Dropping Electrode .2. Basic Properties of System. *J Electroanal Chem* 75(1):211-228.
166. Samec Z (1988) Electrical Double-Layer at the Interface between 2 Immiscible Electrolyte-Solutions. *Chemical Reviews* 88(4):617-632.
167. Kivlehan F, Lanyon YH, & Arrigan DWM (2008) Electrochemical study of insulin at the polarized liquid-liquid interface. *Langmuir* 24(17):9876-9882.
168. Méndez MA, Prudent M, Su B, & Girault HH (2008) Peptide-Phospholipid Complex Formation at Liquid-Liquid Interfaces. *Anal Chem* 80:9499-9507.
169. Trojanek A, Langmaier J, Samcova E, & Samec Z (2007) Counterion binding to protamine polyion at a polarised liquid-liquid interface. *Journal of Electroanalytical Chemistry* 603(2):235-242.
170. Santos HA, Carlsson S, Murtomaki L, & Kontturi K (2007) Effect of gramicidin on phospholipid-modified monolayers and on ion transfer at a liquid-liquid interface. *Chemphyschem* 8(6):913-920.
171. Frank S & Schmickler W (2007) Ion transfer across liquid-liquid interfaces from transition-state theory and stochastic molecular dynamics simulations. *Journal of Electroanalytical Chemistry* 599(2):376-376.
172. Su B, Eugster N, & Girault HH (2005) Simulations of the adsorption of ionic species at polarisable liquid-liquid interfaces. *J Electroanal Chem* 577:187-196.
173. Manciu M & Ruckenstein E (2005) Polarization of water near dipolar surfaces: A simple model for anomalous dielectric behavior. *Langmuir* 21(25):11749-11756.

174. Chang TM & Dang LX (2006) Recent advances in molecular simulations of ion solvation at liquid interfaces. *Chemical Reviews* 106(4):1305-1322.
175. Dang LX & Chang TM (2002) Molecular mechanism of ion binding to the liquid/vapor interface of water. *Journal of Physical Chemistry B* 106(2):235-238.
176. Wick CD & Dang LX (2005) Diffusion at the Liquid-Vapor Interface of an Aqueous Ionic Solution Utilizing a Dual Simulation Technique. *J. Phys. Chem. B* 109:15574-15579.
177. Benjamin I (1997) Molecular structure and dynamics at liquid-liquid interfaces. *Annual Review of Physical Chemistry* 48:407-451.
178. Marrink SJ & Berendsen HJC (1994) Simulation of Water Transport through a Lipid-Membrane. *Journal of Physical Chemistry* 98(15):4155-4168.
179. Manciu M & Ruckenstein E (2006) Ions at the air/water interface. *Journal of Colloid and Interface Science* 304(2):541-544.
180. Zhang YJ & Cremer PS (2006) Interactions between macromolecules and ions: the Hofmeister series. *Current Opinion in Chemical Biology* 10(6):658-663.
181. Helfrich MR, El-Kouedi M, Etherton MR, & Keating CD (2005) Partitioning and assembly of metal particles and their bioconjugates in aqueous two-phase systems. *Langmuir* 21(18):8478-8486.
182. Kirkwood JG & Buff FP (1949) The statistical mechanical theory of surface tension. *J. Chem. Phys.* 17(3):338-343.
183. Onsager L & Samaras NNT (1934) The surface tension of Debye-Hückel electrolytes. *The Journal of Chemical Physics* 2(8):528-536.
184. Wagner C (1924) *Phys. Zeit.* 25:474.
185. Flatté ME, Kornyshev AA, & Urbakh M (2008) Understanding voltage-induced localization of nanoparticles at a liquid–liquid interface. *J Phys Condens Matter* 20:073102.
186. Johans C, Liljeroth P, & Kontturi KS (2002) Electrodeposition at polarisable liquid vertical bar liquid interfaces: The role of interfacial tension on nucleation kinetics. *Physical Chemistry Chemical Physics* 4(6):1067-1071.
187. Bresme F & Quirke N (1999) Nanoparticulates at liquid liquid interfaces. *Physical Chemistry Chemical Physics* 1(9):2149-2155.
188. Amirfazli A & Neumann AW (2004) Status of the three-phase line tension. *Adv Colloid Interface Sci* 110:121-141.
189. Hatti-Kaul Re (2000) *Aqueous two-phase systems: Methods and Protocols* (Humana Press Inc.).
190. Flory PJ (1941) Thermodynamics of high polymer solutions. *J Chem Phys* 9(8):660.
191. Huggins ML (1941) Solutions of long chain compounds. *J Chem Phys* 9(5):440.
192. Walter H, Brooks DE, & Fisher D (1985) *Partitioning in aqueous two-phase systems* (Academic Press, Inc., Orlando, Florida).
193. Albertsson PA (1986) *Partition of cell particles and macromolecules* (John Wiley & Sons, New York).

194. Brooks DE*, et al.* (1984) Electrostatic and electrokinetic potentials in two polymer aqueous phase systems. *J Colloid Interface Sci* 102(1):1-13.

195. Reitherman R, Flanagan SD, & Barondes SH (1973) Electromotive Phenomena in Partition of Erythrocytes in Aqueous Polymer 2 Phase Systems. *Biochim Biophys Acta* 297(2):193-202.

196. Walter H, Johansson G, & Brooks DE (1991) Partitioning in aqueous two-phase systems: recent results. *Anal Biochem* 197(1):1-18.

197. Theos CW & Clark WM (1995) Electroextraction - Two-phase electrophoresis. *Appl Biochem Biotechnol* 54:143-157.

198. Pfennig A & Schwerin A (1995) Analysis of the electrostatic potential difference in aqueous polymer two-phase systems. *Fluid Phase Equilibria* 108:305-315.

199. Herrmann A, Arnold K, & Pratsch L (1985) The Effect of Osmotic-Pressure of Aqueous Peg Solutions on Red Blood-Cells. *Bioscience Reports* 5(8):689-696.

200. Zaslavsky BY*, et al.* (1989) Dielectric Properties of Water in the Coexisting Phases of Aqueous Polymeric Two-phase Systems. *J Chem Soc Faraday Trans 1* 85(1):2857-2865.

201. Pei Y, Wang J, Wu K, Xuan X, & Lu X (2009) Ionic liquid-based aqueous two-phase extraction of selected proteins. *Separation and Purification Technology* 64:288-295.

202. Dreyer S & Kragl U (2008) Ionic liquids for aqueous two-phase extraction and stabilization of enzymes. *Biotechnol Bioeng* 99(6):1416-1424.

203. Luechau F, Ling TC, & Lyddiatt A (2009) Partition of plasmid DNA in polymer–salt aqueous two-phase systems. *Separ Purif Tech* 66:397-404.

204. Foroutan M & Khomami MH (2009) Quaternary (liquid + liquid) equilibria of aqueous two-phase poly (ethylene glycol), poly (DMAM–TBAM), and KH2PO4: Experimental and generalized Flory–Huggins theory. *J. Chem. Thermodynamics* 41:604-609.

205. Sheth SR & Leckband D (1997) Measurements of attractive forces between proteins and end-grafted poly(ethylene glycol) chains. *Proc Natl Acad Sci U S A* 94(16):8399-8404.

206. Käsbauer M, Lasic DD, & Winterhalter M (1997) Polymer induced fusion and leakage of small unilamellar phospholipid vesicles: effect of surface grafted polyethylene-glycol in the presence of free PEG. *Chemistry and Physics of Lipids* 86:153-159.

207. Papahadjopoulos D*, et al.* (1991) Sterically Stabilized Liposomes - Improvements in Pharmacokinetics and Antitumor Therapeutic Efficacy. *Proceedings of the National Academy of Sciences of the United States of America* 88(24):11460-11464.

208. Lerman LS (1971) A transition to a compact form of DNA in polymer solutions. *Proc Natl Acad Sci U S A* 68(8):1886-1890.

209. Zinchenko AA & Yoshikawa K (2005) Na+ shows a markedly higher potential than K+ in DNA compaction in a crowded environment. *Biophysical Journal* 88(6):4118-4123.

210. Frerix A*, et al.* (2006) Exploitation of the coil-globule plasmid DNA transition induced by small changes in temperature, pH salt, and poly(ethylene glycol) compositions for directed partitioning in aqueous two-phase systems. *Langmuir* 22(9):4282-4290.
211. Pastre D*, et al.* (2007) Atomic force microscopy imaging of DNA under macromolecular crowding conditions. *Biomacromolecules* 8(12):3712-3717.
212. Kombrabail MH & Krishnamoorthy G (2005) Fluorescence dynamics of DNA condensed by the molecular crowding agent poly(ethylene glycol). *Journal of Fluorescence* 15(5):741-747.
213. Israelachvili J (1997) The different faces of poly(ethylene glycol). *Proc Natl Acad Sci U S A* 94(16):8378-8379.
214. Münchow G, Schönfeld F, Hardt S, & Graf K (2008) Protein diffusion across the interface in aqueous two-phase systems. *Langmuir* 24(16):8547-8553.
215. Diamond AD & Hsu JT (1989) Fundamental-Studies of Biomolecule Partitioning in Aqueous 2-Phase Systems. *Biotechnology and Bioengineering* 34(7):1000-1014.
216. Zaslavsky BY, Miheeva LM, Gasanova GZ, & Mahmudov AU (1987) Effect of polymer composition on the relative hydrophobicity of the phases of the biphasic system aqueous dextran-poly(ethylene glycol). *Journal of Chromatography* 403:123-130.
217. Neu B & Meiselman HJ (2002) Depletion-mediated red blood cell aggregation in polymer solutions. *Biophys J* 83(5):2482-2490.
218. Lee H, Venable RM, MacKerell AD, & Pastor RW (2008) Molecular dynamics studies of polyethylene oxide and polyethylene glycol: Hydrodynamic radius and shape anisotropy. *Biophysical Journal* 95(4):1590-1599.
219. de Belder AN (2003) *Dextran* (Amersham Biosciences, Uppsala) p 64.
220. Gekko K (1980) Solution Properties of Dextran and Its Ionic Derivatives. *Abstracts of Papers of the American Chemical Society* 179(Mar):55-Carb.
221. Bremner I, Cox JSG, & Moss GF (1969) Structural Studies on Iron-Dextran - Characterisation of an Alkali-Degraded Dextran Suitable for Use in Production of Parenteral Iron-Dextran Complexes. *Carbohydrate Research* 11(1):77-&.
222. Cox JSG, Rutherfo.D, Marshall PR, Kenndy GR, & King J (1972) Structure of an Iron-Dextran Complex. *Journal of Pharmacy and Pharmacology* 24(7):513-&.
223. Ricketts CR, Cox JSG, Fitzmaur.C, & Moss GF (1965) Iron Dextran Complex. *Nature* 208(5007):237-&.
224. Foster AB (1957) Ionophoresis of carbohydrates. Part V. Reaction of the methyl fructofuranosides and fructopyranosides, and of related compounds, with borate ions. *Journal of the Chemical Society* (MAR):1395-1397.
225. Scandola M, Ceccorulli G, & Pizzoli M (1991) Molecular motions of polysaccharides in the solid state: dextran, pullulan and amylose. *Int J Biol Macromol* 13(4):254-260.
226. Koralewski M, Reinholz F, Karon J, & Waraczewski K (2007) Optical and magnetooptical properties of clinical dextrans. *Acta Physica Polonica A* 112(5):1119-1124.

227. da Costa RF, Bettega MH, Varella MT, & Lima MA (2010) Electron collisions with alpha-D-glucose and beta-D-glucose monomers. *J Chem Phys* 132(12):124309.

228. Montès H & Cavaillé JY (1999) Secondary dielectric relaxations in dried amorphous cellulose and dextran. *Polymer* 40:2649-2657.

229. Nishinari K, Shibuya N, & Kainuma K (1985) Dielectric relaxation in solid dextran and pullulan. *Makromol. Chem.* 186:433-438.

230. Kaminski K*, et al.* (2008) Dielectric Studies on Mobility of the Glycosidic Linkage in Seven Disaccharides. *J Phys Chem* 112:12816-12823.

231. Kaminski K*, et al.* (2009) Identifying the Origins of Two Secondary Relaxations in Polysaccharides. *J Phys Chem* 113:10088-10096.

232. Schartel B, Wendling J, & Wendorff JH (1996) Cellulose/Poly(vinyl alcohol) Blends. 1. Influence of Miscibility and Water Content on Relaxations. *Macromolecules* 29:1521-1527.

233. McBrierty VJ, Keely CM, Coyle FM, Xu H, & Vij JK (1996) Hydration and plasticization effects in cellulose acetate: molecular motion and relaxation. *Faraday Discussions* 103:255-268.

234. Ryabov YE, Feldman Y, Shinyashiki N, & Yagihara S (2002) The symmetric broadening of the water relaxation peak in polymer-water mixtures and its relationship to the hydrophilic and hydrophobic properties of polymers. *J Chem Phys* 116(19):8610-8615.

235. Sudo S, Shinyashiki N, Kitsuki Y, & Yagihara S (2002) Dielectric Relaxation Time and Relaxation Time Distribution of Alcohol-Water Mixtures. *J Phys Chem A* 106:458-464.

236. Sudo S, Shinyashiki N, & Yagihara S (2001) The dielectric relaxation of supercooled ethyleneglycol-water mixtures. *Journal of Molecular Liquids* 90:113-120.

237. Shinyashiki N, Sudo S, Abe W, & Yagihara S (1998) Shape of dielectric relaxation curves of ethylene glycol oligomer–water mixtures. *Journal of Chemical Physics* 109(22):9843-9847.

238. Shinyashiki N, Matsumura Y, Mashimo S, & Yagihara S (1996) Dielectric study on coupling constant of lower critical solution of poly(vinylmethylether) in water. *J Chem Phys* 104(17):6877-6880.

239. Williams G & Watts DC (1970) Non-symmetrical dielectric relaxation behaviour arising from a simple empirical decay function.

240. Shinyashiki N, Matsumura Y, Miura N, Yagihara S, & Mashimo S (1994) Dielectric Study of Water Structure in Polymer Solution. *J Phys Chem* 98:13612-13615.

241. Mashimo S, Miura N, Shinyashiki N, & Ota T (1993) Dielectric Study on Molecular Motions of Poly(glutamic acid) in Aqueous Solution over a Frequency Range of 10(5)-10(10) Hz. *Macromolecules* 26:6859-6863.

242. Shinyashiki N, Asaka N, & Mashimo S (1990) Dielectric study on dynamics of water in polymer matrix using a frequency range 10(6)-10(10) Hz. *J Chem Phys* 93(1):760-764.

243. Rendell RW & Ngai KL (1987) Molecular Weight and Concentration Dependences of the Terminal Relaxation Time and Viscosity of Entangled Polymer Solutions. *Macromolecules* 20(9):2250-2256.

244. Qin Q, Doen H, & McKenna GB (2009) Mechanical Spectral Hole Burning in Polymer Solutions. *Journal of Polymer Science Part B: Polymer Physics* 47:2047-2062.

245. Ngai KL & Rendell RW (1987) Effects of Coupling on Polymer Chain Dynamics Probed Dielectrically: Precursor to Entanglement. *Macromolecules* 20:1066-1069.

246. Ngai KL & Phillies GDJ (1996) Coupling model analysis of polymer dynamics in solution: Probe diffusion and viscosity. *J Chem Phys* 105(18):8385-8397.

247. Ngai KL, Rendell RW, & Plazek DJ (1990) Couplings between the cooperatively rearranging regions of the Adam-Gibbs theory of relaxations in glass-forming liquids. *J Chem Phys* 94(4):3018-3029.

248. Lindsey CP & Patterson GD (1980) Detailed comparison of the Williams-Watts and Cole-Davidson functions. *J Chem Phys* 73(7):3348-3357.

249. Naito S, Hoshi M, & Mashimo S (1997) In Vivo Dielectric Analysis of Free Water Content of Biomaterials by Time Domain Reflectometry. *Analytical biochemistry* 251:163-172.

250. Mashimo S (1977) Effect of diluent on dielectric relaxation time of polymers. *J Chem Phys* 67(6):2651-2658.

251. Miura N, Shinyashiki N, & Mashimo S (1992) Dielectric relaxation of the Kohlrausch-type in aqueous polymer solution. *J Chem Phys* 97(11):8722-8726.

252. Murade CU, Subramaniam V, Otto C, & Bennink ML (2010) Force spectroscopy and fluorescence microscopy of dsDNA-YOYO-1 complexes: implications for the structure of dsDNA in the overstretching region. *Nucleic Acids Res* 38(10):3423-3431.

253. Münchow G (2009) Two-phase electrophoresis of biomolecules. Doctoral Dissertation (TU-Darmstadt, Darmstadt).

254. Naimushin AN, Quach N, Fujimoto BS, & Schurr JM (2001) Effect of polyethylene glycol on the supercoiling free energy of DNA. *Biopolymers* 58(2):204-217.

255. Kleideiter G & Nordmeier E (1999) Poly(ethylene glycol)-induced DNA condensation in aqueous/methanol containing low-molecular-weight electrolyte solutions Part I. Theoretical considerations. *Polymer* 40(14):4013-4023.

256. Kleideiter G & Nordmeier E (1999) Poly(ethylene glycol)-induced DNA condensation in aqueous/methanol containing low-molecular-weight electrolyte solutions Part II. Comparison between experiment and theory. *Polymer* 40(14):4025-4033.

257. Neu B & Meiselman J (2001) Sedimentation and Electrophoretic Mobility Behavior of Human Red Blood Cells in Various Dextran Solutions. *Langmuir* 17:7973-7975.

258. Krabi A, Allan G, Donath E, & Vincent B (1997) Depletion of dextran and PEO for latex particles with "hairy layers": An electrophoretic study. *Colloids and Surfaces a-Physicochemical and Engineering Aspects* 122(1-3):33-42.

259. Donath E, Walther D, Krabi A, Allan GC, & Vincent B (1996) A new relaxation effect with polymer depletion layers. *Langmuir* 12(26):6263-6269.

260. Donath E, Krabi A, Allan G, & Vincent B (1996) A study of polymer depletion layers by electrophoresis: The influence of viscosity profiles and the nonlinearity of the Poisson-Boltzmann equation. *Langmuir* 12(14):3425-3430.

261. Donath E*, et al.* (1997) Stokes friction coefficient of spherical particles in the presence of polymer depletion layers - Analytical and numerical calculations, comparison with experimental data. *J Chem Soc Faraday T* 93(1):115-119.

262. Raghavarao KSMS, Stewart RM, Rudge SR, & Todd P (1998) Electrokinetic demixing of aqueous two-phase systems. 3. Drop electrophoretic mobilities and demixing rates. *Biotechnol Prog* 14(6):922-930.

263. Raghavarao KSMS, Stewart RM, & Todd P (1990) Electrokinetic demixing of two-phase aqueous polymer systems I. Separation rates of polyethylene glycol-dextran mixtures. *Separation Science and Technology* 25(9-10):985-996.

264. Raghavarao KSMS, Stewart RM, & Todd P (1991) Electrokinetic demixing of two-phase aqueous polymer systems II. Separation rates of polyethylene glycol-maltodextrin mixtures. *Separation Science and Technology* 26(2):257-267.

265. Baygents JC & Saville DA (1991) Electrophoresis of Drops and Bubbles. *J Chem Soc Faraday T* 87(12):1883-1898.

266. Ohshima H, Healy TW, & White LR (1984) Electrokinetic Phenomena in a Dilute Suspension of Charged Mercury Drops. *Journal of the Chemical Society-Faraday Transactions Ii* 80:1643-1667.

267. Kirby BJ & Hasselbrink EF (2004) Zeta potential of microfluidic substrates: 2. Data for polymers. *Electrophoresis* 25:203-213.

268. Nespolo SA, Bevan MA, Chan DYC, Grieser F, & Stevens GW (2001) Hydrodynamic and Electrokinetic Properties of Decane Droplets in Aqueous Sodium Dodecyl Sulfate Solutions. *Langmuir* 17:7210-7218.

269. Nagaraj N, Chethana S, & Raghavarao KS (2005) Electrokinetic demixing of aqueous two-phase polymer/salt systems. *Electrophoresis* 26(1):10-17.

270. Dale SEC & Unwin PR (2008) Polarised liquid/liquid micro-interfaces move during charge transfer. *Electrochemistry Communications* 10(5):723-726.

271. Flatté ME, Kornyshev AA, & Urbakh M (2008) Giant Stark effect in quantum dots at liquid/liquid interfaces: A new option for tunable optical filters. *Proc Natl Acad Sci U S A* 105(47):18212-18214.

272. Empedocles SA & Bawendi MG (1997) Quantum-confined stark effect in single CdSe nanocrystallite quantum dots. *Science* 278(5346):2114-2117.

273. Kirby BJ & Hasselbrink EF, Jr. (2004) Zeta potential of microfluidic substrates: 1. Theory, experimental techniques, and effects on separations. *Electrophoresis* 25(2):187-202.

274. Lif T, Frick G, & Albertsson PA (1961) Fractionation of Nucleic Acids in Aqueous Polymer 2-Phase Systems. *J Mol Biol* 3(6):727-&.

275. Kovacic RT & Vanholde KE (1977) Sedimentation of Homogeneous Double-Strand DNA-Molecules. *Biochemistry* 16(7):1490-1498.

276. Studier FW (1965) Sedimentation Studies of Size and Shape of DNA. *Journal of Molecular Biology* 11(2):373-&.

277. Gomes GA, Azevedo AM, Aires-Barros MR, & Prazeres DMF (2009) Purification of plasmid DNA with aqueous two phase systems of PEG 600 and sodium citrate/ammonium sulfate. *Separ Purif Tech* 65:22-30.

278. Kendall D, Booth AJ, Levy MS, & Lye GJ (2001) Separation of supercoiled and open-circular plasmid DNA by liquid-liquid counter-current chromatography. *Biotechnology Letters* 23(8):613-619.

279. Kimura K & Kobayashi H (1996) RNA partitioning accompanied by adsorption: High-molecular-mass RNA adsorbed at the interface like a particle. *Journal of Chromatography B-Biomedical Applications* 680(1-2):213-219.

280. Albertsson PA (1961) Partition studies on nucleic acids I. Influence of electrolytes, polymer concentration and nucleic acid conformation on the partition in the dextran-polyethylene glycol system. *Biochimica et Biophysica Acta* 103:1-12.

281. Anisimov MA (2007) Divergence of Tolman's Length for a Droplet near the Critical Point. *Phys Rev Lett* 98:035702-035701-035702-035703.

282. Levine ML, Cabezas H, Jr., & Bier M (1992) Transport of solutes across aqueous phase interfaces by electrophoresis. Mathematical modeling. *Journal of Chromatography* 607(1):113-118.

283. Bresme F & Oettel M (2007) Nanoparticles at fluid interfaces. *J Phys Condens Matter* 19:1-33.

284. Nikolaides MG*, et al.* (2002) Electric-field-induced capillary attraction between like-charged particles at liquid interfaces. *Nature* 420(6913):299-301.

285. Kramers A (1940) Brownian motion in a field of force and the diffusion model of chemical reactions. *Physica* 7:284-304.

286. Bamberger S, Seaman GVF, Brown JA, & Brooks DE (1984) The partition of sodium phosphate and sodium chloride in aqueous dextran poly(ethylene glycol) two-phase systems. *Journal of Colloid and Interface Science* 99(1):187-193.

287. Lueth CA & Shaqfeh ESG (2009) Experimental and Numerical Studies of Tethered DNA Shear Dynamics in the Flow-Gradient Plane. *Macromolecules* 42(22):9170-9182.

288. Chan EY*, et al.* (2004) DNA mapping using microfluidic stretching and single-molecule detection of fluorescent site-specific tags. *Genome Res* 14(6):1137-1146.

289. Krishnan M, Monch I, & Schwille P (2007) Spontaneous stretching of DNA in a two-dimensional nanoslit. *Nano Lett* 7(5):1270-1275.

290. Krishnan M, Petrasek Z, Monch I, & Schwille P (2008) Electrostatic self-assembly of charged colloids and macromolecules in a fluidic nanoslit. *Small* 4(11):1900-1906.

291. Tuukkanen S*, et al.* (2005) Dielectrophoresis as a tool for nanoscale DNA manipulation. *International Journal of Nanotechnology* 2(3):280-291.

292. Germishuizen WA*, et al.* (2003) Selective dielectrophoretic manipulation of surface-immobilized DNA molecules. *Nanotechnology* 14(8):896-902.

293. Mannion JT, Reccius CH, Cross JD, & Craighead HG (2006) Conformational analysis of single DNA molecules undergoing entropically induced motion in nanochannels. *Biophys J* 90(12):4538-4545.

294. Stigter D (2002) Wall effects on DNA stretch and relaxation. *Biophys Chem* 101-102:447-459.

295. Ferree S & Blanch HW (2003) Electrokinetic stretching of tethered DNA. *Biophys J* 85(4):2539-2546.

296. Akerman B & Tuite E (1996) Single- and double-strand photocleavage of DNA by YO, YOYO and TOTO. *Nucleic Acids Res* 24(6):1080-1090.

297. Breadmore MC*, et al.* (2002) Towards a microchip-based chromatographic platform. Part 1: Evaluation of sol-gel phases for capillary electrochromatography. *Electrophoresis* 23(20):3487-3495.

298. Breadmore MC*, et al.* (2003) Microchip-based purification of DNA from biological samples. *Anal Chem* 75(8):1880-1886.

299. Dhopeshwarkar R, Crooks RM, Hlushkou D, & Tallarek U (2008) Transient effects on microchannel electrokinetic filtering with an ion-permselective membrane. *Anal Chem* 80(4):1039-1048.

300. Hlushkou D, Dhopeshwarkar R, Crooks RM, & Tallarek U (2008) The influence of membrane ion-permselectivity on electrokinetic concentration enrichment in membrane-based preconcentration units. *Lab Chip* 8:1153-1162.

301. Jung B, Bharadwaj R, & Santiago JG (2006) On-chip millionfold sample stacking using transient isotachophoresis. *Anal Chem* 78:2319-2327.

302. Yoza B, Arakaki A, Maruyama K, Takeyama H, & Matsunaga T (2003) Fully automated DNA extraction from blood using magnetic particles modified with a hyperbranched polyamidoamine dendrimer. *J Biosci Bioeng* 95(1):21-26.

303. Yoza B, Arakaki A, & Matsunaga T (2003) DNA extraction using bacterial magnetic particles modified with hyperbranched polyamidoamine dendrimer. *J Biotechnol* 101(3):219-228.

304. Yossifon G, Chang YC, & Chang HC (2009) Rectification, gating voltage, and interchannel communication of nanoslot arrays due to asymmetric entrance space charge polarization. *Phys Rev Lett* 103(15):154502.

305. Yossifon G, Mushenheim P, Chang YC, & Chang HC (2009) Nonlinear current-voltage characteristics of nanochannels. *Phys Rev E Stat Nonlin Soft Matter Phys* 79(4 Pt 2):046305.

306. Breadmore MC & Quirino JP (2008) 100 000-Fold Concentration of Anions in Capillary Zone Electrophoresis Using Electroosmotic Flow Controlled Counterflow Isotachophoretic Stacking under Field Amplified Conditions. *Anal Chem* in press.

307. Yoza B, Matsumoto M, & Matsunaga T (2002) DNA extraction using modified bacterial magnetic particles in the presence of amino silane compound. *J Biotechnol* 94:217-224.

308. Vuosku J*, et al.* (2004) Does extraction of DNA and RNA by magnetic fishing work for diverse plant species? *Mol Biotechnol* 27(3):209-215.

309. Dai J, Ito T, Sun L, & Crooks RM (2003) Electrokinetic trapping and concentration enrichment of DNA in a microfluidic channel. *J Am Chem Soc* 125(43):13026-13027.

310. Wang YC, Stevens AL, & Han J (2005) Million-fold preconcentration of proteins and peptides by nanofluidic filter. *Anal Chem* 77(14):4293-4299.

311. Lichtenberg J, de Rooij NF, & Verpoorte E (2002) Sample pretreatment on microfabricated devices. *Talanta* 56:233-266.

312. Long Z, Liu D, Ye N, Qin J, & Lin B (2006) Integration of nanoporous membranes for sample filtration/preconcentration in microchip electrophoresis. *Electrophoresis* 27(24):4927-4934.

313. Wang Y-C, Tsau CH, Burg TP, Manalis S, & Han J (2005) Efficient biomolecule pre-concentration by nanofilter triggered electrokinetic trapping. *Proceedings of MicroTAS* 9:238-240.

314. Jellema LC, Mey T, Koster S, & Verpoorte E (2009) Charge-based particle separation in microfluidic devices using combined hydrodynamic and electrokinetic effects. *Lab on a Chip* 9(13):1914-1925.

315. Hatch AV, Herr AE, Throckmorton DJ, Brennan JS, & Singh AK (2006) Integrated preconcentration SDS-PAGE of proteins in microchips using photopatterned cross-linked polyacrylamide gels. *Anal Chem* 78(14):4976-4984.

316. Kim SJ, Wang YC, Lee JH, Jang H, & Han J (2007) Concentration polarization and nonlinear electrokinetic flow near a nanofluidic channel. *Phys Rev Lett* 99(4):044501.

317. Leinweber FC & Tallarek U (2005) Concentration polarization-based nonlinear electrokinetics in porous media: induced-charge electroosmosis. *J Phys Chem B* 109(46):21481-21485.

318. Tallarek U, Leinweber FC, & Nischang I (2005) Perspective on concentration polarization effects in electrochromatographic separations. *Electrophoresis* 26(2):391-404.

319. Leinweber FC & Tallarek U (2004) Nonequilibrium electrokinetic effects in beds of ion-permselective particles. *Langmuir* 20(26):11637-11648.

320. Kang KH & Li D (2005) Force acting on a dielectric particle in a concentration gradient by ionic concentration polarization under an externally applied DC electric field. *J Colloid Interface Sci* 286(2):792-806.

321. Khair AS & Squires TM (2008) Fundamental aspects of concentration polarization arising from nonuniform electrokinetic transport (vol 20, art no 087102, 2008). *Physics of Fluids* 20(12):087102.

322. Yossifon G, Frankel I, & Miloh T (2009) Macro-scale description of transient electro-kinetic phenomena over polarizable dielectric solids. *J. Fluid Mech.* 620:241-262.

323. Astorga-Wells J, Vollmer S, Bergman T, & Jornvall H (2007) Formation of stable stacking zones in a flow stream for sample immobilization in microfluidic systems. *Anal Chem* 79(3):1057-1063.

324. Hsieh MM, Tseng WL, & Chang HT (2000) On-column preconcentration and separation of DNA fragments using polymer solutions in the presence of electroosmotic flow. *Electrophoresis* 21(14):2904-2910.

325. Kuo IT, Chiu TC, & Chang HT (2003) On-column concentration and separation of double-stranded DNA by gradient capillary electrophoresis. *Electrophoresis* 24(19-20):3339-3347.

326. Shihabi ZK (2000) Stacking in capillary zone electrophoresis. *J Chromatogr A* 902(1):107-117.

327. Goet G, Baier T, & Hardt S (2009) Micro contactor based on isotachophoretic sample transport. *Lab on a Chip* 9(24):3586-3593.

328. Rubinstein I & Shtilman L (1979) Volatge against current curves of cation-exchange membranes. *J. Chem. Soc., Faraday Trans. 2* 75:231-246.

329. Zangle TA, Mani A, & Santiago JG (2007) Novel device for electrophoretic focussing and separation at a microchannel-nanochannel interface. *Proc. MicroTAS* 11:1204-1206.

330. Zhou K, Kovarik ML, & Jacobson SC (2008) Surface-charge induced ion depletion and sample stacking near single nanopores in microfluidic devices. *J Am Chem Soc* 130(27):8614-8616.

331. Kim SM, Burns MA, & Hasselbrink EF (2006) Electrokinetic protein preconcentration using a simple glass/poly(dimethylsiloxane) microfluidic chip. *Anal Chem* 78(14):4779-4785.

332. Chang H-C & Yossifon G (2009) Understanding electrokinetics at the nanoscale: A perspective. *Biomicrofluidics* 3:012001-012001-012001-012014.

333. Abramoff MD, Magelhaes PJ, & Ram SJ (2004) Image processing with ImageJ. *Biophotonics International* 11:36-42.

334. Fan HC, Blumenfeld YJ, Chitkara U, Hudgins L, & Quake SR (2010) Analysis of the size distributions of fetal and maternal cell-free DNA by paired-end sequencing. *Clin Chem* 56(8):1279-1286.

335. Saiki RK*, et al.* (1985) Enzymatic amplification of beta-globin genomic sequences and restriction site analysis for diagnosis of sickle cell anemia. *Science* 230(4732):1350-1354.

# Symbols and abbreviations

## Symbols

| | |
|---|---|
| $A$ | Surface area |
| $a$ | Radius |
| $a_i$ | Activity of an ion |
| $b$ | Segment distance, height |
| $C$ | Capacitance |
| $C_d$ | Differential capacitance |
| $C_H$ | Capacitance of the Stern layer |
| $C_D$ | Capacitance of the diffuse layer |
| $c$ | Concentration |
| $c_i$ | Concentration of ion species $i$ |
| $D_i$ | Diffusion coefficient of species $i$ |
| $D_r$ | Rotational diffusion constant |
| $D_t$ | Translational diffusion constant |
| $d$ | Displacement, length scale |
| $E^{ext}$ | Externally applied electric field |
| $e$ | Elementary charge |
| $F$ | Faraday constant |
| $\Delta F$ | Energy barrier |
| $F_{dep}$ | Dielectrophoretic force |
| $G_m$ | Gibbs free energy of mixing |
| $\Delta G_t$ | Gibbs free energy of transfer (difference in solvation) |
| $\Delta G_{Born}$ | Born energy |
| $\Delta G_{ne}$ | Solvophobic part of the Gibbs free energy of transfer |
| $g$ | Gravity |
| $H_m$ | Enthalpy of mixing |
| $I$ | Ionic strength or current |
| $I_{max}$ | Maximal discharge current |
| $i$ | Ion species |
| $J_i$ | Ion flux of species $i$ |
| $j$ | Imaginary unit |
| $k_B$ | Boltzman constant |
| $l$ | Length scale |
| $N$ | Number of ion species |
| $N_A$ | Avogadro constant |
| $n_i$ | Ionic number concentration |
| $n_{i\infty}$ | Ionic number concentration in the bulk |
| $p$ | Pressure |
| $p_m$ | Dipole moment |
| $q$ | Charge |
| $R$ | Gas constant |
| $r$ | Length scale |
| $r_g$ | Radius of gyration |
| $S_m$ | Entropy of mixing |
| $T$ | Absolute temperature |
| $t$ | Time |
| $u$ | Velocity |
| $\mathbf{u}$ | Velocity vector |
| $u_{eo}$ | Velocity of the electroosmotic flow |
| $u_p$ | Velocity of a pressure driven flow |
| $u_{hydro}$ | Velocity of a hydrodynamic flow |
| $V$ | Volume |
| $V^{LJ}$ | Lennard-Jones potential |
| $v$ | A symbol, e.g. Fluid velocity |
| $\mathbf{v}$ | Vector function |
| $w$ | Energy |
| x | Distance |
| $x_1$ | Stern plane |
| $x_2$ | Shear plane |
| z | Charge number |
| $z_i$ | Charge number of ion species $i$ |
| $\Gamma_i$ | Surface excess |
| $\gamma$ | Surface tension |
| $\gamma_{1,2}$ | Surface tension between medium 1 and 2 |
| $\gamma_c$ | Volumetric correction factor |

| | |
|---|---|
| $\gamma_i$ | Activity coefficient |
| $\delta$ | Correction factor |
| $\varepsilon$ | Depth of the potential well in the LJ potential |
| $\varepsilon_0$ | Permittivity of free space |
| $\varepsilon_r$ | Relative permittivity |
| $\zeta$ | Zeta potential |
| $\eta$ | Dynamic viscosity |
| $\theta$ | Angle |
| $\lambda_B$ | Bjerrum length |
| $\lambda_D$ | Debye length |
| $\mu$ | Dynamic viscosity |
| $\overline{\mu}_i$ | Chemical potential of an ion ($i$) |
| $\overline{\mu}_i^0$ | Standard chemical potential of $i$ |
| $\mu_e$ | Electrophoretic mobility |
| $\nu$ | Correction factor |
| $\pi$ | Ratio of the circumference to diameter |
| $\sigma_f$ | Charge density of the fluid |
| $\sigma_s$ | Charge density of the substrate |
| $\sigma$ | Conductivity |
| $\sigma_p$ | Conductivity of the particle |
| $\sigma_m$ | Conductivity of the medium |
| $\tau$ | Time constant |
| $\tau_b$ | Escape time |
| $\varphi$ | Potential |
| $\varphi_s$ | Surface potential |
| $\varphi_d$ | Potential at the Stern plane |
| $\varphi_P$ | Dipole potential |

**Abbreviations**

| | |
|---|---|
| AC | Alternating current |
| ATPS | Aqueous two-phase system |
| A.U. | Arbitrary units |
| CE | Capillary electrophoresis |
| DC | Direct current |
| DNA | Desoxyribonucleic acid |
| dsDNA | double-stranded DNA |
| EDL | Electric double layer |
| EKT | Electrokinetic trapping |
| EOF | Electroosmotic flow |
| $EOF_2$ | Electroosmosis of second kind |
| FASS | Field-amplified sample stacking |
| HEPES | 4-(2-Hydroxyethyl)piperazine-1-ethanesulfonic acid |
| ITIES | Interface of two immiscible electrolyte solutions |
| ITP | Isotachophoresis |
| IVD | In-vitro diagnostic device |
| LE | Leading electrolyte |
| *LEP* | Leptin, gene |
| LJ | Lennard-Jones |
| MOPS | 3-(N-Morpholino) propanesulfonic acid |
| NC | Negative control |
| PC | Positive control |
| PCR | Polymerase chain reaction |
| PEG | Poly(ethylene glycol) |
| PET | Poly(ethylene terephtalate) |
| PMMA | Poly(methyl methacrylate) |
| REV | Reference element of volume |
| RNA | Ribonucleic acid |
| *SRY* | Sex determining region Y, gene |
| ssDNA | Single-stranded DNA |
| TE | Terminating electrolyte |
| Tris | Tris(hydroxymethyl) aminomethane |
| λ-DNA | DNA of the Lambda phage |
| µTAS | Micro total analysis systems |

## Acknowledgements

I owe my deepest gratitude to my supervisor, Steffen Hardt, whose passion for science, critical comments, guidance and support enabled me to achieve various results for this thesis. Certainly I appreciate his frequent availability for scientific discussions. I thank also Ciara K. O`Sullivan and Klaus S. Drese for their great support and supervision during my stay at Universitat Rovira i Virgili (Tarragona, Spain) and Institut für Mikrotechnik Mainz (Mainz, Germany). Nico van der Vegt is gratefully acknowledged to act as co-referee for this extensive documentation.

Beside, there have been many scientists and international experts to be acknowledged. I thank Götz Münchow for exchanging scientific ideas, which enabled me to grow in the field of microfluidics. Friedhelm Schönfeld and Tobias Baier I thank for helpful discussions concerning physical issues and Ranjan Ganguly for his support and helpful discussions at my time in Hannover. I am grateful to Jörg Strutwolf and Noemi Laboria-Viñuelas giving me a fundamental understanding of electrochemistry.

It is also a pleasure to thank those who made this thesis possible with their technical assistance, especially Andreas Kurz for labview assistance, José Pinzon for graphic design support, Ashok Sinha for some language advisory and Natalya Pertaya for sharing her experience in optical setups. I am grateful to Anika Kohlstedt and Christine Ruffert for processing SU8 photolithography, to Carsten Zeilinger for access to his laboratory facilities, and I thank Aicha at Soussan and Ellen van der Schoot for providing fetal DNA samples.

I am grateful for funding to pursue research being financed from Universitat Rovira i Virgili (Chapter 11-14) and Deutsche Forschungsgemeinschaft (Chapter 1-10).

Alongside, I thank my family, friends and colleagues for establishing a motivating environment.

# Curriculum Vitae and publications

| | |
|---|---|
| Name: | Thomas Hahn |
| Birth: | 11.06.1978 in Spremberg, Germany |

## Education

| | |
|---|---|
| 2006- 2011 | PhD-studies, Mechanical Eng., TU-Darmstadt, Germany |
| 1999-2005 | **Diploma in biology** at Martin-Luther-Universität Halle/Wittenberg, Germany |
| 1991-1998 | **Sec. School**, Strittmatter-Gymnasium Spremberg |
| 1985-1991 | P**rimary school**, Spremberg |

## Working experience

| | |
|---|---|
| since 2009 | **Research associate** at Center of Smart Interfaces, Mechanical Engineering, TU-Darmstadt, Germany |
| 2008-2009 | **Research associate** at Mechanical Engineering, Leibniz-Universität Hannover, Germany |
| 2006-2008 | **Fellow** of FP6/SAFE-network o. E., at Chemical Engineering Department Universitat Rovira i Virgili, Tarragona, Spain; and visiting scientist at Institut für Mikrotechnik Mainz GmbH, Germany |
| 2005 | **Science technician** at Christchurch Polytechnic Institute of Technology (CPIT), Christchurch, New Zealand |
| 2004-2005 | **Undergraduate employee** at Leibniz-Institut für Pflanzengenetik und Kulturpflanzenforschung (IPK), Gatersleben, Germany |
| 1998-1999 | **Civil service**, Spremberg |

## List of publications

T. Hahn, K. Tag, K. Riedel, S. Uhlig, K. Baronian, G. Gellissen and G. Kunze, (2006) "A novel estrogen sensor based on recombinant *Arxula adeninivorans* cells", **Biosensors & Bioelectronics**, 21(11), 2078-2085

K. Tag, T. Hahn, K. Riedel and G. Kunze, (2006) Biosensors and Bioassays based on microorganisms, **Research Signpost**, Kerala (India) (book chapter)

T. Hahn, C. K. O`Sullivan and K. S. Drese, (2009) "Microsystem for field-amplified electrokinetic trapping preconcentration of DNA at poly(ethylene terephtalate)-membranes", **Analytical Chemistry**, 81(8), 2904-2911

T. Hahn, C. K. O`Sullivan and K. S. Drese, (2009) "Microsystem for isolation of fetal DNA by size separation", **Clinical Chemistry**, 55(12), 2144-2152

T. Hahn, A. Kurz and S. Hardt, (2009) „Size separation of nucleic acids by electrophoretic transport across fluid boundaries", **Proceedings of MicroTAS**, Jeju (South Korea), 13, 809-811

R. Ganguly, T. Hahn and S. Hardt, (2010) "Characterization of magnetic bead-based microfluidic mixing for BioMEMS applications", **ISHMT-ASME** Heat and Mass Transfer Conference, Mumbai (India), 20, 619-626

R. Ganguly, T. Hahn and S. Hardt, (2010) "Magnetophoretic mixing for in-situ immunochemical binding on magnetic beads in a microfluidic channel", **Microfluidics and Nanofluidics**, 8(6), 739-753

T. Hahn, G. Münchow and S. Hardt, (2011) "Electrophoretic transport of biomolecules across liquid-liquid interfaces", **Journal of Physics: Condensed Matter**, accepted for publication

## Patents

O`Sullivan, T. Hahn and K. S. Drese, (2010) “Device and process for rapid isolation of a compound in a sample”, WO2010026222 (A1)

## Prices & Awards

Best student presentation at the General Assembly of the SAFE-network o. E. in Bristol (UK), FP6, E.U., Jan 2007

R. Ganguly, T. Hahn and S. Hardt, ISHMT-ASME Heat and Mass Transfer Conference, 2010, Mumbai (India), 20, 619-626, awarded for best conference paper

# Appendix

## List of figures

# List of tables